

# The Origin of Magnetic Noise in Nanoscale Square Dots

A DISSERTATION  
SUBMITTED TO THE FACULTY OF THE GRADUATE SCHOOL  
OF THE UNIVERSITY OF MINNESOTA  
BY

Daniel E. Endean

IN PARTIAL FULFILLMENT OF THE REQUIREMENTS  
FOR THE DEGREE OF  
Doctor of Philosophy

E. Dan Dahlberg

May, 2014

© Daniel E. Endean, 2014  
ALL RIGHTS RESERVED

# Acknowledgements

First and foremost, I would like to acknowledge the help and support of my adviser, Professor Dan Dahlberg. During my entire graduate career, Dan pushed me to be the best scientist I could be. He repeatedly challenged me to take my results one step further, all the while giving me the freedom to learn about and explore the physical world. My experimental technique will forever be improved by Dan's insistence that I follow Herb Broida's mantra: "make mistakes and *learn from them* as quickly as possible!"

I am thankful to have had the opportunity to work with all of my academic 'siblings.' Greg McKusky, Tanner Schulz, and Feng Guo gave me a great start as a fresh graduate student and taught me how to maintain the lab's equipment while progressing in research. Barry Costanzi and Bern Youngblood became great colleagues while talking through problems at the board, proofing my various papers including this thesis, commiserating over broken equipment, and reveling at those rare successful days in the cleanroom.

Many others beyond the Dahlberg lab also contributed to my success. Prof. Randall Victora was extremely helpful in discussing my results and confirming my observations through simulations. Chad Weigelt deserves acknowledgment not only for producing those simulations, but for catching all the details I missed in our papers. Discussions with Profs. Paul Crowell and Jim Kakalios about the physics of magnetism and noise were very useful. The physics department staff made my life much easier; Annie Bartels, Shelly Frankel, Julie Murphy, and MetteMarie Stewart in particular went above and beyond in helping me navigate the paperwork of graduate school. Jon Kilgore and the entire Machine Shop team were always willing to teach me a new machining technique. Likewise, the staff in the MNC and the CharFac were excellent sources of expertise and support. Bryan Cord, Kevin Roberts, Lage von Dissen, and Mark Fisher were particularly diligent in ensuring their equipment met my needs. I would also like to thank James Heyman at Macalaster College for helping me with the infrared measurements of my GMR films.

No set of acknowledgements would be complete without thanking those teachers who inspired my interest in physics. Gus Lukow first introduced me to physics in 2002; building Rube Goldberg machines with him was a true joy. Amy Kolan's introductory physics course at St. Olaf College showed me the beauty of how so few equations could explain so many physical phenomena. And, Jason Engbrecht was my first true experimentalist mentor; I am glad I had the opportunity to study positrons with him.

To my family and friends, thank you for supporting me. My grandmother, Ruth Endean, patiently listened to me and nurtured my love for science. My brother, Thomas, the chemist, challenged me with his conversations about all things scientific. My mother, Cheri, taught me to write well, encouraged me when times got tough, challenged me when I could take it, and was always there for me. My father, Tim, inspired me to enjoy science, taught me calculus on a napkin at the dinner table, and has always been interested in my work.

And finally, I must thank my wife, Aimée. She is my rock. Despite the ups and downs, despite late nights and early mornings, despite frustrating weeks that passed without progress, her support never wavers. She dares me to see the world from new perspectives. I am so glad she has been by my side through this process.

---

This work was supported primarily by ONR Grant N00014-11-1-0850 and the MRSEC Program of the NSF under Grant No. DMR-0819885. Part of this work was carried out in the University of Minnesota MNC, which receives partial support from the NSF through the NNIN program, and the Characterization Facility, a member of the NSF-funded Materials Research Facilities Network via the MRSEC program. I was personally supported by a three-year Graduate School Fellowship and the Doctoral Dissertation Fellowship, both funded by the University of Minnesota.

## Abstract

Magnetic fluctuations, also referred to as magnetic noise, in very small (sub-micron) magnetic systems are important both in studying the fundamental physics of statistical mechanics and in technology. Thermal fluctuations of the magnetization define the ultimate limit of magnetic storage densities and sensing technologies but may be useful in some biomedical applications. At high frequencies ( $>100$  kHz), fluctuations of the magnetization about the internal field are the dominant form of magnetic noise. At lower frequencies,  $1/f$  and random telegraph noise have been observed in many magnetic systems. Yet these noise sources are challenging to reproduce due to their origin in defects and, thus, identification of the physical mechanism which produces them is difficult. Further progress in studying magnetic noise requires a model system where the fluctuations are reproducible and the physical origin is known.

In this thesis, random telegraph noise is identified in square magnetic dots and shown to originate from a configurational anisotropy associated with the square dot geometry. The square dots were fabricated from thin ( $\sim 10$  nm) Permalloy films with side lengths ranging from 200 nm to 1  $\mu\text{m}$ , and the magnetization was measured via the anisotropic magnetoresistance. It is first shown, through measurements unaffected by the noise in these samples, that the square dot geometry exhibits a preference for the magnetization to align parallel to an edge of the square. A model of this four-fold configurational anisotropy explains the behavior of the magnetization and provides two methods to characterize the strength of the anisotropy.

It is then shown that when a field is applied along the dot diagonal, the configurational anisotropy barrier in this direction is lowered, which allows thermal switching of the magnetization between low-energy magnetic states. The telegraph state lifetimes are quantified and shown to vary with applied field magnitude, field direction, and temperature as expected. The switching rate obeys an Arrhenius law and the energy barriers measured in the noise data agree well with those measurements independent from the noise. In addition, micromagnetic simulations of the Landau-Lifshitz-Gilbert equation reproduce the observed behavior and confirm the explanation of the magnetic noise in these samples.

# Table of Contents

<b>Acknowledgements</b>	<b>i</b>
<b>Abstract</b>	<b>iii</b>
<b>List of Tables</b>	<b>ix</b>
<b>List of Figures</b>	<b>x</b>
<b>1 Introduction</b>	<b>1</b>
1.1 Motivation . . . . .	1
1.1.1 Fundamental Physics . . . . .	1
1.1.2 Applications Where Magnetic Noise Is Undesirable . . . . .	2
1.1.3 Applications Where Magnetic Noise Could Be Useful . . . . .	3
1.2 Noise Measurements . . . . .	3
1.2.1 Fourier Transform and Power Spectral Density . . . . .	4
1.2.2 White Noise . . . . .	5
1.2.3 Random Telegraph Noise . . . . .	5
1.2.4 $1/f$ Noise . . . . .	6
1.3 Magnetic Noise . . . . .	6
1.3.1 Magnetic White Noise . . . . .	6
1.3.2 Observations of Two-State Magnetic Switching . . . . .	7
1.3.3 Observations of Magnetic $1/f$ Noise . . . . .	8
1.4 Energetics of Ferromagnetism . . . . .	8
1.4.1 Exchange Energy . . . . .	9
1.4.2 Magnetostatic Energy . . . . .	9
1.4.3 Zeeman Energy . . . . .	10

1.4.4	Crystalline Anisotropy Energy . . . . .	10
1.4.5	Shape Anisotropy . . . . .	11
1.4.6	Configurational Anisotropy . . . . .	12
1.4.7	Thermal Energies . . . . .	13
1.5	Research Questions . . . . .	13
1.5.1	Conditions Necessary to Observe Magnetic Noise . . . . .	14
1.5.2	Quantitative Explanation of the Origins of Magnetic Noise . . . . .	14
<b>2</b>	<b>Experiment Design and Methodology</b>	<b>15</b>
2.1	Sample Design . . . . .	15
2.1.1	Size and Shape Considerations . . . . .	15
2.1.2	Measuring the Magnetization . . . . .	16
2.1.3	Material Considerations . . . . .	18
2.2	Sample Fabrication . . . . .	19
2.2.1	Substrate Preparation, Optical Lithography . . . . .	20
2.2.2	Electron Beam Lithography . . . . .	21
2.2.3	Deposition . . . . .	23
2.3	Measurement Techniques . . . . .	24
2.3.1	Current Source . . . . .	24
2.3.2	Pre-amplifier . . . . .	25
2.3.3	Resistance Measurements . . . . .	25
2.3.4	Spectrum Analyzer and Noise Measurements . . . . .	26
2.3.5	Magnetic Field . . . . .	27
2.3.6	Temperature Control . . . . .	28
2.3.7	Background Noise and Electrostatic Discharge Considerations . . . . .	28
2.4	Micromagnetic Simulations . . . . .	28
2.4.1	Landau-Lifshitz-Gilbert Equation . . . . .	29
2.4.2	LLG Micromagnetics Simulator . . . . .	29
2.4.3	Finite Temperature Simulations . . . . .	29
<b>3</b>	<b>Quantifying the Energy Landscape</b>	<b>30</b>
3.1	Identifying the Magnetization State through AMR . . . . .	30
3.1.1	Definition of Angle . . . . .	30
3.1.2	Large Field AMR Rotational Hysteresis Loops . . . . .	31

3.2	Rotational Hysteresis Data . . . . .	32
3.2.1	Rotational Hysteresis . . . . .	32
3.2.2	Differences in Rotational Hysteresis at Adjacent Corners . . . . .	34
3.3	Easy-Axis Linear Hysteresis Data . . . . .	35
3.3.1	Interpretation of the AMR Data . . . . .	35
3.3.2	Observation of Well-Defined Coercivities . . . . .	36
3.3.3	Effects Due to the Demagnetization Energy . . . . .	38
3.3.4	Observation of 4 Distinct Magnetic States . . . . .	38
3.3.5	Observation of Vortex Magnetic States . . . . .	39
3.4	Non-Easy-Axis Hysteresis Loops . . . . .	40
3.4.1	Near Easy-Axis Hysteresis Loops: Reduced Coercivity . . . . .	40
3.4.2	Near Diagonal Hysteresis Loops: Evidence of Rotation . . . . .	40
3.4.3	Diagonal Hysteresis Loops: Evidence of Magnetic Noise . . . . .	41
3.5	Stoner-Wohlfarth Model . . . . .	42
3.5.1	Model Description . . . . .	43
3.5.2	Modelling the Rotational Hysteresis Data . . . . .	44
3.5.3	Modelling the Easy-Axis Hysteresis Data . . . . .	46
3.5.4	Modelling Non-Easy-Axis Hysteresis Loops . . . . .	47
3.6	Size Dependent Configurational Anisotropy . . . . .	49
3.7	Limits of the Configurational Anisotropy Measurements . . . . .	51
3.7.1	Bending of the Magnetization . . . . .	51
3.7.2	Temperature Effects . . . . .	52
3.7.3	Sinusoidal Anisotropy . . . . .	53
3.7.4	Fabrication Imperfections . . . . .	53
3.8	Comparison to Micromagnetic Simulations . . . . .	54
3.8.1	Easy-Axis Hysteresis . . . . .	54
3.8.2	Rotational Hysteresis . . . . .	56
<b>4</b>	<b>Observation and Explanation of Telegraph Noise</b>	<b>57</b>
4.1	Signatures of the Telegraph Noise . . . . .	57
4.1.1	Noise in Hysteresis Loops at the Dot Diagonal . . . . .	57
4.1.2	Observed Noise PSDs: Lorentzian Spectra . . . . .	58
4.1.3	Time Dependence of the Resistance at a Fixed Field . . . . .	60
4.1.4	Telegraph Frequency and Fitting the Lorentzian . . . . .	61



4.2	Tuning and Quantifying the Magnetic Noise . . . . .	61
4.2.1	Field Dependence of the Telegraph Frequency . . . . .	62
4.2.2	Temperature Dependence of the Telegraph Frequency . . . . .	63
4.2.3	Arrhenius Law and the Attempt Frequency . . . . .	63
4.2.4	Ferromagnetic Resonance Approximation . . . . .	65
4.2.5	Field Dependence of the Energy Barrier . . . . .	65
4.2.6	Comparison to the Stoner-Wohlfarth Model . . . . .	66
4.2.7	Angular Dependence of the Telegraph Noise . . . . .	67
4.3	Micromagnetic Simulations of Noise . . . . .	68
4.3.1	Simulations of Hysteresis Loops Along the Dot Diagonal . . . . .	68
4.3.2	Simulations of Thermally Driven Telegraph Noise . . . . .	70
4.3.3	Magnetization Configuration of Telegraph States . . . . .	71
<b>5</b>	<b>Conclusions and Future Directions</b>	<b>72</b>
5.1	Conclusions . . . . .	72
5.1.1	Quantifying the Magnetic Energy Landscape in Square Dots . . . . .	72
5.1.2	Discovering and Explaining Magnetic Noise in Square Dots . . . . .	73
5.2	Future Experimental Directions and Open Questions . . . . .	74
5.2.1	Configurational Anisotropy Phase Change . . . . .	74
5.2.2	Configurational Anisotropy Angular Dependence . . . . .	75
5.2.3	Observations of $1/f$ noise . . . . .	78
5.2.4	Chained Square Dots . . . . .	79
5.2.5	Attempt Frequency and High Frequency Effects . . . . .	80
5.2.6	Domain Wall Measurements . . . . .	80
5.2.7	Stochastic Resonance . . . . .	81
	<b>References</b>	<b>83</b>
	<b>Appendix A. Microwave Measurements of Giant Magnetoresistance</b>	<b>91</b>
A.1	Experimental Motivation and Goals . . . . .	91
A.1.1	GMR Dependence on Current Direction . . . . .	91
A.1.2	Quantifying GMR at Microwave Frequencies . . . . .	92
A.2	Sample Fabrication . . . . .	93
A.3	Attempts to Measure CPP-GMR . . . . .	93

A.3.1	Experimental Design and CPP-GMR Measurements . . . . .	93
A.3.2	Theoretical Justifications for Infeasibility . . . . .	95
A.4	Quantifying Microwave CIP-GMR . . . . .	96
A.4.1	Experimental Design . . . . .	97
A.4.2	Theoretical Predictions . . . . .	98
A.4.3	Experimental Observations . . . . .	100
A.5	Discussion . . . . .	102
A.6	Conclusions and Future Directions . . . . .	104
<b>Appendix B. Details of the Fabrication Process</b>		<b>105</b>
B.1	Fabrication Procedure . . . . .	105
B.2	Bilayer Photolithography Recipe . . . . .	107
B.3	Bilayer Electron Beam Lithography Recipe . . . . .	108
<b>Appendix C. Experimental Techniques</b>		<b>111</b>
C.1	Low Noise Considerations . . . . .	111
C.1.1	Grounding . . . . .	111
C.1.2	Faraday Shielding . . . . .	112
C.1.3	Cable Shielding . . . . .	112
C.1.4	Magnetic Field Noise . . . . .	112
C.1.5	Spectrum Analyzer Setup . . . . .	112
C.1.6	Pre-Amplifier Setup . . . . .	113
C.1.7	Computer and GPIB . . . . .	114
C.1.8	Low-Temperature Setup . . . . .	114
C.2	Electrostatic Protections . . . . .	115
C.2.1	Grounding . . . . .	115
C.2.2	Foil Coverings and Experimentalist Wristbands . . . . .	115
C.2.3	Experimental Design and Start-up . . . . .	116
C.2.4	Wirebonding . . . . .	116
C.2.5	SEM Work . . . . .	116
<b>Appendix D. Derivation of the FMR Frequency in Square Dots</b>		<b>118</b>
<b>Appendix E. Abbreviations and Symbols</b>		<b>120</b>

# List of Tables

C.1	Instrumentation settings for low noise measurements. . . . .	113
E.1	List of Abbreviations . . . . .	120
E.2	List of Symbols . . . . .	121

# List of Figures

1.1	Examples of noise: time spectra and PSDs . . . . .	4
1.2	Observations of RTN in spin-polarized STM . . . . .	7
1.3	Cartoon demonstration of shape anisotropy . . . . .	11
1.4	Phase diagram for square magnetic dots . . . . .	12
1.5	Spin configurations for square magnetic dot phases . . . . .	13
2.1	SEM micrograph of a finished sample . . . . .	16
2.2	AMR dependence on Ni concentration in Fe . . . . .	17
2.3	Variation in crystalline anisotropy for NiFe alloys . . . . .	18
2.4	Schematic of the lift-off fabrication process . . . . .	19
2.5	Sample contact geometry on a 1 cm chip . . . . .	21
2.6	Problems encountered in monolayer resist lift-off . . . . .	22
2.7	Noise floor of the SRS 560 pre-amplifier . . . . .	26
3.1	AMR effect in a 350 nm dot for large applied fields . . . . .	31
3.2	Rotational hysteresis at small applied fields . . . . .	32
3.3	Rotational hysteresis in a dot with dissimilar corners . . . . .	33
3.4	Dot-to-dot variations due to fabrication imperfections . . . . .	34
3.5	Hysteresis loop along the dot easy axis . . . . .	35
3.6	Simulation of an easy-axis hysteresis loop . . . . .	36
3.7	Easy-axes hysteresis loops for 400 nm and 200 nm dots . . . . .	37
3.8	Evidence of vortices in circular and large square dots . . . . .	39
3.9	Hysteresis loops away from the easy axes . . . . .	41
3.10	Hysteresis loops at the dot diagonal . . . . .	42
3.11	Diagram of the magnetic energy for a square dot . . . . .	44
3.12	Simulated rotational hysteresis using the Stoner-Wohlfarth model . . . . .	45
3.13	Simulated hysteresis loops using the Stoner-Wohlfarth model . . . . .	48

3.14	Easy-axis coercivity and minimum rotational hysteresis fields . . . . .	49
3.15	Configurational anisotropy dependence on dot size . . . . .	50
3.16	Temperature dependence of linear hysteresis loops . . . . .	52
3.17	Micromagnetic simulations of easy-axis hysteresis loops . . . . .	54
3.18	Micromagnetic simulations of rotational hysteresis . . . . .	55
3.19	Vector fields of the magnetic configurations during rotational hysteresis simulations . . . . .	56
4.1	Magnetic energy surface which produces telegraph noise in square dots . . .	58
4.2	PSDs of magnetic noise in square dots at various applied fields . . . . .	59
4.3	Real-time data of RTN for various applied fields . . . . .	60
4.4	Dependence of switching frequency on applied field . . . . .	62
4.5	Switching frequency dependence on sample temperature . . . . .	63
4.6	Arrhenius plot of switching frequency vs. temperature . . . . .	64
4.7	Energy barrier heights extracted as a function of applied field . . . . .	66
4.8	RTN plotted as a function of applied field direction . . . . .	68
4.9	Micromagnetic simulations of hysteresis loops for applied fields along the dot diagonal . . . . .	69
4.10	RTN observed in micromagnetic simulations . . . . .	70
4.11	Vector fields for the two telegraph states obtained from simulations . . . . .	71
5.1	Rotational hysteresis exhibiting additional magnetic transitions . . . . .	75
5.2	An 8 contact dot to differentiate ‘C’ and ‘S’ shaped magnetizations . . . . .	76
5.3	Hysteresis and PSD data for a rectangular dot . . . . .	77
5.4	Observations of $1/f$ noise in square dots . . . . .	78
5.5	Diagram illustrating a chained set of square dots . . . . .	79
5.6	Proposed experiment to measure domain wall noise . . . . .	81
A.1	Setup for the CPP/CIP comparison experiment . . . . .	94
A.2	Microwave response vs. film angle in the CPP-GMR experiment . . . . .	95
A.3	Comparison of a resistor and capacitor . . . . .	96
A.4	Microwave setup for the CIP-GMR experiment . . . . .	97
A.5	Absolute reflection and transmission coefficients of GMR films . . . . .	100
A.6	Field dependence of $\mu$ GMR and transport GMR effects . . . . .	101
A.7	$\mu$ GMR effect in the transmission and reflection coefficients . . . . .	102
A.8	Reflection coefficient change at infrared frequencies due to GMR . . . . .	103

# Chapter 1

## Introduction

Our everyday encounters with magnets suggest that a magnet has two distinct magnetic poles termed north and south. More technically speaking, alignment of the magnetic moments of the individual electrons in a magnet gives the bulk magnet its poles. The magnetization of this system is the vector field which describes the orientation of the electron spins. Without further information about the nature of the magnet, however, there is no reason to expect the magnetization of the system to remain fixed with time. In fact, the only reason that commonly encountered magnets exhibit a stable magnetization is that it costs too much energy for the magnetization to change direction. Yet, as will be discussed in this thesis, if a magnet becomes sufficiently small, the energy barriers which prevent the magnetization from switching direction can shrink to the point where the orientation of the magnetization no longer remains stable but fluctuates. The primary goal of this work is to determine the conditions under which magnetic fluctuations, also termed magnetic noise, can be experimentally observed and to explain their origin.

### 1.1 Motivation

#### 1.1.1 Fundamental Physics

At small enough length scales our traditional conception of permanent magnets break down. The magnetization in a material is determined by minimization of the total magnetic energy in the system. For a simple system, the magnetization can be represented as a ball rolling on a hilly surface. The location of the ball corresponds to the magnetization direction while the height of the hills represents the magnetic energy of the system. The

magnetization seeks low spots in the hilly landscape to minimize its energy. However, at any finite temperature, thermal energies also exist and increase the entropy of a system by enabling the magnetization to sample other energy states. In general, the sizes of the energy barriers depend directly on the volume of the magnetic sample under study. Thus, as the sample size shrinks, thermal energies will begin to play a larger and larger role in determining the magnetization dynamics.

From a theoretical perspective, the conditions necessary to observe the magnetic fluctuations are still not well understood. If the energy barriers in the system are small in comparison to thermal energies, the magnetization will become entirely unpinned and rotate randomly in any direction, an effect known as superparamagnetism [1, 2]. But above this limit, the energy barriers can be influenced by the sample properties (size, material and shape) and the appearance of the noise may be affected by experimental conditions such as magnetic field, temperature, and interactions with nearby magnetic structures. Furthermore, many other magnetic effects become significant at the nanoscale including those due to the surface roughness of a particle, interactions between the grains within a sample, and domain structures [3, 4]. While several reports discussed below indicate the existence of magnetic noise, the parameters which are most relevant in determining whether the magnetization fluctuates are still poorly understood.

### 1.1.2 Applications Where Magnetic Noise Is Undesirable

Many applications that use magnetic materials, especially the magnetic storage industry, are interested in ways to reduce magnetic noise. As the areal density of information in a hard drive increases, the individual magnetic bits shrink and become increasingly susceptible to thermal fluctuations [5, 6]. Unfortunately, this problem cannot be alleviated simply by increasing the size of the magnetic energy barriers since they are limited by the maximum magnetic field available to write information to the disk (which is currently limited to a maximum value of 24 kOe in known magnetic materials) [7]. Thus, a better understanding the physics of superparamagnetism and the conditions necessary to observe magnetic noise may lead to insight into ways to suppress these fluctuations and allow further improvements in hard drive technology.

In addition to the ability to store information in magnetic particles, the ability to sense magnetic fields is also affected by magnetic noise. The sensor used in a hard drive to read back the magnetic information currently is a magnetic tunnel junction (MTJ) which

contains multiple magnetic layers. Magnetic noise observed in MTJs has been shown to limit the signal-to-noise ratio of these sensors, as discussed later in this chapter. In addition to the hard drive industry, MTJs and other magnetic sensors are being developed as alternatives to superconducting quantum interference devices (SQUIDs) and hall-effect probes for measuring magnetic fields [8, 9]. Applications for these devices include precision measurements, biological tests to sense magnetic particles, or magnetic compassing in devices such as cell phones [10].

### 1.1.3 Applications Where Magnetic Noise Could Be Useful

Though noise is usually undesirable, there are several applications where magnetic noise may actually be useful. In a variety of biomedical and pharmaceutical applications, magnetic particles could be attached to drugs or biological markers [11, 12]. The magnetic particle could act as a carrier to bring the attached drug to a certain part of the body via an externally applied field. Or, the biological tag could direct the particle within the body, and the magnetic particle would then be used in treating disease by taking advantage of the fact that it can be heated with the application of an alternating magnetic field [13]. And, for imaging applications the magnetic particles could increase the contrast in magnetic resonance imaging (MRI) [14].

In these applications, superparamagnetism discourages the magnetic particles from clumping through magnetostatic attraction before they are delivered to the target location in the body [15, 16]. Superparamagnetic particles are ideal for these applications since their magnetic moments fluctuate too fast for magnetostatic attractions to cause the particles to clump (though interactions between particles may stabilize the magnetization). Thus, understanding ways to controllably increase magnetic fluctuations in magnetic nanoparticles is critical for these applications and offers motivation for controllably producing magnetic noise.

## 1.2 Noise Measurements

In most contexts, noise is the undesirable fluctuation of a measured quantity that obscures the desired signal. However, the magnitude and frequency of the deviations of a signal about its average value often reveal additional information about a physical system. Examples of common noise signatures are plotted in Fig. 1.1. To quantify the differences



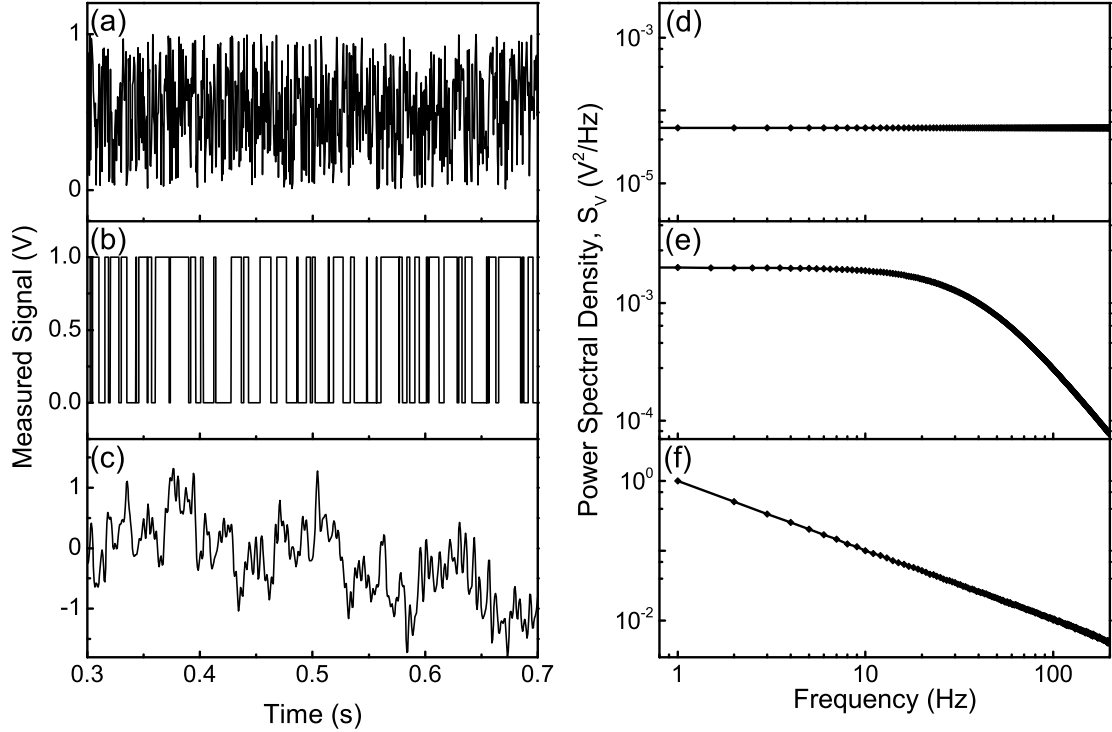


Figure 1.1: Simulated time spectra of (a) white, (b) random telegraph, and (c)  $1/f$  noise signals with (d-f) the corresponding PSDs plotted on a log-log plot as a function of frequency. The PSD amplitude for white noise is frequency independent while the PSD for  $1/f$  noise forms a straight line with slope equal to minus one. The PSD of RTN has a white noise spectrum at low frequencies which then falls off as  $1/f^2$  above a characteristic average switching frequency.

between these types of noise, a power spectral density (PSD) of the noise is computed which reveals size of the fluctuations of a physical quantity as a function of frequency. Examples of the PSD for the noise spectra plotted in Fig. 1.1(a-c) are shown in Fig. 1.1(d-f). We discuss the interpretation of the PSD and these types of noise below.

### 1.2.1 Fourier Transform and Power Spectral Density

The PSD can be interpreted either as the power dissipated by a system at different frequencies or the characteristic frequencies over which the state of the system is well correlated. In the first interpretation, the PSD is understood as the square of the Fourier transform of the signal itself. Large Fourier components correspond to large fluctuations at a particular

frequency; if the PSD is peaked at a certain frequency one would identify the system as dissipating energy at that frequency. Similarly, if the PSD is large at high or low frequencies, one would expect to see fluctuations over short or long time scales respectively. Similarly, using the second interpretation, if a signal is highly correlated with itself over long time periods, it will have a large PSD at low frequencies but a small PSD at high frequencies. The actual computation of the PSD can be done following both interpretations but yields the same result [17]. Experimental details are provided in Sec. 2.3.4.

### 1.2.2 White Noise

White noise is the simplest form of noise because its PSD has a constant value independent of frequency as shown in Fig. 1.1(d). White noise occurs in physical systems where the source of the noise is entirely uncorrelated. As an example, the voltage measured across an unbiased resistor fluctuates in time due to thermal agitation of the charge carriers in the resistor [18, 19]. These charge carriers are uncorrelated so that, up to a characteristic collision frequency, all frequencies are equally represented. This effect is known as Johnson-Nyquist noise, which has a PSD given by

$$S_V(f) = 4k_BTR\Delta f, \quad (1.1)$$

where  $R$  is the sample resistance,  $T$  is the temperature,  $k_B$  is the Boltzmann constant, and  $\Delta f$  is the measurement bandwidth [17].

Similarly, since the charge carriers such as electrons carry discrete packets of charge, the current exiting the system under study consists of a series of delta function pulses of charge [20]. Since the Fourier transform of a delta function is a constant, this second source of electronic noise, called shot noise, also causes frequency independent white noise [17]. The relative magnitudes of the Johnson-Nyquist and shot noises in a circuit depend on temperature, resistance, and current densities. For the work discussed here, Johnson-Nyquist noise will form the dominant non-magnetic background noise signal.

### 1.2.3 Random Telegraph Noise

Random telegraph noise (RTN), also known as popcorn or burst noise, is associated with a measured signal randomly switching between two or more distinct values. RTN exists in a physical system where the system can take on several different energetically favorable

metastable states. An example of a simulated RTN signal is shown in Fig. 1.1(b) with corresponding PSD in Fig. 1.1(e). Assuming the lifetimes of the telegraph states follow a Poisson distribution the PSD of a RTN signal takes the form of a Lorentzian,

$$S_V(f) = 4\Delta V^2 \frac{f_1 f_2}{(f_1 + f_2)} \frac{1}{(f_1 + f_2)^2 + (2\pi f)^2}, \quad (1.2)$$

where  $f_1$  and  $f_2$  are the reciprocals of the characteristic lifetimes for the two telegraph states with voltage difference  $\Delta V$  [17, 21]. At low frequencies, below  $(f_1 + f_2)$ , the PSD is frequency independent and appears as white noise since on long time scales the value of the signal is completely uncorrelated. However, at high frequencies, the PSD decays as  $1/f^2$  since on short time scales the signal becomes increasingly well correlated.

#### 1.2.4 $1/f$ Noise

A third type of noise that appears in many physical systems is termed  $1/f$  noise for its frequency dependence. When the PSD is plotted on a log-log plot, a  $1/f$  power spectrum appears as a line with a slope of minus one as shown in Fig. 1.1(f). This type of noise has been observed in a wide variety of signals including electronic circuits [22], nerve membranes [23], classical music [24] and the flood levels of the Nile river [25]. However, to date no useful universal explanation of  $1/f$  noise has emerged [26]. As the name implies,  $1/f$  noise indicates correlations over long times since the noise power is proportional to the inverse of the frequency. It should also be noted that Dutta *et al.* have developed a model whereby a particular distribution of RTN sources can added together to give rise to  $1/f$  noise [27].

## 1.3 Magnetic Noise

### 1.3.1 Magnetic White Noise

Frequency independent white noise in magnetism has been observed and is well understood. This magnetic noise signature is associated with thermal fluctuations of the magnetization about an internal field within the sample [28, 29]. This internal field results from a minimum in the magnetic energy and fluctuations of the magnetization about this field give rise to this noise signature. Since the fluctuations result in a very small change in the magnetization direction in the sample and are evenly distributed over a wide frequency

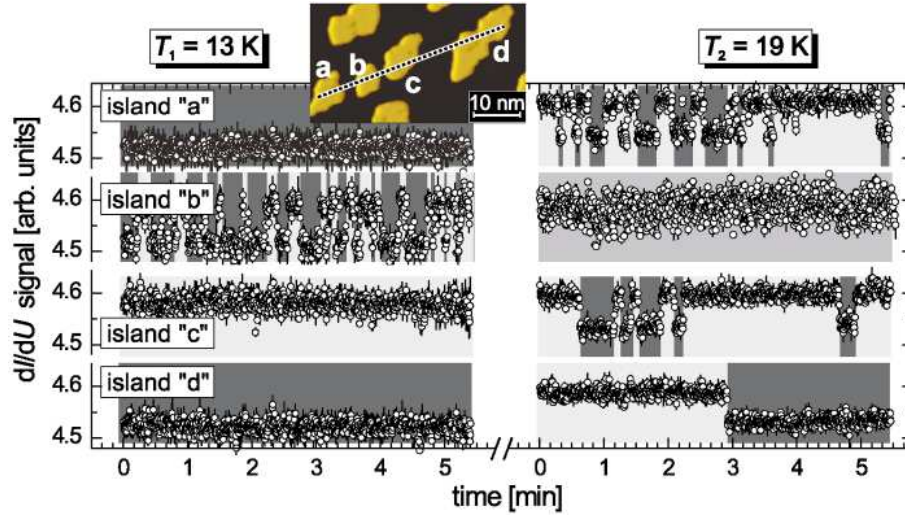


Figure 1.2: Spin-polarized STM measurements of Fe nanoislands with monolayer thickness (inset). The plot shows the measured differential conductance which is proportional to the out-of-plane component of the nanoisland magnetization as a function of time for two temperatures. Each particle shows thermally activated RTN associated with fluctuations of its magnetization. Reprinted, with permission, from Ref. [30]. Copyright 2004, APS.

range they are too small to be observed in most experiments.

### 1.3.2 Observations of Two-State Magnetic Switching

In magnetic systems where two low-energy magnetic states are separated by an energy barrier several times larger than thermal energies, the magnetization can exhibit two-state switching in the form of RTN. A convincing demonstration of this type of magnetic noise was provided by Bode *et al.* [30] in observing the magnetization reversal in atomically thin Fe nanoislands using spin-polarized scanning tunneling microscopy (STM) as shown in Fig. 1.2. In these experiments and several others [31, 32], the magnetization switches between low energy states via thermal energies with a switching rate that depends on temperature, the particle size, and its shape. Similarly, Burgess *et al.* found that the core of a magnetic vortex can exhibit random telegraph switching between neighboring pinning sites and that by applying a magnetic field, the time spent at each pinning site could be varied [33]. Thermally activated two-state switching behavior has also been observed in domain wall hopping between pinning sites in MTJs [34–37] and in the magnetization of magnetic ErAs nanoparticles [38].

In all of the systems studied to date, the experiments rely on defects, imperfections in the fabrication process, or self-ordering processes to produce sufficiently small magnetic volumes for magnetic noise to be observed. Thus, while the magnetization in these systems certainly exhibits measurable fluctuations, the experimental conditions do not allow the fluctuations to be controlled except by varying of temperature and in some cases the applied field. Furthermore, temperature and applied field cycling often destroy the existence of a given fluctuator limiting the reproducibility of the magnetic observations [35, 36, 38].

### 1.3.3 Observations of Magnetic $1/f$ Noise

Most reports of  $1/f$  magnetic noise come from measurements on MTJs. The resistance of an MTJ varies greatly (in some cases by more than 100%) with the relative orientation of its two magnetic layers [39]. Thus, measuring resistance noise in an MTJ, if properly characterized, provides indirect measurement of magnetic fluctuations. Several groups have claimed that the  $1/f$  noise in these systems increases when one of the magnetic layers is switching, sometimes by several orders of magnitude [34, 35, 37, 40, 41]. In addition, measurements on magnetic films with perpendicular anisotropy also appear to show an increase in  $1/f$  magnetic noise as the magnetization switches in a hall-effect measurement [42].

However, as with  $1/f$  noise in non-magnetic systems, the origins of magnetic  $1/f$  noise are still very poorly understood. The Fluctuation-Dissipation theorem [43] may explain the magnitude of the  $1/f$  noise observed if several conditions of the theorem are relaxed [34, 37, 42] though some reports dispute this explanation [35, 40, 41]. However, even if the Fluctuation-Dissipation accounts for  $1/f$  noise, it still fails to provide a satisfying explanation of the microscopic origin for the magnetic  $1/f$  noise.

It should also be noted that in some reports of  $1/f$  magnetic noise, RTN has also been observed in the same samples at very similar magnetic fields [34, 35, 37]. Thus, investigations of magnetic RTN appear necessary to fully explain magnetic  $1/f$  noise.

## 1.4 Energetics of Ferromagnetism

The explanation for the magnetic fluctuations discussed in this thesis relies on the underlying energetics associated with magnetic materials [44]. We briefly summarize the

four magnetic energies and discuss their relation to the energy landscape intrinsic to the samples studied in this thesis.

### 1.4.1 Exchange Energy

The ferromagnetic exchange energy quantifies the fundamental tendency of a material toward ferromagnetism. That is, it specifies the energy gain in the material if neighboring electron spins are aligned. It originates from the Pauli exclusion principle which requires that two electrons cannot occupy the same quantum mechanical state. In essence, if two electrons are in the same spin state then the Pauli exclusion principle forces them to occupy different orbital states which increases their spatial separation. Since increasing the distance between electrons lowers the electrostatic energy of the system, a parallel spin configuration may become energetically favorable state (a net energy gain is only possible in materials where a large number of orbital states near the Fermi energy have similar kinetic energy). The details of this mechanism can be found elsewhere, but in general the transition metals Ni, Fe, and Co and some rare-earth elements favor ferromagnetism [45].

The exchange interaction is considered a local magnetic energy since it acts over short range and only depends on the alignment of neighboring spins. For the purposes of calculating the energy of a bulk ferromagnetic system, a phenomenological parameter known as the exchange stiffness constant,  $A_{ex}$  describes the energy cost per unit length associated with a non-uniform magnetization. Permalloy ( $\text{Ni}_{80}\text{Fe}_{20}$ ), the primary material studied in this thesis, has an exchange stiffness constant of approximately  $1 \mu\text{erg}/\text{cm}$  [45, 46].

### 1.4.2 Magnetostatic Energy

Also known as the dipole-dipole energy, the magnetostatic energy arises from the interaction of the magnetic dipole fields of the electron spins. The lowest energy configuration of two neighboring dipoles is to be oppositely polarized since in this configuration the north (south) pole of each dipole will be closer to the south (north) pole of the other dipole. For a large collection of spins, the dipole-dipole interactions can be integrated to determine the total magnetostatic energy of the system. Since the magnetostatic energy depends on the strength of the field produced by the dipoles in the material, we can quantify the magnitude of the magnetostatic energy through the saturation magnetization,  $M_s$  of the material. For permalloy,  $M_s$  is  $800 \text{ emu}/\text{cm}^3$  [45].

Since the magnetostatic energy originates from the magnetic dipole interaction, it is a long-range interaction in contrast with the exchange energy which is a short range interaction between neighboring spins. Thus, in small magnetic particles, the exchange energy will dominate and uniform magnetization will be observed. On longer length scales, the magnetostatic energy dictates and encourages the formation of domains with opposite magnetization. Since the magnetostatic and exchange energies discourage and encourage uniform magnetization respectively, a characteristic length scale, called the exchange length [47], emerges:

$$R_0 = \sqrt{2\pi} \sqrt{\frac{A_{ex}}{2\pi M_s^2}}. \quad (1.3)$$

In general the exchange length depends on the crystalline anisotropy discussed below, but in the limit of zero crystalline anisotropy it reduces to Eq. 1.3. Magnetic domains tend to form on length scales larger than the exchange length while uniform magnetization single-domain particles should be observed on length scales comparable to or shorter than this length scale [48]. For permalloy, the exchange length is roughly 6 nm [47].

### 1.4.3 Zeeman Energy

The Zeeman energy of a ferromagnet is simply the interaction of the individual dipoles in the system with an externally applied field,  $\mathbf{H}$ . This energy favors alignment of the magnetization to the applied field and is computed as,

$$E = -\mathbf{m} \cdot \mathbf{H}, \quad (1.4)$$

where  $\mathbf{H}$  is the applied field vector, and  $\mathbf{m}$  is the magnetic moment of the sample. In general the Zeeman energy provides the only externally tunable magnetic energy in the system.

### 1.4.4 Crystalline Anisotropy Energy

The fourth main energy in a ferromagnet will not be central to this thesis but is mentioned here for completeness. The crystalline anisotropy energy arises from the spin-orbit energy in a material, which preferentially favors a magnetization which aligns with certain crystalline axes in a material [44]. The magnitude of the crystalline anisotropy is

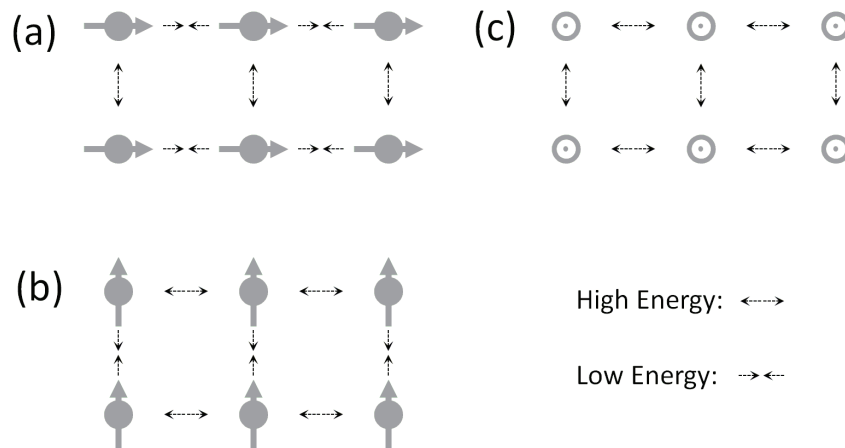


Figure 1.3: A schematic comparison of three magnetization states for a 3x2x1 arrangement of 6 spins. When the magnetization is (a) parallel to the long axis there are 3 high energy and 4 low energy interactions. Higher energy states are seen for the cases when the spins are (b) aligned with the short axis and (c) point out of the plane. This analysis accounts only for nearest neighbor interactions.

highly dependent on material composition, crystalline structure, and growth conditions. Additional material dependent energies also arise from the spin-orbit interaction, such as magnetostriction which couples the stress applied to a film to its magnetization. Permalloy has near zero crystalline anisotropy energy and magnetostriction constants that are orders of magnitude smaller than the magnetostatic and exchange energies [49, 50].

#### 1.4.5 Shape Anisotropy

The magnetic energies relevant in this thesis depend entirely on the geometrical shape of the samples. Shape anisotropy is a direct consequence of the magnetostatic energy of a system. As an example, consider the six magnetic dipoles arranged in a rectangle shown in Fig. 1.3. The lowest energy configuration occurs when the magnetization is parallel to the long axis; in this state there are three high energy parallel interactions and four low energy tip-to-tail interactions. When the magnetization is parallel to the short axis there are four high and three low energy interactions. And, for a magnetization out-of-the-plane there are six high energy interactions. Thus, a shape anisotropy energy exists favoring magnetization in-plane along the long axis. For larger samples this same rule holds true; the longest axes of the sample tend to have the lowest shape anisotropy energy.



### 1.4.6 Configurational Anisotropy

A unique situation arises when the symmetry of the system increases, as in the case of a square sample. If the example above is repeated with four spins in a square, the in-plane magnetization is still favored. However, for uniform magnetization, the magnetostatic energy is equal for all directions in-the-plane [51]. Thus squares—as well as triangles, pentagons, and any regular polygon—have no in-plane shape anisotropy.

In these regular shapes, a configurational anisotropy [53] results from non-uniformities in the magnetization. Consider a thin square magnetic particle. If the magnetization is allowed to bend slightly, and adopt a C shaped magnetic state, it may lower the magnetostatic energy more than it increases the exchange energy, reducing the total energy of the system. As a result, certain magnetization directions of the particle will be of lower energy. In previous measurements performed by Cowburn *et al.*, a net magnetization along the dot diagonal resulted in a lower total energy than magnetization parallel to an edge of the square [54]. Simulations by the same researchers produced the phase diagram shown in Fig. 1.4 which indicates the lowest energy magnetic configuration, diagrammed in

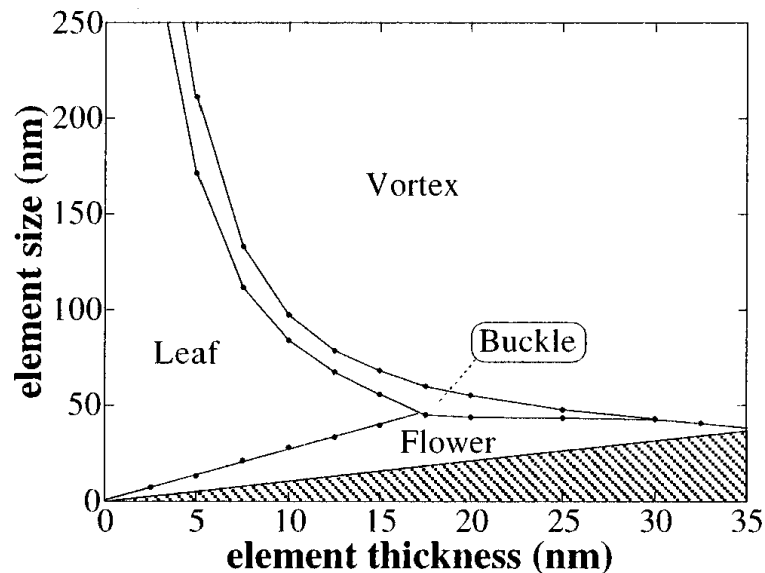


Figure 1.4: A magnetic phase diagram of the lowest energy magnetic configuration for thin square permalloy particles at a given thickness and side length (element size). The lowest energy state has the minimum combined exchange and magnetostatic energy among the four states listed in the diagram and displayed in Fig. 1.5. Reprinted, with permission, from Ref. [52]. Copyright 1998, AIP.

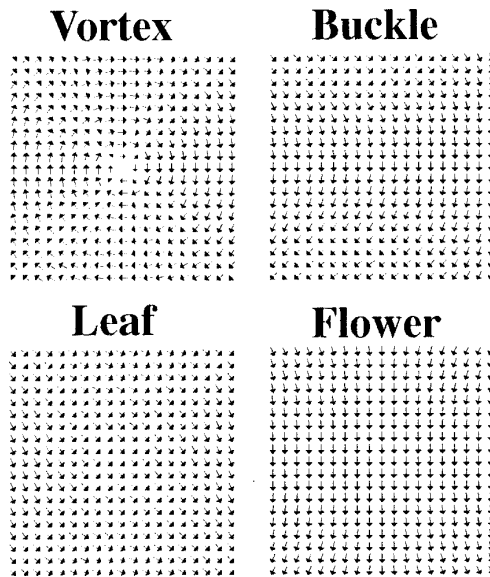


Figure 1.5: Examples of the magnetization configurations for a planar square magnetic dot calculated for a  $95 \times 95 \times 5$  nm nanostructure by Cowburn *et al.* The arrows denote the in-plane component of the magnetization vector for each simulation cell. These states correspond to those presented in Fig. 1.4; for this size element the leaf state has the lowest energy. Reprinted, with permission, from Ref. [52]. Copyright 1998, AIP.

Fig. 1.5, for permalloy squares of various sizes [52, 55]. Thus, the square particle, as well as other geometrical shapes [56], still exhibits a geometrical anisotropy which depends on the configuration of the magnetization.

#### 1.4.7 Thermal Energies

In addition to the magnetic energies discussed here, a complete description of a magnetic system requires incorporation of thermal energies. At zero temperature, the magnetization will occupy the lowest energy state. At finite temperatures, however, the system has a finite probability to transition over an energy barrier to another lower energy state [57, 58]. The details of these transitions are discussed in Chapter 4.

## 1.5 Research Questions

To investigate magnetic noise, we utilize the configurational anisotropy of square permalloy dots to control the magnetic energy landscape of the dots and study the resulting magnetic

noise. In this investigation of noise we have resolved two long standing questions regarding noise in magnetic systems.

### 1.5.1 Conditions Necessary to Observe Magnetic Noise

The first step was to determine the conditions necessary to observe magnetic noise. According to thermodynamics, magnetic noise must exist. Several experiments, discussed above, have demonstrated its existence. However, these systems lack control of the magnetic energy barriers that give rise to the noise, making it difficult to reproduce. When the magnetic noise is indirectly measured, for example through the sample resistance, other non-magnetic sources of noise may obscure the noise signals of interest. This is especially of concern in MTJs where properties of the barrier, sample preparation conditions, and interactions between the magnetic layers complicate the analysis [36, 59, 60].

Thus, we have developed a magnetic system to unambiguously observe reproducible magnetic noise. The details of this simplified system and our measurement techniques are discussed in Chapter 2. Square magnetic dots were chosen for their configurational anisotropy which gives rise to relatively small energy barriers. Measurements of these energy barriers [61] are discussed in Chapter 3. The magnetic noise originating from thermal activation of the magnetization over these energy barriers is presented in Chapter 4.

### 1.5.2 Quantitative Explanation of the Origins of Magnetic Noise

In addition to observing magnetic noise, we determined and quantified the fundamental physical origin of the magnetic noise in our system. Theoretically magnetic noise should be governed by the underlying magnetic energy landscape. The properties of the magnetic energy landscape in our samples are measured in Chapter 3 to confirm that the energy barriers which we extract from analysis of the noise correspond to the properties of the samples under study. We show that the noise observed in our samples is explained by these energy barriers in Chapter 4 through quantitative temperature and field dependent measurements and through micromagnetic simulations. In Chapter 5 we place these results in the context of other measurements and offer future applications for this model system to study more complex sources of magnetic noise.

## Chapter 2

# Experiment Design and Methodology

In this chapter we discuss the methods used in preparing our samples and the techniques used to measure the magnetization. The experimental design focused on two key requirements: producing samples with large magnetic fluctuations and accurately measuring the sample magnetization. The final appearance of the samples studied can be seen in the scanning electron microscopy (SEM) micrograph shown in Fig. 2.1.

### 2.1 Sample Design

#### 2.1.1 Size and Shape Considerations

To observe magnetic RTN, the magnetic energy of a system must possess two low-energy magnetic states with significantly different magnetization configurations. As discussed in Sec. 1.4.6, the magnetostatic energy of a ferromagnet creates a geometry-dependent anisotropy energy known as the configurational anisotropy for highly symmetric shapes. Since a square possesses four-fold symmetry, it will have four equally low-energy magnetic states with the magnetization rotated by  $90^\circ$  between neighboring states. As will be demonstrated in Chapter 3, square dots exhibit barriers associated with magnetization along the square diagonal. By applying an appropriate magnetic field these energy barriers can be tuned to produce magnetic fluctuations.

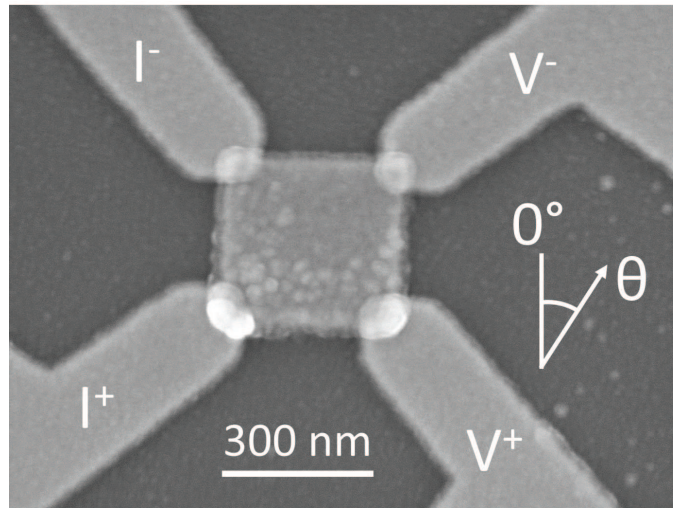


Figure 2.1: An SEM micrograph of a completed 250 nm square Permalloy dot (center) with four non-magnetic Ti-Au electrodes. The current and voltage leads are labelled as they are connected in the experiment; directions of the magnetization and applied field are defined relative to the primary current direction as indicated. The image was taken using 3 keV electrons at a working distance of 3.0 mm in the JEOL 6700 SEM located in the University of Minnesota Characterization Facility. The sample was coated with 5 nm of C prior to imaging to reduce charging artifacts.

### 2.1.2 Measuring the Magnetization

While small sample sizes are desirable from the perspective of producing small energy barriers to encourage magnetic fluctuations, measurement considerations generally favor larger samples. Direct measurements of the magnetization using vibrating sample magnetometry, magneto-optical Kerr effect (MOKE) [62], AC susceptibility [63] or other field sensitive techniques generally rely on large arrays of magnetic particles to obtain sufficient signal [4]. Since we seek unambiguous observation of magnetic noise, the averaging effect in these measurements would obscure the signal of interest. Thus, we utilize a magnetoresistance effect that allows us to infer the behavior of the magnetization of a single particle by correlating changes in the sample resistance to a change in the magnetization. Previous work in this area has used MTJs which benefit from a very large ( $>100\%$ ) magnetoresistance and are motivated based on application of these devices. However, as discussed in Sec. 1.5.1, the complex structure of an MTJ complicates the analysis of noise in these structures.

To reduce the complexity of our system, we measure a single magnetic layer using the anisotropic magnetoresistance (AMR) effect [64]. According to the AMR effect, the resistivity of a material depends on the angle  $\theta$  between the magnetization and the current through

$$\rho(\theta) = \rho_{\perp} + (\rho_{\parallel} - \rho_{\perp}) \cos^2(\theta), \quad (2.1)$$

where  $\rho_{\perp}$  ( $\rho_{\parallel}$ ) is the resistivity when the magnetization is perpendicular (parallel) to the current.

This effect arises from a scattering asymmetry in the conduction electrons caused by the orientation of the magnetization relative to the current and should not be confused with the Lorentz force which is responsible for the ordinary and planar Hall effects [45, 64, 65].

For signal-to-noise considerations and in order to ensure that our measurements are sensitive to the resistance change of the dot alone, four-terminal resistance measurements were made. Since this requires four separated non-magnetic contacts, the size of measurable devices was ultimately limited by the achievable spacing between contacts, around 50 nm. We also note that since the contacts were placed at the corners of a square dot as shown in Fig. 2.1, the voltage was not measured along a well-defined straight current path through the sample. This leads to a significantly larger AMR signal than would be obtained for a narrow wire [66] but does not change the results of our experiments.

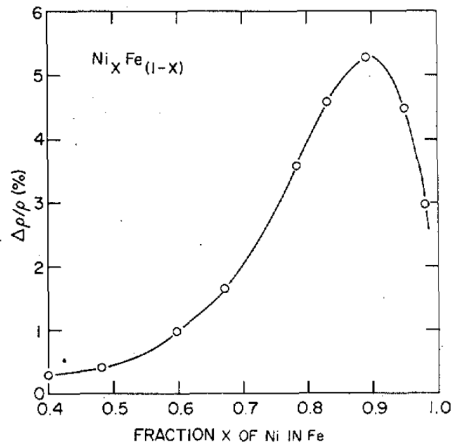


Figure 2.2: The magnitude of the AMR effect measured for  $\text{Ni}_x\text{Fe}_{1-x}$  alloys as a function of the concentration  $x$  of Ni in Fe. Permalloy, which consists of 80% Ni, has a large AMR value near the maximum of this curve. Reprinted, with permission, from Ref. [64]. Copyright 1975, IEEE.

### 2.1.3 Material Considerations

Two factors drive the choice of material used for the dots measured in this work. First, a material with low magnetocrystalline anisotropy is needed to avoid introducing magnetocrystalline energy barriers. At the same time, the AMR effect is material dependent and a sufficiently large signal is necessary to observe magnetic fluctuations. Fortuitously, both of these parameters can be nearly optimized in the same alloy of iron and nickel, Permalloy ( $\text{Ni}_{80}\text{Fe}_{20}$ ). Permalloy exhibits a large AMR effect (up to 6% in bulk [67]) as shown in Fig. 2.2 and at the same time has one of the lowest known crystalline anisotropy constants [50] as indicated in Fig. 2.3. Though some samples were fabricated using pure Ni, the small crystalline anisotropy of Ni was large enough to significantly complicate the analysis of the data.

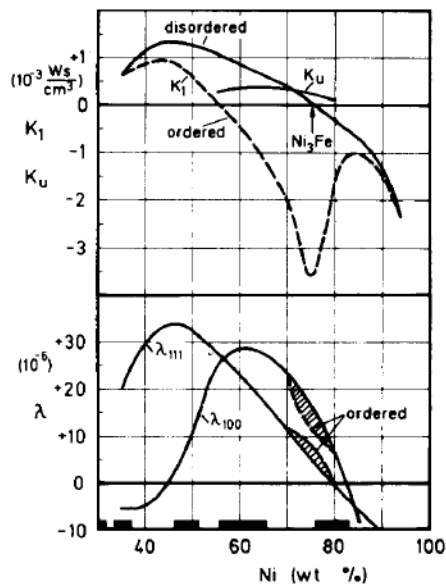


Figure 2.3: Variation in the crystalline anisotropy, and magnetostriction constants for alloying concentrations of Ni in FCC NiFe alloys. Bold lines on the concentration axis indicate industrially useful alloys. Note that both the magnetostriction and crystalline anisotropy values approach zero near 80% Ni. Reprinted, with permission, from Ref. [50]. Copyright 1980, Elsevier.

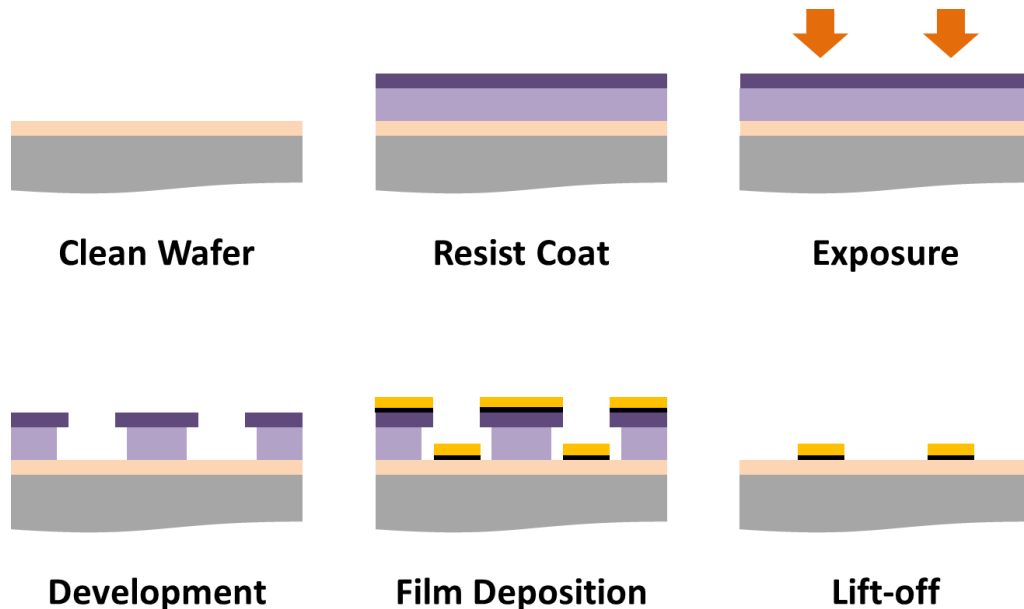


Figure 2.4: A side-view cartoon of the bilayer lift-off process generically applicable to the optical and EBL processes. A clean substrate is coated with two layers of resist with development selectivity. Depending on the resolution requirements, the resist is exposed with UV light or 100 keV electrons and developed to define the desired pattern in the top resist layer and undercuts in the bottom layer. The desired film is deposited everywhere on the substrate; the parts of the film deposited on top of the resist lift-off in a solvent bath leaving the desired pattern on the wafer.

## 2.2 Sample Fabrication

To investigate magnetic noise in thin Permalloy films patterned as square dots, a nanofabrication process relying on electron beam lithography (EBL) was developed to define the necessary sub-micron structures. Unambiguous identification of the magnetic noise required that the magnetic structures investigated be magnetically isolated. Thus, the structures were fabricated in a two-step process with the first step defining the square Permalloy dots and the second step adding non-magnetic electrodes for resistance measurements. Each of these steps, as well as an optical lithography step, utilized a lift-off process shown schematically in Fig. 2.4. We provide a brief overview of the fabrication process and its challenges here while technical details can be found in Appendix B. This work was completed using equipment in the Minnesota Nano Center (MNC) at the University of Minnesota and in Prof. Dan Dahlberg’s lab.



### 2.2.1 Substrate Preparation, Optical Lithography

Several practical considerations constrained the fabrication process and required certain preparations of the substrate prior to deposition the magnetic dot structures. The EBL system uses the electron beam as an SEM to align the write pattern to the substrate. The most efficient strategy for depositing the samples would define alignment marks in the same step as the dots and use these marks to align the contacts to the dots. However, sufficient contrast of any alignment marks is necessary for proper alignment. Contrast is achieved by defining alignment marks that a) use a material with a large atomic number to effectively scatter electrons and b) are sufficiently thick to produce a large number of scattered electrons. The 10 nm thick layer of Permalloy used for the dots did not produce sufficient contrast to allow for alignment marks to be simultaneously defined during this lithography step. The next best solution to this problem would be to deposit the dot contacts first using a material such as gold and also deposit the alignment marks in this step. However, this would corrugate the dots when deposited on top of electrical contacts and add additional sources of shape anisotropy. Thus, we deposited alignment marks in a preparatory optical lithography step. Since exposure of macroscopically large substrate areas for electrical contacts is time consuming when using EBL, coarse electrodes (everything but the central 20  $\mu\text{m}$  square of the pattern) were also defined in this step. The final deposition pattern for the 1 cm square substrates is shown in Fig. 2.5(a) which contains 9 sets of contacts, shown in Fig. 2.5(b), each available to connect to 4 magnetic dots. Note that the 4 fine alignment marks near the center of each pattern were necessary for high alignment accuracy as discussed in the next section.

The entire process began with clean 4-inch silicon wafers, purchased from NVE Corporation, pre-coated with 2000 angstroms of  $\text{Si}_3\text{N}_4$  to prevent stray electrical conduction between the sample leads. Following the recipe outlined in Sec. B.2, a bilayer of photoresist was spun onto the wafer which was exposed with the pattern of coarse electrodes and 20  $\mu\text{m}$  square alignment marks. A reference bar with 4-terminal contacts was patterned to allow measurement of the deposited film conductivity. Additional copies of this contact bar were added in each of the EBL steps for witness measurements of the films deposited in these steps.

After developing the resist, 30 nm of Ti and 70 nm of Au were deposited using electron beam evaporation. The Ti was used merely as a seed layer while Au was chosen for its low electrical resistivity, high atomic number, and resistance to oxidation. Following

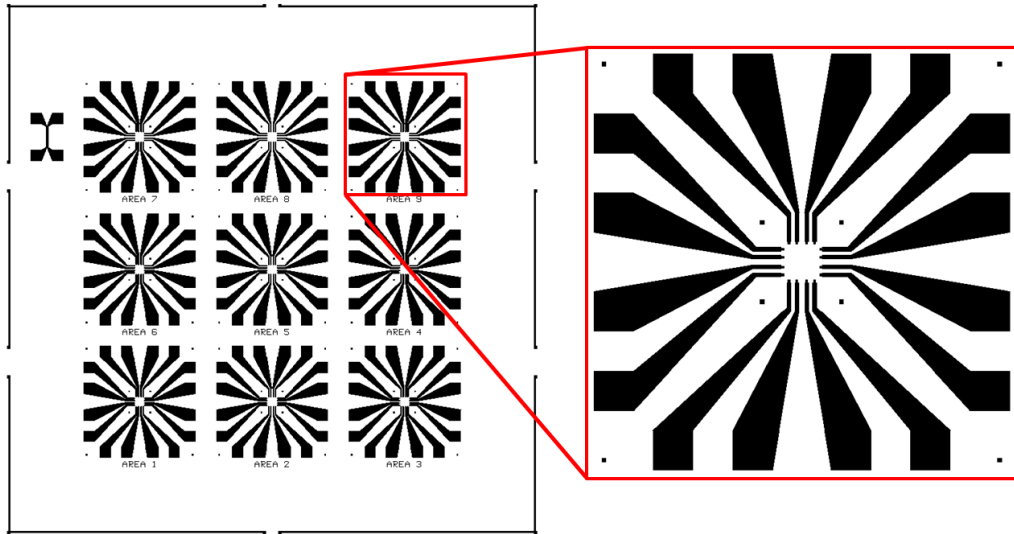


Figure 2.5: An overview of the pattern defined using optical lithography to produce high contrast alignment marks and the coarse sample contacts. The full pattern (left) contains 9 sets of contacts (right). The ‘I’ shaped structure in the upper right corner allows for 4-terminal witness measurements of the film properties; identical copies of this witness bar were included for the dot and contact depositions. The contact set (right) is approximately 2 mm wide and contains two sets of four  $20\ \mu\text{m} \times 20\ \mu\text{m}$  alignment marks. The fine alignment marks at the center are spaced by  $400\ \mu\text{m}$  to provide alignment of the final dot and contact exposures without requiring the stage within the EBL tool to be moved.

deposition, lift-off was performed and the wafer was diced into 60 individual 1 cm square dies.

### 2.2.2 Electron Beam Lithography

Optical lithography is generally limited to feature sizes comparable to the wavelength of the light used, 193 nm in the case of I-Line ultraviolet (UV) light. However, the wavelength of an electron can be much shorter than UV light ( $\sim 4\ \text{pm}$  for a 100 keV electron) allowing EBL to achieve far higher lithographic resolution. In fact, the most significant resolution limits of EBL are imposed by the chemical properties of the polymer resists and the back scattering of the electrons. All samples discussed here were patterned using an EBPG 5000+, built by Vistec Electron Beam GmbH, with an accelerating voltage of 100 keV. The high electron beam energy offers achievable beam sizes of  $< 4\ \text{nm}$  while the resist used for the work discussed here is generally limited to around 20 nm feature sizes.

As in the photolithography step, a bilayer resist recipe was used. Bilayer resist is

critical for this work since a single layer resist results in poor lift-off as shown in Fig. 2.6. Specifically, for single layer resists, fencing occurs at the border of the pattern as material is deposited on the sidewall of the resist. In the worst cases, fencing causes retention of the unwanted part of the film deposited on top of the resist. Since fencing and retention alter the final sample shape, they introduce additional shape anisotropies, affect subsequent resist coatings, and interfere with electrical continuity between the dots and electrodes.

For the top, imaging layer of the bilayer resist, poly-methyl methacrylate (PMMA) was used for its high sensitivity to electron beam radiation. The thickness of this layer is not significant but was kept thin ( $\sim 30$  nm) to improve resolution. Polymethylglutarimide (PMGI) was used for the bottom layer resist since it provides development selectivity, i.e. its developer does not affect PMMA and vice versa. Using a layer of PMGI approximately three times that of the deposited film thickness allows clean lift-off. In addition to the constraints on resist thicknesses, the number of electrons exposed to the sample (termed the dose), the developer concentrations, and development time were adjusted to produce high resolution features. Using the parameters listed in Sec. B.3, magnetic dots were successfully fabricated with side lengths down to about 100 nm.

For each of the EBL steps, the pattern of contacts and dots was defined using the

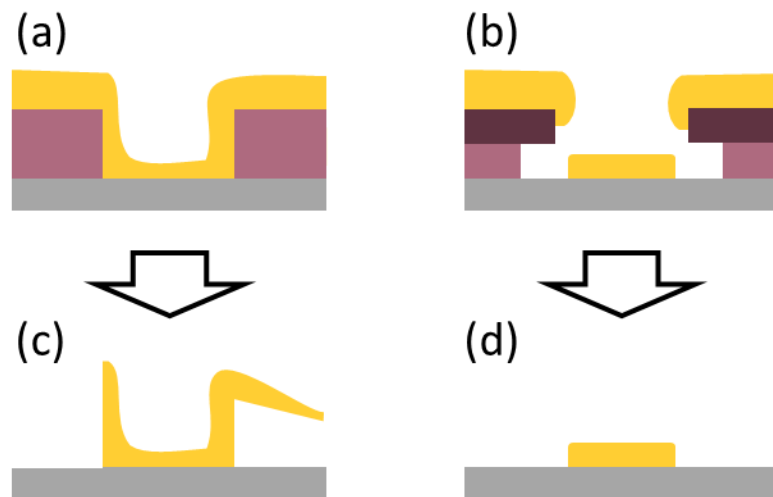


Figure 2.6: A side-view cartoon comparing (a) monolayer and (b) bilayer resist lift-off results for a conformal deposition process such as sputtering. (c) The monolayer resist suffers from fencing problems (left side) and retention problems (right sides) due to the sidewall coverage of the resist. (d) The bilayer avoids these problems by providing an undercut in the side-wall profile that prevents complete metal coverage of the side-wall.

ICWIN layout software and exported in the Graphic Database System (GDSII) file format. Using the proprietary software Layout Beamer and Cjob developed by Vistec, this pattern was translated into an executable job file. This job file aligned the designed pattern to the pre-fabricated alignment marks on the die of interest and specified the pattern rastered by the electron beam. The electron beam size was adjusted to ensure that the convolution of its shape with the desired pattern produced the necessary resolution. The dot and the parts of the contacts directly connected to the magnetic dots were patterned using the highest resolution beams, 5 nm at 200 pA. However, since high resolution beams require long write times, lower resolution, higher current beams were used for low resolution features.

As an additional note, the arrangement of coarse contacts on the die was chosen to optimize the alignment procedures. The electron optics of the EBPG can deflect the beam only within a 500 nm square. To achieve the highest alignment, 4 alignment marks were placed at the corners of a 400 nm square at the center of each set of 16 contacts in the photolithography step as shown in Fig. 2.5(b). The EBPG then located the alignment marks and exposed the resist without translating the sample stage and introducing alignment errors. Using this procedure, alignments better than 10 nm were achieved between the dot and contacts.

### 2.2.3 Deposition

The two primary considerations for depositing the materials used in fabricating the samples are 1) the directionality of the deposition procedure and 2) the quality of the deposited magnetic materials. We consider each of these limitations in turn below.

Deposition techniques which allow deposited material to travel in a straight-line path from source to substrate are preferred in lift-off procedures since they do not produce conformal coatings. In the limit of thick films, conformal coatings cover all surfaces of a substrate including the side-walls of the resist in much the same way that a thick snowfall results in a smoothed covering of the landscape. This prevents clean lift-off causing problems similar to those in Fig. 2.4. Thus, techniques such as electron beam or thermal evaporation are preferred so that only substrate areas exposed to the source along the line-of-sight are coated. In the case of bilayer resists, directional deposition results in near exact copies of the suspended top-layer resist in the final deposited features. These deposition techniques require the vacuum pressure to be kept low enough to maintain

a mean free path longer than the source-substrate distance. Since the 4-terminal non-magnetic contacts required the highest resolution, these were deposited using the CHA electron beam evaporation system in the MNC (pressure  $6 \times 10^{-7}$  Torr, mean free path  $>1$  m) with a final film stack of 10 nm Ti and 20 nm Au.

While evaporative techniques yield higher resolution samples, sputter deposition techniques offer better control of the final sample material composition. Maintaining the atomic composition of  $\text{Ni}_{80}\text{Fe}_{20}$  for permalloy is necessary to ensure a low crystalline anisotropy. Evaporative techniques lack composition control since the constituent metals will have different evaporation rates from the source material. By contrast, sputtering techniques utilize room temperature solid targets; the material is released from the target via kinetic impact of the ionized sputtering gas (Ar in our case). The magnetic dots in this work were deposited using DC magnetron sputtering in the Dahlberg lab at an Ar pressure of 3 mTorr with sputtering rates of about  $0.5 \text{ \AA/s}$ . The resultant films appear to be polycrystalline and SEM micrographs indicate grain sizes of  $\sim 10$  nm.

A Ta seed layer was used included in the dot deposition because previous work found this to improve the magnitude of the AMR effect [68]. A Ta capping layer was also used to prevent oxidation of the Permalloy. Note that Ta is also a poor conductor which reduces the fraction of current shunted through the seed and capping layers. A 3 nm seed and capping layer were used for 10 nm thick Permalloy films.

## 2.3 Measurement Techniques

### 2.3.1 Current Source

For the resistance measurements, a direct current (DC) was supplied to the sample to avoid introducing an artificial frequency into the noise measurements. For the same reason, the current supply was powered with a 1.5 V D-cell battery. A  $100 \text{ k}\Omega$  potentiometer was used to adjust the magnitude of the current with the voltage across a  $100 \text{ }\Omega$  series resistor used to measure the current. A current of about  $150 \text{ }\mu\text{A}$  produced a reasonable signal-to-noise ratio without producing significant ohmic heating (a temperature increase of  $<0.2 \text{ K}$  was observed in measurements on films with sizes similar to our samples when the current was raised from  $180 \text{ }\mu\text{A}$  to  $235 \text{ }\mu\text{A}$ ) or other effects that could degrade or destroy the samples. At current levels above  $\sim 1 \text{ mA}$ , noticeable changes in the magnetic behavior of the samples were observed with complete breakdown occurring at current densities around

$8 \times 10^7$  A/cm<sup>2</sup>. Aluminum wirebonds provided electrical connection from the sample contacts, shown in Fig. 2.5, to the current supply and voltage measurement instruments. The circuit was grounded, as discussed in Appendix C, at the negative-voltage terminal which greatly reduced the background noise sources and the number of samples destroyed by electrostatic discharge (ESD).

### 2.3.2 Pre-amplifier

The  $\sim 1.5$  mV sample voltage produced by the DC current (150  $\mu$ A) was first amplified by a factor of 200 with a low-noise battery powered Stanford Research Systems (SRS) 560 pre-amplifier. This initial gain reduced the noise floor of the measurement by about 2 orders of magnitude above 1 kHz and by a factor of 10 at 1 Hz as shown in Fig. 2.7. Gain settings larger than 200 did not noticeably improve the noise floor or the signal-to-noise ratio of the DC resistance measurements. To allow simultaneous measurement of the sample resistance during noise measurements, the pre-amplifier was DC coupled with no high-pass filtering. The pre-amplifier was battery powered using the internal battery; excess noise at 60 Hz and higher harmonics appear when the pre-amplifier is powered by a wall outlet.

In the data presented in this thesis, the background noise from the pre-amplifier and spectrum analyzer has been subtracted; thus all data represents noise intrinsic to the sample, contacts, and leads. The background was measured with the pre-amplifier input shorted. When the background subtraction method was applied to data for a 14 k $\Omega$  resistor, the resultant spectra agreed with Eq. 1.1 to within uncertainty. Thus, we present our data having subtracted the pre-amplifier noise and the noise floor can be interpreted as the Johnson-Nyquist noise of the voltage contacts.

### 2.3.3 Resistance Measurements

The DC resistance of the dot was determined by measuring the sample voltage with a Keithley 2000 Digital Multimeter and dividing by the current provided by the current source (measured using a series resistor). The multimeter readings were transferred to a computer for analysis through an IEEE-488 General Purpose Interface Bus (GPIB) connection using National Instruments LabView software to control the data exchange. Time dependent measurements were limited to  $< 10$  Hz by the single point sampling rates achievable using the GPIB interface. Attempts to use the buffer of the instrument lacked

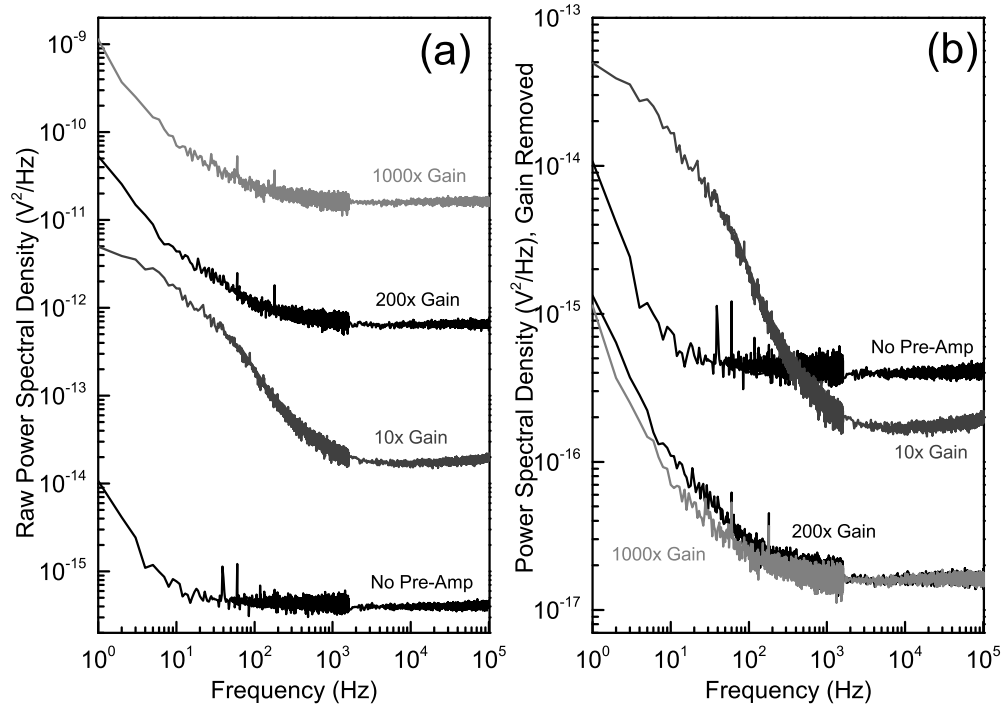


Figure 2.7: (a) PSDs measured for the SRS 560 pre-amplifier with a shorted input at the gain values indicated and compared to the case where the short was applied directly to the HP35670A spectrum analyzer (No Pre-Amp). (b) When the gain is removed from the data, it is apparent that pre-amplifier gains of 200 and above provide the best noise floor achievable,  $\sim 4 \text{ nV}/\sqrt{\text{Hz}}$ . The low frequency data was averaged over 100 spectra while the high frequency data contains 500 averages. Uniform windowing was used and the spectrum analyzer was AC coupled. Using battery power, the pre-amplifier input was set to GND under battery power with no filters applied and was placed more than 25 cm from the spectrum analyzer (additional noise peaks are observed if the separation distance is too small).

timing accuracy sufficient for quantitative measurements of the RTN. In future studies, this low frequency limitation could be avoided by using a real time oscilloscope.

### 2.3.4 Spectrum Analyzer and Noise Measurements

As discussed in Sec. 1.2.1, noise measurements are usually analyzed by examining the Fourier transform of a physical quantity measured over some time duration. Experimentally this is accomplished using a spectrum analyzer, a Hewlett-Packard (HP) 35706A for these experiments, which directly computes the fast Fourier transform of the measured

time dependent voltage and outputs the resultant PSD. To avoid an anomalously large DC component of the spectra, the analyzer was AC coupled to the voltage input. Since true stationary noise signals are not periodic, uniform windowing was used. Non-uniform windowing would result in spill-over of any measured frequency component into adjacent frequency components (i.e. peaks such as that produced by 60 Hz backgrounds broaden into the 59 and 61 Hz bins).

The frequency resolution of the analyzer was set to the maximum of 1600 lines which allowed 3.2 decades of frequency to be measured. The lowest frequency component is only limited by the length of the measured time spectra (measuring 1 Hz data requires  $\sim 30$  s per data point if 30 spectra are averaged). The upper limit of our measurement bandwidth, 102.4 kHz, is dictated by the frequency limits of the HP 35706A. Since our measurement techniques probe the voltage of the sample, all of measured PSDs are reported in the units of  $V^2/\text{Hz}$ . Conversion of these results to a PSD of the magnetization itself can be computed using the details of the AMR effect and the magnetic material in question as discussed elsewhere [34].

### 2.3.5 Magnetic Field

The magnetic field in our experiments was applied using standard electromagnets with a soft-iron core. The magnetic field was measured using an F. W. Bell Gauss-meter. The output signal voltage from the Gauss-meter varied by 0.5 Oe even at the highest sensitivity setting. This uncertainty did not originate from true fluctuations in the field since no resistance changes in the samples were observed which correlated with the Gauss-meter fluctuations.

To improve the field measurement we interpolated the correct value using the control voltage sent to the electromagnet power supply, which could be measured with much higher precision than the field. Both the output voltage controlling the electromagnet and the input Gauss-meter measurement were recorded. A polynomial fit was then applied to this data and the applied field values were calculated from this fit using the control voltage data. In essence, this process smoothed the uncertainty introduced by the Gauss-meter. This procedure was repeated each time data was recorded since the electromagnets were slightly hysteretic and a universal fit was impractical.



### 2.3.6 Temperature Control

Temperature dependent measurements were made using an Advanced Research Systems closed-cycle refrigerator with a demonstrated base temperature below 4 K. A Lakeshore 335 temperature controller regulated the temperature of a reference thermometer. The temperature could be stabilized to within 0.5 K for measurements made at temperatures ranging from 50 K to 320 K. Using GE varnish to achieve thermal contact, a second thermometer was connected to the copper stub on which the sample was mounted. The sample temperature was recorded using this thermometer. The cryostat introduced several noise sources discussed in Appendix C. However, the majority of this extraneous noise was limited to narrow peaks in frequency space which did not impact our ability to measure the broad signals associated with RTN and  $1/f$  noise.

### 2.3.7 Background Noise and Electrostatic Discharge Considerations

Significant efforts were made to reduce the number of background noise sources in the experiment. Details of the steps undertaken to produce a low noise experimental setup are described in Appendix C. In general, faraday shielding of the samples in conductive enclosures, proper grounding, and the use of battery power wherever possible caused the most significant reductions in noise backgrounds.

The small cross-sectional area of the sample contacts made them especially susceptible to the high transient currents associated with electrostatic discharge (ESD). Several procedures adopted to mitigate these effects are also included in Appendix C. These primarily involve proper grounding of the sample, experimental setup, and experimentalist.

## 2.4 Micromagnetic Simulations

To aid in interpretation of our experimental results and provide theoretical justification for our conclusions, simulations of the magnetization in our dots were performed in collaboration with C. T. Weigelt and R. H. Victora in the Department of Electrical and Computer Engineering at the University of Minnesota.

### 2.4.1 Landau-Lifshitz-Gilbert Equation

All micromagnetic simulations are based on the numerical integration of the Landau-Lifshitz-Gilbert (LLG) equation [69, 70]. The LLG equation describes the motion of the magnetization in the presence of an effective magnetic field and incorporates a phenomenological damping term [70]. The effective magnetic field incorporates the effect due to all magnetic energies discussed in Chapter 1, the details of which can be found elsewhere [69, 71]. Extended magnetic samples are treated by subdividing the sample into small cells with dimensions comparable to the exchange length of the simulated material.

### 2.4.2 LLG Micromagnetics Simulator

Some of the simulations were performed by the author utilizing the LLG Micromagnetics Simulator software package developed by M. R. Scheinfein [72]. The built-in parameters for Permalloy were used for these simulations and the sample was discretized into 10 nm square elements. All simulations using this software package were done ignoring any thermal effects, i.e., zero temperature simulations.

### 2.4.3 Finite Temperature Simulations

Prof. R. H. Victora and his graduate student C. T. Weigelt both in the Department of Electrical and Computer Engineering at the University of Minnesota developed additional simulations of the LLG equation to incorporate the effects due to finite temperature [58]. Temperature is included by adding a scaled random vector to the effective magnetic field encountered by each magnetization cell. Simulations were conducted for 200 nm square Permalloy dots 10 nm thick at 300 K with zero crystalline anisotropy, an exchange stiffness constant of 1  $\mu\text{erg}/\text{cm}$ , and saturation magnetization of 800  $\text{emu}/\text{cm}^3$ . This simulation volume was discretized into 10 nm cells.

## Chapter 3

# Quantifying the Energy Landscape

The magnetic energy landscape associated with the square geometry of our samples provides the fundamental explanation for the magnetic noise observed in this system. In this chapter, we present measurements of the magnetic energy landscape, describe a model which explains the observed magnetic behavior, and conclude by demonstrating that micromagnetic simulations support our conclusions.

### 3.1 Identifying the Magnetization State through AMR

#### 3.1.1 Definition of Angle

As discussed in Sec. 2.1.2, we utilize the AMR to correlate a measured sample resistance to the magnetization state of our sample. To describe the direction of the magnetization, we must define a particular direction as  $0^\circ$ . Equation 2.1 provides this definition naturally. However, it describes the dependence of the resistivity of a magnetic material on the angle between the current and magnetization while our measurements are of the total sample resistance. In addition, both the current and magnetization are not uniform within our samples so if the direction of the current is taken to be zero degrees, this definition would vary within the sample. Thus, we make the simplifying assumption that dominant current path is parallel to the line connecting the current leads of our sample and define this direction as zero degrees, as shown in Fig. 2.1. All inferred net magnetization directions and applied magnetic fields are described with reference to this definition of angle.

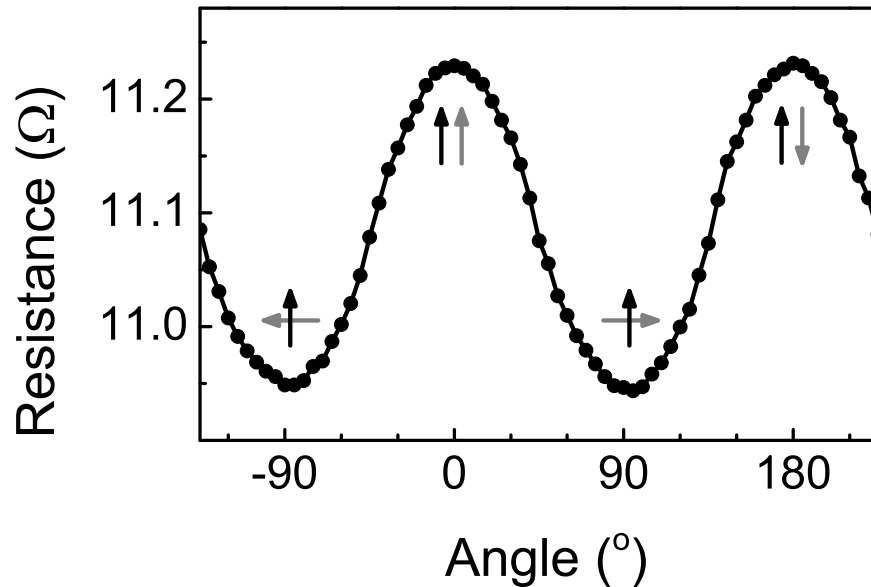


Figure 3.1: The resistance of a 350 nm square dot measured as a function of applied field angle at a fixed magnetic field of 251 Oe. At this field, the magnetization is nearly uniform and parallel to the applied field. The pairs of arrows indicate the direction of the magnetization (gray) relative to the current (black) at the maxima and minima of the data. Note that a given resistance value may correspond to up to four different magnetization directions. Reprinted, with permission, from Ref. [61]. Copyright 2013, AIP.

### 3.1.2 Large Field AMR Rotational Hysteresis Loops

As an example of how to interpret the magnetization direction using AMR, consider Fig. 3.1, where the measured resistance of a dot is plotted as a function of applied field angle. In this case, a large magnetic field is used which is sufficient to force the magnetization to align to the field. The resistance varies sinusoidally with applied field in good agreement with Eq. 2.1. A high resistance is observed when the magnetization is colinear with the current while a low resistance is observed when the magnetization and current are perpendicular. However, there is not a one-to-one relationship between the measured resistance and the magnetization direction; for example, magnetization directions of  $0^\circ$  and  $180^\circ$  have the same resistance. Thus, knowledge about the magnetic history of the sample must be incorporated when inferring the net magnetization direction.

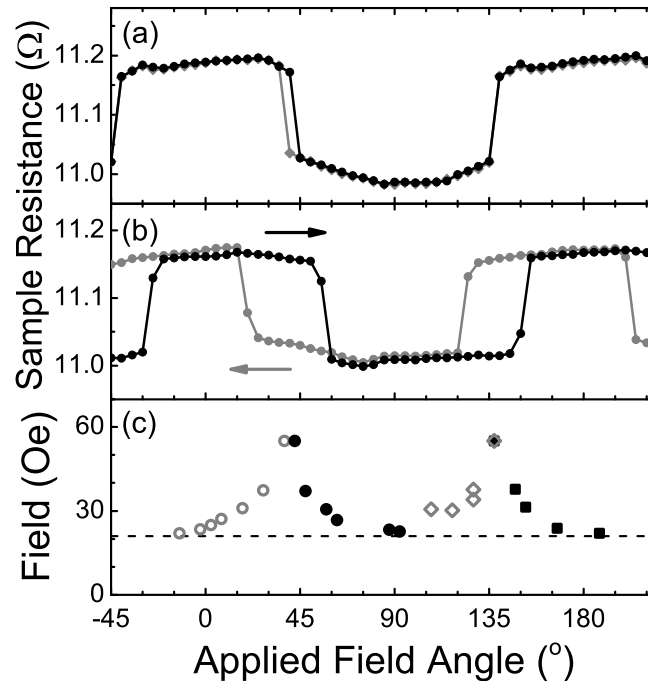


Figure 3.2: Rotational hysteresis loops measured for the same 350 nm dot as in Fig. 3.1. The sample resistance is plotted as a function of applied field angle for the fixed applied field magnitudes of (a) 55 Oe and (b) 31 Oe. Arrows in (b) indicate the direction of rotation of the applied field. (c) The applied field magnitude is plotted as a function of the angle at which the largest resistance changes are observed for both rotation directions (open vs. closed symbols) and for the hysteresis point around 45° (circles) and 135° (squares). Reprinted, with permission, from Ref. [61]. Copyright 2013, AIP.

## 3.2 Rotational Hysteresis Data

### 3.2.1 Rotational Hysteresis

The data in Fig. 3.1 was taken at a sufficiently large field that the Zeeman energy overwhelmed all other magnetic energies in the sample and thus the magnetization was parallel to the applied field. However, for similar data taken at smaller applied fields, the influence of the configurational anisotropy of the square dots becomes apparent, as shown in Fig. 3.2(a). Large jumps in the resistance occur at angles corresponding to the diagonals of the square samples, odd multiples of 45°. The configurational anisotropy energy in our samples creates local energy minima in the directions parallel to the dot edges that produce preferred directions of the magnetization. The jumps observed in the resistance

correspond to the magnetization becoming dislodged from one minimum and rotating immediately to the other minimum once sufficient torque is provided by the applied field. The total amplitude of the resistance change associated with rotation of the magnetization through  $90^\circ$  is smaller than in Fig. 3.1 due to non-uniformities in the magnetization discussed in greater detail in Sec. 3.3.3.

At small applied magnetic fields, as shown in Fig. 3.2(b), hysteresis appears when the field is rotated in opposite directions. In this case, the angle between the magnetization and the applied field increases until sufficient torque is developed to dislodge the magnetization from the energy minima. This hysteresis grows as the magnitude of the field is reduced further until, at sufficiently small applied fields, the resultant torque on the magnetization is insufficient to dislodge it from its energy minimum. The widening of the rotational hysteresis is shown in Fig. 3.2(c), where each plotted point corresponds to the applied field angle necessary to switch the magnetization for a given applied field magnitude. The horizontal distance between two points at a given field represents the width of the observed rotational hysteresis.

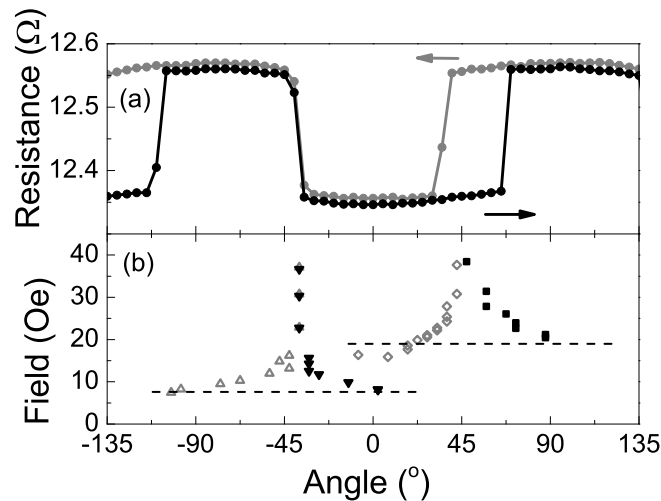


Figure 3.3: Rotational hysteresis measurements of a 250 nm dot plotting (a) the resistance as a function of applied field angle at a fixed field of 24 Oe and (b) the applied field values as a function of the applied field angle where the largest change in resistance occurs. Arrows in (a) indicate rotation directions. Note that unlike the data in Fig. 3.2, the minimum field necessary to rotate the magnetization differs for the data associated with each corner; 18 Oe is required at  $45^\circ$  while only 7 Oe is required at  $90^\circ$ .

### 3.2.2 Differences in Rotational Hysteresis at Adjacent Corners

The rotational hysteresis observed in our samples was not always the same when the magnetization was rotated across the two diagonal directions of the square dot. A larger amount of rotational hysteresis was observed at  $45^\circ$  than at  $-45^\circ$  for the sample shown in Fig. 3.3. In some cases the minimum field needed to rotate the magnetization also varied between rotation directions for a given corner; in Fig. 3.3 the minimum hysteresis at  $45^\circ$  differs by about 3 Oe between the two rotation directions. These effects can easily be explained by sample imperfections introduced when the dots were fabricated. A rhomboidal shape or rounded corners could explain differences in rotational hysteresis between the two dot diagonals, and imperfections that are not reflection symmetric might explain rotation direction differences.

Every effort was made to produce ideal square dots but slight deviations were inevitable in fabrication. A set of SEM micrographs in Fig. 3.4 demonstrates the variation between 4 dots intended to be identical square dots. Of particular note is the variation in edge roughness and roundness of the square corners which could account for variation in the rotational hysteresis between the two corner directions. Asymmetries could likewise account for the differences between rotation directions. However, data taken at  $180^\circ$  produced identical behavior; that is, when the magnetization direction was reversed and the same corner was measured, the results were unchanged. This indicates that no exchange bias or other symmetry breaking effects were present at room temperature in our samples [73, 74].

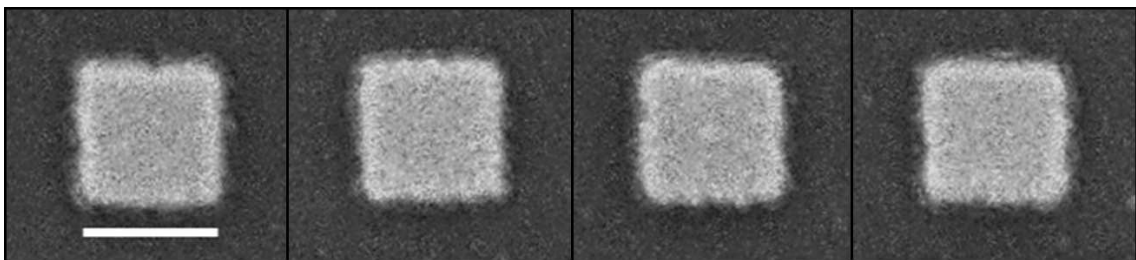


Figure 3.4: Four SEM images of 200 nm dots fabricated without electrodes illustrating the edge roughness and imperfections introduced by the fabrication process. All four dots were defined on the same chip; a 200 nm scale bar is provided for reference.

### 3.3 Easy-Axis Linear Hysteresis Data

Based on the rotational hysteresis data, the samples indicate a preference for the magnetization to align parallel to one of the edges of the square, i.e. the easy axes of the sample. To explore the magnetic properties of the dots further, we fix an applied field direction and investigate the magnetization as a function of applied magnitude, measuring the AMR in a fashion similar to a hysteresis loop.

#### 3.3.1 Interpretation of the AMR Data

The linear hysteresis loops presented below can be interpreted as traditional  $M$  vs.  $H$  loops folded back upon themselves (technically the AMR probes the square of the magnetization). Consider for example, the plot of the dot resistance as a function of the applied field magnitude in Fig. 3.5 for a field aligned parallel to the primary current direction. This measurement can be directly compared to micromagnetic simulations of the magnetization for a dot of the same size in Fig. 3.6. From Eq. 2.1 we note that the sample resistivity does not change if the magnetization is rotated by  $180^\circ$ . Thus, the resistivity

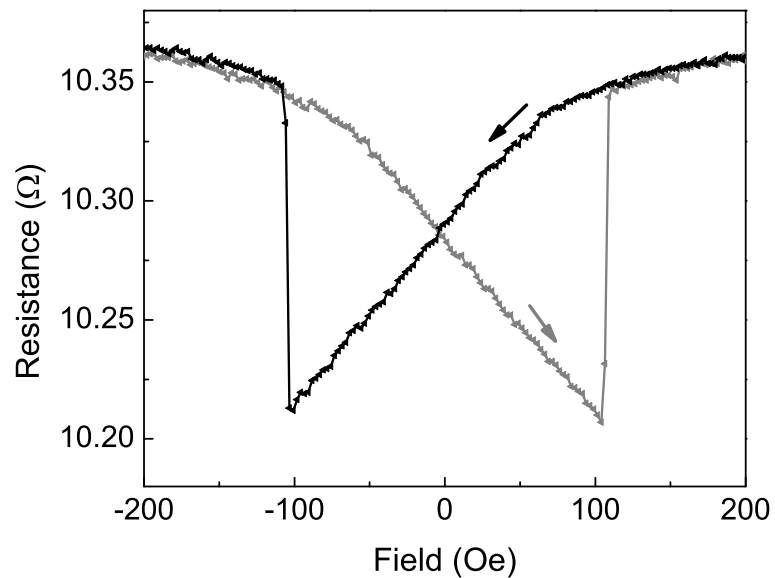


Figure 3.5: Resistance versus applied field for a 300 nm dot measured with the applied field oriented at  $0^\circ$ . Arrows denote sweep directions.



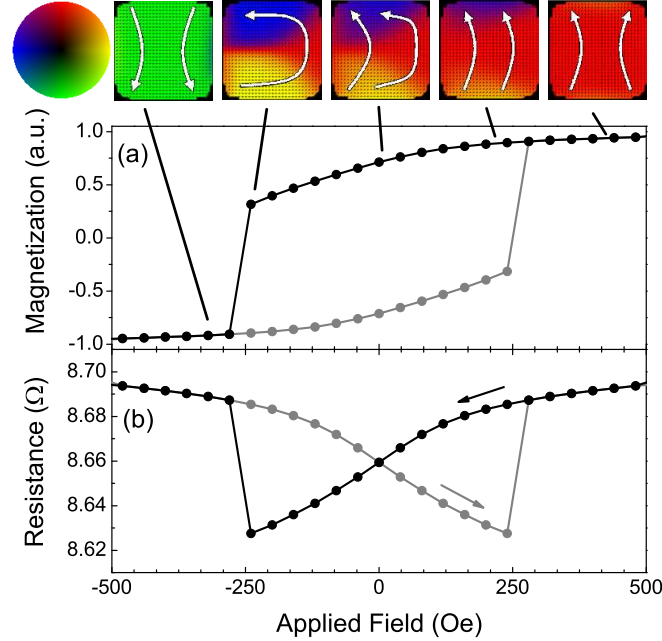


Figure 3.6: Simulated hysteresis loops for a 300 nm square permalloy dot where the (a) the normalized magnetization and (b) resistance are plotted as a function of applied field edge of the square dot. Resistance is computed assuming a uniform current collinear with the applied field direction and computing the voltage at opposite sides of the sample (AMR ratio of 1.2%, 10 nm discretization). Vector plots shown approximate the magnetization configurations where the colors correspond to the in-plane directions indicated in the color wheel; arrows in (b) indicate field sweep directions. Simulations were conducted by the author using the LLG Micromagnetic Simulator [72].

for the magnetic state at a large positive magnetic field should be identical to the resistivity when a large negative field is applied to the sample. This is reflected in the data in Fig. 3.5; at large positive (or negative) magnetic fields the same high resistance state is observed since the magnetization is saturated parallel (or anti-parallel) to the current direction.

### 3.3.2 Observation of Well-Defined Coercivities

Extending our interpretation of the linear hysteresis data further, we can identify the field required to reverse the magnetization. Simulations indicate that the net magnetization will remain oriented parallel to an edge of the square dot until a sufficiently large magnetic field in the opposite direction causes it to abruptly switch by  $180^\circ$ . This leads to very square

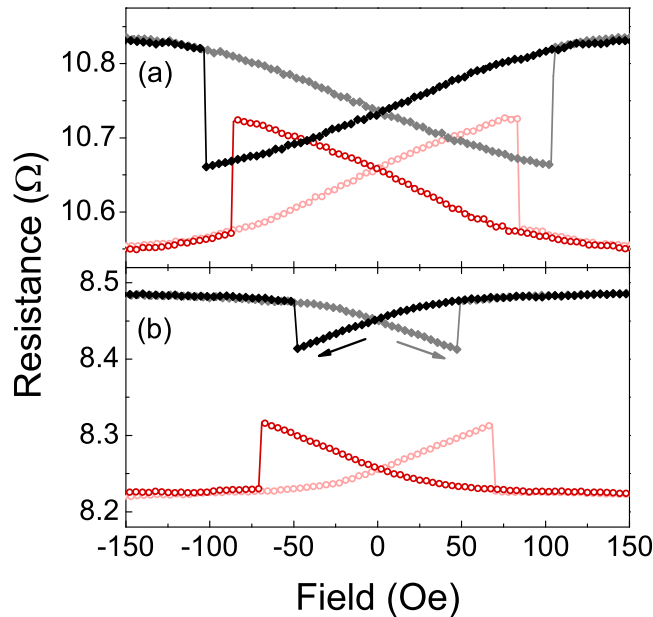


Figure 3.7: Resistance plotted as a function of applied field for a (a) 400 nm dot and (b) 200 nm dot at  $0^\circ$  (solid black diamonds) and at  $90^\circ$  (open red circles). Arrows indicate sweep directions with return sweeps plotted in a lighter color. Note that at remanence, the relative difference in the two resistance states for the 200 nm is approximately 90% of the full magnetoresistance while it is only it is roughly 30% in the 400 nm case due to differences in the remanent magnetization between the dots.

hysteresis loops with a single large change in the magnetization seen in Fig. 3.6. The AMR data shows this abrupt change in magnetization as a single large jump in the resistance of the sample. Clearly the AMR data indicates, as does the simulated magnetization data, that the magnetization does not simply rotate by  $180^\circ$ ; the gradual change in resistance prior to the abrupt rotation is discussed in the next section.

In Fig. 3.7, we plot the linear hysteresis loops for applied fields at both  $0^\circ$  and  $90^\circ$ . In this case, the  $90^\circ$  data is similar to the  $0^\circ$  data but starts at a low value of resistance based on Eq. 2.1. Since our samples are symmetric we expect the coercivity observed along both axes to be the same and our observations confirm this prediction. However, as in the rotational data, sample imperfections sometimes led to differing coercivities between the two easy axes. To emphasize the benefits of measuring isolated individual dots, note that experiments conducted by Cowburn et al., [54, 56] on arrays of dots were unable to resolve these well-defined coercivities due to the effects of averaging in their measurements.

### 3.3.3 Effects Due to the Demagnetization Energy

The gradual change in resistance prior to the abrupt jump at the coercivity can be explained by examining the vector field of the magnetization obtained from simulations of the square dots conducting using the LLG Micromagnetics Simulator [72] at different points along the hysteresis loop shown in Fig. 3.6. At large applied fields the magnetization aligns almost uniformly with the applied field resulting in the largest (or smallest) resistance observed in the  $0^\circ$  (or  $90^\circ$ ) data in Fig. 3.7. At smaller applied magnetic fields, the resistance exhibits a bent magnetic state with a net magnetization still parallel to the original field direction but with a smaller magnitude. If the voltage differences are integrated along the current path in the sample using Eq. 2.1, the resultant resistance will decrease (increase) as the magnetization bends for the cases when the net magnetization is collinear (perpendicular) to the current. The bending of the magnetization originates from the competition between the exchange and magnetostatic energies within the sample. The slight bend in the magnetization causes a larger decrease in magnetostatic energy than the accompanying increase in exchange energy leading to a lower magnetic configuration energy state.

Comparing the hysteresis loops for large and small dots provides additional experimental evidence supporting these conclusions. In a 400 nm dot, as shown in Fig. 3.7(a), the magnetoresistance between the collinear and perpendicular magnetization states at remanence is less than 30% of the total AMR. By contrast, in a 200 nm dot, Fig. 3.7(b), the magnetoresistance difference is about 80% of the total AMR. This suggests that the magnetization bends more strongly in the larger dot where the magnetostatic energies exert more influence while the magnetization is more uniform in smaller dots with relatively larger exchange energy.

### 3.3.4 Observation of 4 Distinct Magnetic States

Our measurements of the linear hysteresis loops further confirm the existence of 4 low-energy magnetic states. In Fig. 3.7 note that there are two distinct resistance states at zero field, with the data for the  $0^\circ$  and  $90^\circ$  applied fields indicating different resistance values. Furthermore, at small positive or negative fields we observe 4 distinct resistance values. From our interpretation of the resistance based on the vector field plots in Fig. 3.6 we recognize that there are four distinct low-energy orientations of the remnant magnetization that will give rise to these four distinct resistance values. Thus, measurements of the

easy-axis hysteresis and the rotational hysteresis both indicate a four-fold symmetry to the magnetic energy landscape in the square dots.

### 3.3.5 Observation of Vortex Magnetic States

A magnetic vortex dramatically lowers the magnetostatic energy of the system since the magnetization curls completely within the sample as shown in Fig. 1.5 [52]. In this state the magnetization is never perpendicular to the edge of the sample (with the exception of the core where it is perpendicular to the plane) and all pairs of spins on opposite sides of the sample have a low-energy, anti-parallel alignment. The square dot geometry strongly suppresses vortex magnetic states because bending of the magnetization at the corners results in a large exchange energy cost; this vortex suppression for small square dots is indicated in Fig. 1.4.

However, in circular dots, no corners exist to suppress vortex magnetization and for

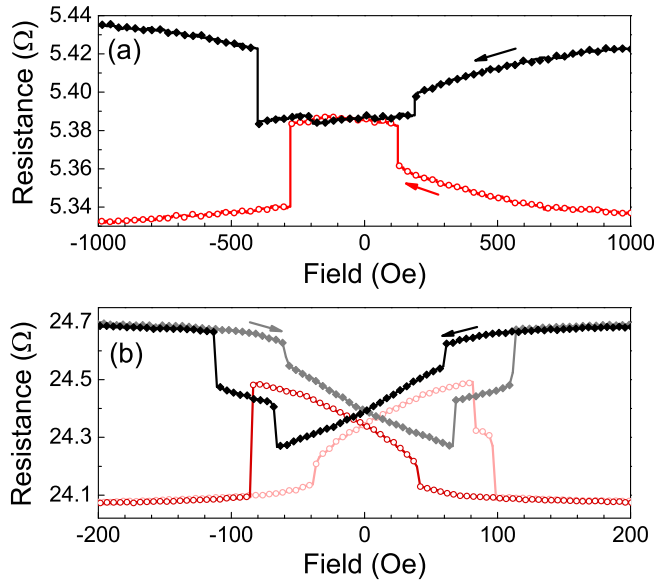


Figure 3.8: Resistance vs. applied field for (a) 200 nm circular and (b) 500 nm square magnetic dots for applied field directions of  $0^\circ$  (closed black diamonds) and  $90^\circ$  (open red circles). For the circular dot, one resistance value is observed at zero applied field indicating the presence of a vortex magnetic state. The large square dot does not exhibit a vortex state at remanence but the resistance states that occur after the field has swept past zero (between 80 Oe and 120 Oe in the  $0^\circ$  data) may be a vortex state. Arrows denote field sweep directions with one direction plotted in (a) and both directions in (b).

circular dots of comparable size to our samples it is the ground state magnetization configuration. Figure 3.8(a) shows the measured resistance of a circular dot as a function of applied field for several field directions. Large abrupt resistance changes at large fields correspond to the formation and annihilation fields for the vortex, above which the dot will exhibit a single-domain magnetization state. Since the vortex core will move to the center of the dot at zero field regardless of the applied field history (assuming there are no defect pinning sites), only one resistance value is observed at zero field for all applied field directions. The presence of two resistance values at zero field supports our conclusions that the magnetization in our square samples is quasi-single domain and does not form a vortex state. We do note that several large square dots with side lengths of 500 nm or 1  $\mu\text{m}$  did exhibit some hysteresis loops with states that may be explained by the formation of a vortex, as shown in Fig. 3.8(b).

### 3.4 Non-Easy-Axis Hysteresis Loops

Hysteresis loops measured at applied field directions other than the square dot easy axes offer additional insight into the nature of the magnetization reversal process.

#### 3.4.1 Near Easy-Axis Hysteresis Loops: Reduced Coercivity

For applied field directions near the easy-axis direction, the coercivity of the loop decreases. As shown in Fig. 3.9(a), loops at applied field directions of  $5^\circ$ ,  $10^\circ$ , and  $15^\circ$  away from the easy axis show a qualitatively similar field dependence to easy-axis loops. At very large fields the resistance is slightly different for the  $10^\circ$  and  $15^\circ$  data since the magnetization is saturated in the new applied field directions as expected from Eq. 2.1. However, at smaller fields, the hysteresis loops for these applied field directions have nearly identical field dependencies as observed for the easy-axis data.

#### 3.4.2 Near Diagonal Hysteresis Loops: Evidence of Rotation

As the applied field direction moves further from the easy axes, additional jumps in the hysteresis loops appear suggesting the magnetization completes a series of  $90^\circ$  rotations during reversal. A hysteresis loop for an applied field direction of  $40^\circ$  is plotted in Fig. 3.9(b); the easy-axes data are also plotted for comparison. Again, the high field resistance values for the  $40^\circ$  data are consistent with Eq. 2.1 and indicate that the magnetization is saturated

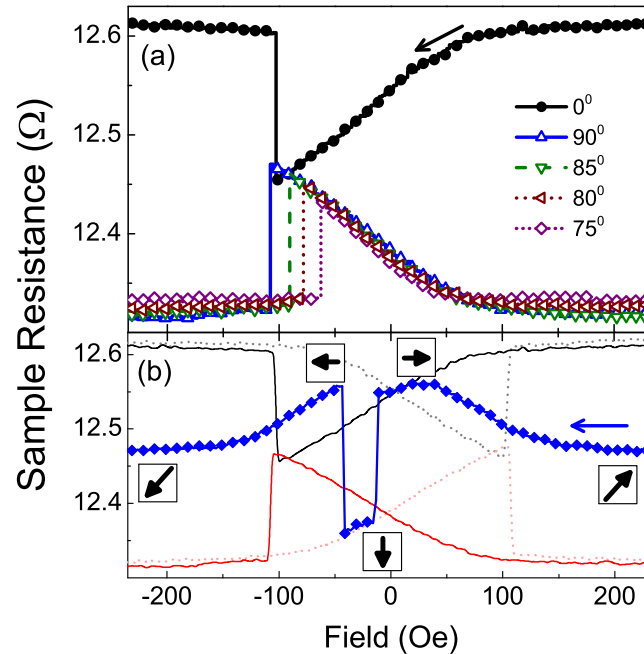


Figure 3.9: Resistance vs. applied field magnitude comparing the behavior for field directions (a) near the easy axis and (b) far from the easy axis for a 250 nm square dot. In (a) only one sweep direction is shown and a decrease in coercivity can be observed as the applied field moves away from  $90^\circ$ . In (b) data for an applied field at  $40^\circ$  (blue diamonds) can be compared with the easy-axes data (lines without symbols following the color convention in Fig. 3.7). The boxed symbols indicate the inferred magnetization directions for the  $40^\circ$  data.

along the field direction. As the field is swept from positive to negative fields however, the resistance is observed at times to track data from both the  $0^\circ$  and  $90^\circ$  loops. Assuming the magnetization adopts the same states as in the easy-axis loops at low fields, we postulate that the  $40^\circ$  data displays a rotation of the magnetization through two successive  $90^\circ$  rotations as indicated by the cartoons in the figure.

### 3.4.3 Diagonal Hysteresis Loops: Evidence of Magnetic Noise

The most intriguing applied field direction for measuring a hysteresis loop is along the diagonal of the dot. Details of this applied field direction will be discussed in Chapter 4 since the samples exhibit large amounts of magnetic noise at these applied field directions. In Fig. 3.10, we plot two successive sweeps of the field when the field is applied along the

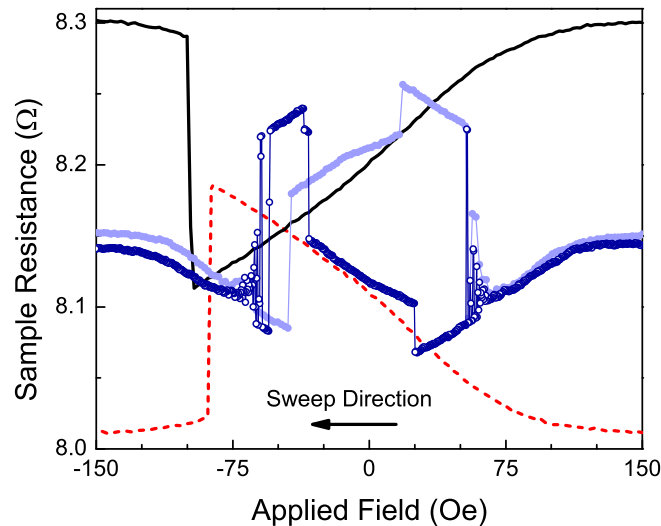


Figure 3.10: Resistance vs. applied field data for a 300 nm with applied field directions of  $0^\circ$  (black line),  $90^\circ$  (dashed red line), and  $45^\circ$  (blue lines with symbols). Two sets of data are shown at  $45^\circ$  taken consecutively under identical conditions. Both show evidence of magnetic noise around  $\pm 65$  Oe but exhibit different resistances at remanence suggesting that the system randomly chooses a ground state magnetization at  $0^\circ$  or  $90^\circ$ .

diagonal of the dot; the easy-axis data are again plotted for comparison. Fluctuations of the resistance occur around  $\pm 50$  Oe, which are associated with the magnetization thermally hopping between the low-energy magnetic states parallel to the dot edge and adjacent to the applied field direction. We also observe different resistance values between the two data runs at remanence, in the first case equal to the resistance for the  $0^\circ$  easy-axis loop and in the second case equal to the resistance for the  $90^\circ$  easy-axis loop. These field sweeps were taken under identical conditions and further repetition randomly yielded the two different resistance values at remanence. We interpret this behavior as the magnetization adopting one of the two different remanent states, which have the same energy, with equal probability.

### 3.5 Stoner-Wohlfarth Model

We explain the magnetic behavior of our dots through a simple model of the magnetization that also allows us to quantify the magnitude of configurational anisotropy energy barriers.

### 3.5.1 Model Description

To model the magnetization in our dots, we assume that the magnetization settles into a local minimum of the magnetic energy landscape and changes orientation only when this minimum moves or is destroyed. This model was first formulated by Stoner and Wohlfarth [75] for an ellipsoidal particle with two well-defined minima corresponding to the easy-axis directions of the magnetization. Based on the rotational hysteresis data presented above, it is apparent that our square samples exhibit a four-fold symmetry to their magnetic energy landscape, which is not unsurprising given their shape. For simplicity, we assume that the configurational anisotropy energy varies sinusoidally with the net magnetization direction and with a period of  $90^\circ$ . Then, the total magnetic energy at zero field is given by

$$E(\theta) = -\frac{E_A}{2} \cos(4\theta), \quad (3.1)$$

where  $\theta$  is the direction of the magnetization and  $E_A$  is the difference in configurational anisotropy between the low-energy state parallel to an edge of the square and the high-energy state oriented along the diagonal of the square. This model defines  $\theta$  so that it is consistent with our data and Eq. 2.1. The configurational anisotropy energy captures all of the details of the interplay between the magnetostatic and exchange energies.

To account for the presence of a magnetic field we incorporate the Zeeman energy into our equation for the total magnetic energy of our system which modifies Eq. 3.1 as follows:

$$E(\theta) = -\frac{E_A}{2} \cos(4\theta) - mH \cos(\theta - \theta_H), \quad (3.2)$$

where  $m$  is the magnetic moment of the dot, and  $H$  and  $\theta_H$  indicate the magnitude and direction of the applied magnetic field. Both the simulations and experiments indicate that the magnetization of the dots bends at small fields and thus  $m$  is itself a function of  $H$ . However, we will assume the internal magnetization state is independent of the applied field and therefore  $m$  is constant with a value equal to the saturation magnetization of the dot multiplied by its volume.

The shape of the energy surface described by Eq. 3.2 is plotted in Fig. 3.11 with an SEM image of a square dot provided for reference. The z-axis of this plot corresponds to the magnetic energy associated with a magnetization aligned in a given direction. In zero applied magnetic field, Fig. 3.11(a), there are four minima each corresponding to the four magnetization directions which lie perpendicular to one of the dot edges. The magnetic



field effectively tilts this energy surface in the direction of the field thereby lowering the energy of the magnetization in that direction.

To use our energy model to describe the magnetization in square dots, we assume the magnetization settles in the nearest energy minimum. For significantly large changes in applied field, the magnetization can be dislodged from its original local energy minimum and move to a new local energy minimum. This corresponds to the large jumps in resistance that we associate with the abrupt changes of the magnetization in our data.

This model of the magnetization assumes that the magnetization is highly damped, losing its kinetic energy immediately upon moving to a lower energy state. The physical mechanism of the energy dissipation mechanism is not considered here but would likely occur through coupling of magnons to the phonon bath of the system [76]. In this chapter, thermal energies are neglected.

### 3.5.2 Modelling the Rotational Hysteresis Data

From our energy model of the magnetization, we can directly account for the rotational hysteresis loops that we observe in our samples. For large magnetic fields, the magnetic energy surface will be highly tilted in the direction of the field resulting in a single minimum in the energy surface in that direction. As the field direction is rotated, the magnetization will simply follow the direction of the applied magnetic field, explaining the agreement of

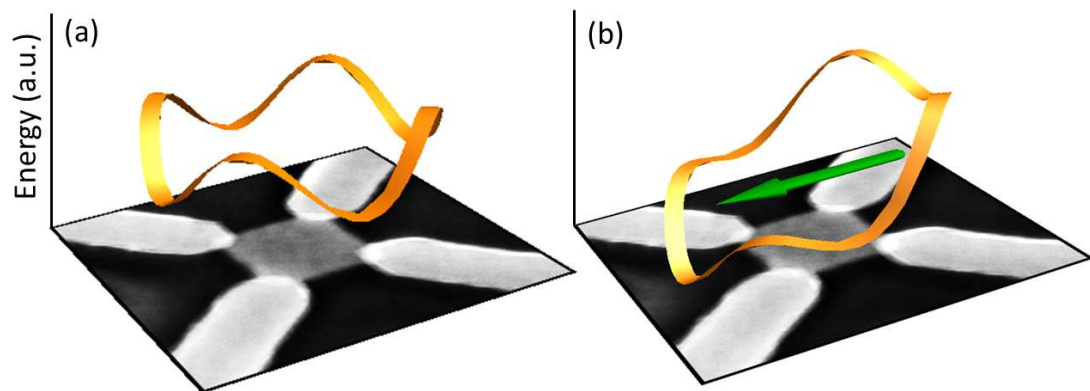


Figure 3.11: A cartoon of Eq. 3.2 where the total magnetic energy of the dot according to our model is plotted in yellow as a function of the magnetization direction for the cases where (a) there is no applied field and (b) and the applied field is oriented along the easy axis (green arrow). An SEM image of a typical dot is superimposed on the floor of the plot for reference.

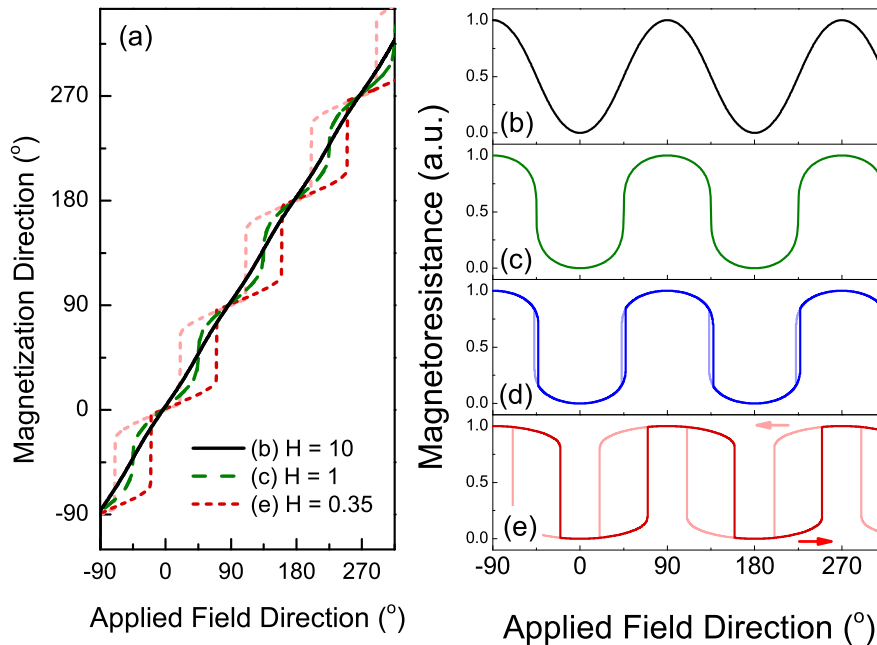


Figure 3.12: Simulated rotational hysteresis data using the model described in Sec. 3.5.1 with a dimensionless configurational anisotropy energy,  $E_A = 1/8$ , and varying the applied field direction for fixed field magnitudes. (a) The magnetization direction plotted as a function of applied field angle for the values of  $H$  indicated. Assuming a total unitless magnetoresistance of 1.0, the magnetoresistance vs. applied field direction is plotted for (b)  $H = 10$ , (c)  $H = 1.0$ , (d)  $H = 0.75$ , and (e)  $H = 0.35$  where the minimum field necessary to rotate the magnetization in these units is  $H = 0.25$ . The magnetization data corresponding to  $H = 0.75$  in (d) has been omitted from (a). Arrows in (e) denote rotation directions.

Fig. 3.1 with Eq. 2.1.

At smaller applied fields, the configurational anisotropy begins affect the magnetization. For example, suppose the magnetization is initially oriented at  $0^\circ$  and the applied field is also in this direction. In this orientation, a high resistance state is observed. As the field is rotated, a local energy minimum will remain near  $0^\circ$  due to the configurational anisotropy. Thus the magnetization will lag behind the applied field and the resistance will remain high. It is only when the field is rotated sufficiently far to destroy the original energy minima that the magnetization will rotate noticeably. In this case, the magnetization will settle in the new local minima, around  $90^\circ$  if the field was rotated in a positive direction.

By combining Eqs. 2.1 and 3.2 we can simulate rotational hysteresis loops based on

this model as shown in Fig. 3.12. In the large field case, the magnetization follows the magnetic field with no hysteresis. As the field is reduced there are jumps in resistance and hysteresis between the two rotation directions which agree well with our experimental data in Fig. 3.2.

To quantify the magnitude of the configurational anisotropy energy through rotational hysteresis, we determine the minimum applied field sufficient to destroy the energy minima in Eq. 3.2 and dislodge the magnetization. To understand this, we note that the first derivative of the total magnetic energy of the system with respect to the magnetization direction gives the torque,  $\tau_{eff}$ , applied to the magnetization at a given direction, that is

$$\frac{dE}{d\theta}(\theta) = \tau_{eff} = 2E_A \sin(4\theta) + mH \sin(\theta - \theta_H). \quad (3.3)$$

The first term is the torque due to the external field and the second term is the effective configurational anisotropy torque. For the magnetization to become depinned and rotate to a different direction, the torque created by the applied field must overcome the effective torque from the configurational anisotropy within the local minimum. The maximum effective torque from the configurational anisotropy occurs at odd multiples of  $45^\circ$  and has a magnitude of  $2E_A$ . Similarly, the maximum torque that the applied field can provide is  $mH$ . Thus, we immediately see that we can measure the configurational anisotropy energy magnitude using the data in Fig. 3.2(c) since

$$E_a = \frac{mH_{min}}{2}, \quad (3.4)$$

where  $H_{min}$  is the minimum field which exhibits a transition. The maximum torque is developed when the applied field is perpendicular to the magnetization. Thus, to dislodge the magnetization from a minimum at  $45^\circ$ , at the smallest fields the resistance change will be observed at field angles of  $135^\circ$  or  $-45^\circ$ , in general agreement with our measurements.

### 3.5.3 Modelling the Easy-Axis Hysteresis Data

The easy-axis hysteresis loops offer a second method of quantifying the magnitude of the configurational anisotropy. To explain the data in Fig. 3.5, we begin by considering a large applied magnetic field at  $0^\circ$  with the magnetization settled in the global minimum at  $0^\circ$ . As the field is reduced to zero the magnetization is fixed since the configurational anisotropy naturally encourages the magnetization to remain in the original orientation.

Even after applying a small negative magnetic field, the magnetization will remain at  $0^\circ$ . It is not until the energy surface is tilted sufficiently to destroy the minima at  $0^\circ$  that the magnetization will be dislodged from this minimum and rotate to the only available minimum, at  $180^\circ$ . This process repeats itself as the field is swept in the opposite direction, thus a hysteresis develops. The same behavior would be expected based on our model for an applied field at  $90^\circ$ . We note, however, that this model does not capture the slight decrease in the magnetic moment of dot due to the bending of the magnetization.

Quantifying the magnitude of the configurational anisotropy from the hysteresis data follows a similar procedure to that used in the rotational data. We again determine the condition where the local energy minimum is destroyed and the magnetization rotates to the opposite direction. The locations of the energy minima are easily extracted from Eq. 3.2 by setting the first derivative of this equation with respect to angle, Eq. 3.3, equal to zero. If the applied field direction is taken to be along the easy axis, that is any multiple of  $90^\circ$ , there will always be a local energy extremum in the applied field direction. In order to determine when this extremum changes from a minimum to a maximum, and the magnetization switches direction, we examine the second derivative of Eq. 3.2 with respect to the direction of the magnetization,

$$\frac{d^2 E}{d\theta^2}(\theta) = 8E_A \sin(4\theta) + mH \cos(\theta - \theta_H). \quad (3.5)$$

Setting the second derivative of the total energy also to zero for a magnetization direction along an easy axis yields a second method of determining the magnitude of the configurational anisotropy. Using the measured easy-axis coercivity,  $H_C$ , the configurational anisotropy can be calculated as

$$E_a = \frac{mH_{min}}{2}. \quad (3.6)$$

#### 3.5.4 Modelling Non-Easy-Axis Hysteresis Loops

We note also that our model correctly predicts the behavior observed in the hysteresis loops taken for applied fields away from the easy axes. As in the case of the easy-axes hysteresis loops, the large abrupt changes in resistance coincide with the magnetization moving to a different local energy minimum in the magnetic energy landscape as the Zeeman energy destroys the original local energy minimum. While analytical expressions for the fields at which these switching events occur are not possible, for arbitrary applied

field angles we can numerically calculate hysteresis loops based on Eq. 3.2 which we plot in Fig. 3.13. These calculated data show qualitatively similar features to the experimental data in Fig. 3.9. Suggestions for future research to make this work more quantitative are discussed in Sec. 5.2.2.

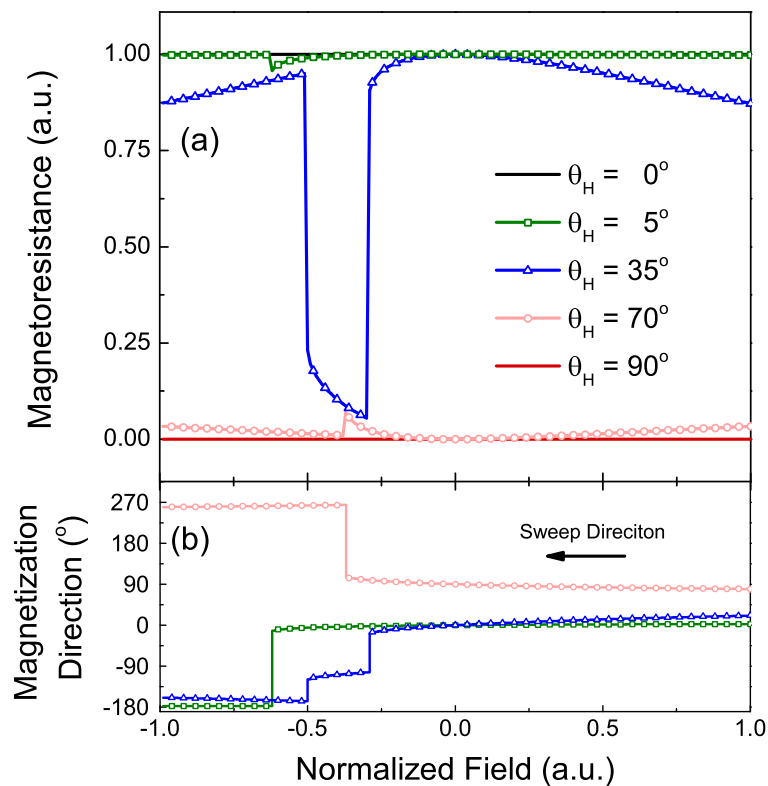


Figure 3.13: Simulations of the magnetization as a function of applied field for various applied field directions using the model discussed in Sec. 3.5.1. (a) The magnetoconductance is plotted as a function of the applied field magnitude in the normalized units where the configurational anisotropy energy has the fixed value of  $EA = 1/8$ . Since the bending effect of the magnetization is not incorporated into these simulations, the easy-axis data ( $0^\circ$  and  $90^\circ$ ) are featureless but the data for applied field directions of  $5^\circ$ ,  $35^\circ$ , and  $70^\circ$  can be compared to Fig. 3.9. (b) The direction of the magnetization is also plotted as a function of applied field for the non-easy-axis hysteresis loops.

### 3.6 Size Dependent Configurational Anisotropy

Based on our discussion above, it is straightforward to extract measurements of the configurational anisotropy from data such as that presented in Figs. 3.2(c) and 3.7 for a range of dot sizes. Both the easy-axis coercivity and the minimum field necessary to achieve rotational hysteresis are well-defined measurable quantities in our data. In Fig. 3.14 we plot the observed easy-axis coercivity and minimum rotational hysteresis fields respectively as a function of dot size. The measurement of the coercivity can be made for each easy axis and the rotational hysteresis measurement for each diagonal direction. Thus, each dot measured yields two values for each measurement technique. Rather than averaging these values, which is not justified a priori, we plot both values in each case.

To connect the data in Fig. 3.14 to the configurational anisotropy, the magnetic moment of the dot must be determined. For simplicity, we maintain our assumption of a single-domain magnetization and take  $m$  to be the product of the saturation magnetization and the dot volume. In Fig. 3.15, we plot the calculated configurational anisotropies using this assumption for the magnetic moment of the dot. The two measurement methods show

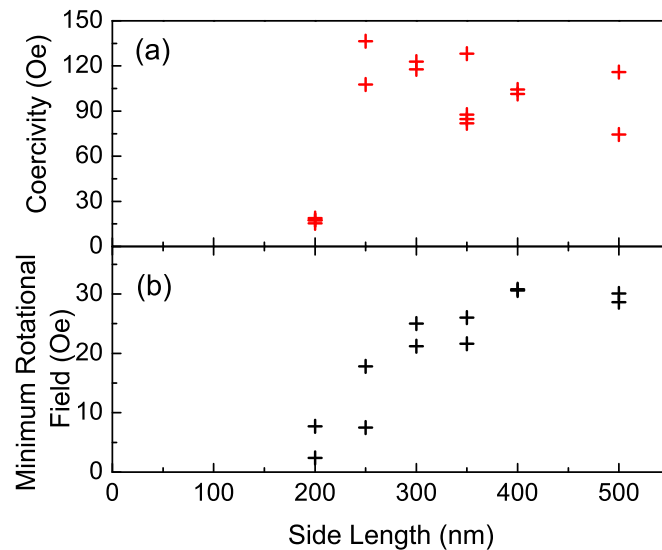


Figure 3.14: (a) Measured coercivity and (b) minimum field necessary to rotate the magnetization plotted as a function of dot side length for 10 nm thick dots. Each dot yields two data points per measurement since two easy axes and two diagonal directions can be measured. The precipitous decrease in coercivity for samples with a side length of 200 nm is likely a temperature effect such as is discussed in Sec. 3.7.2

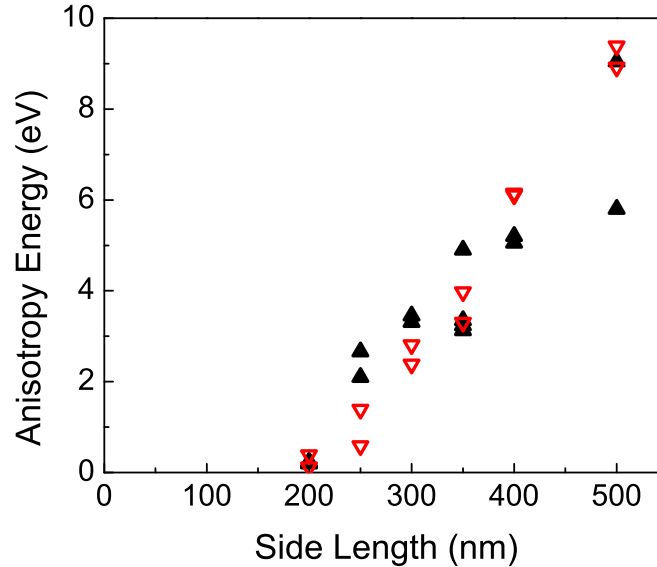


Figure 3.15: Measured configurational anisotropy energy barriers as a function of dot side length based on the dot coercivity (solid black symbols) and rotational hysteresis (red open symbols) data shown in Fig. 3.14. Reprinted, with permission, from Ref. [61]. Copyright 2013, AIP.

good agreement across the range of dot sizes measured. This agreement strongly supports our model since the measurement techniques probed the dot magnetization through independent methods and yielded the same measurement for the configurational anisotropy.

Additional striking features of the size dependence of the configurational anisotropy are its linear dependence on dot size and disappearance at a finite dot size of around 150 nm. The linear dependence on dot size is not unexpected since the dot side length also parameterizes the surface area to volume ratio of the sample. The magnetostatic energy is strongly influenced by the dot geometry while the exchange energy is not. Thus, as the sample geometry changes, one would expect the configurational anisotropy to also change. Similarly, at some finite dot size, the exchange energy will begin to strongly dominate over the magnetostatic energy in favor of a completely single domain dot. Thus, it is not unexpected that the configurational anisotropy would disappear near this length scale.

In addition to these qualitative physical arguments, our observations confirm the previous measurements of configurational anisotropy on arrays of dots. Our dots, give a configurational anisotropy twice the value of those previously measured which are a factor

of 2 thicker [56]. However, the sign of our configurational anisotropy, that is the preference for magnetization to point parallel to an edge versus the diagonal, differs from the previous measurements [56]. The source of this sign change is still unknown but may be due to a difference in the relative strengths of the magnetostatic and exchange energies for different materials (Supermalloy,  $\text{Ni}_{80}\text{Fe}_{14}\text{Mo}_5$ , was used in this previous study). The corners of the dot also likely play a significant role in determining the lowest energy state; differences in the sharpness of the corners are likely due to the difference in deposition techniques between the two results. Simulations produced by this same group also found the energy barrier to disappear at a finite side length [52]. Their simulation results plotted in Fig. 1.4, in contrast with their experimental data, supports our conclusion that the configurational anisotropy does not disappear but changes to favor a diagonal magnetization below a certain side length. Since the properties of this magnetic phase change are clearly still not well understood we propose further experimental investigations into this topic in Chapter 5.

## 3.7 Limits of the Configurational Anisotropy Measurements

While our measurements of the configurational anisotropy confirm the predictions of our model and can be used to estimate of the magnitude of the configurational anisotropy, there are several limitations which introduce uncertainty.

### 3.7.1 Bending of the Magnetization

The first major limit to the accuracy of our quantification of the configurational anisotropy is the lack of a true single domain character of the magnetization. Since simulations and experiment both show that the magnetization adopts a bent magnetic state, the magnetization clearly is not a true single domain. As a result, in Eq. 3.2, we know that the magnetic moment that appears in this equation cannot be simply equal to the product of the dot volume and the saturation magnetization. Simulations indicate that the net magnetization of the dot is around 80% of saturation near zero field (where the rotational measurements are made) and drops to almost 60% near the coercivity. Inputting this into our calculations for the configurational anisotropy would lower our estimates of the configurational anisotropy by the same amounts. Without accounting for the field dependence of the magnetization, this source of error over estimates the strength of the



Zeeman energy. While these corrections could be made, it is unclear how the experimental AMR data relates to the change in magnetic moment and thus the corrections would rely on data taken from simulations. This source of uncertainty is sample size dependent and it appears to have a stronger effect on the larger samples where the bending of the magnetization is greatest.

### 3.7.2 Temperature Effects

The second major limit to the accuracy of our measurement of the configurational anisotropy arises from the fact that our measurements are made at room temperature. The room temperature thermal energy is approximately 0.025 eV and therefore the associated thermal fluctuations may dislodge the magnetization from any minimum which has a depth several times this size. We will discuss this effect in much greater depth in Chapter 4 but for now it is sufficient to note that in the case of a 200 nm dot, the energy barriers between low energy magnetic states at zero field are only 40 to 80 times the size of thermal energies.

To see how thermal energies limit our measurements of the configurational anisotropy, consider Fig. 3.16 which shows easy-axis hysteresis loops taken for a 250 nm dot at various

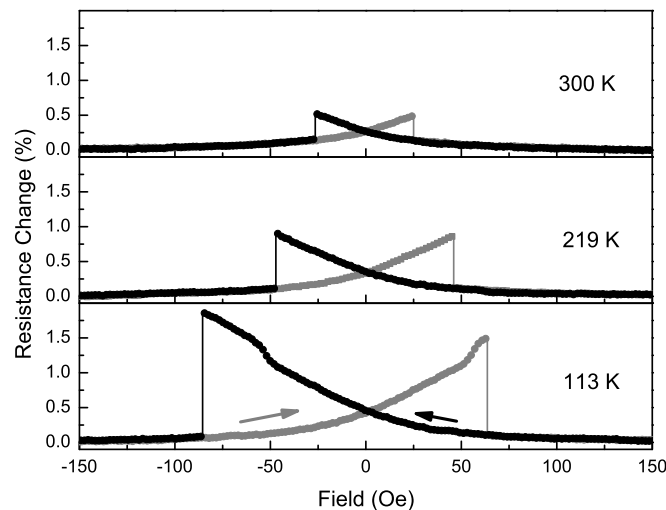


Figure 3.16: Measurements of the magnetoresistance change as a function of applied field for a field applied at  $90^\circ$  taken at three different temperatures indicated in the figure where the arrows indicate the sweep direction. Data is taken on a 250 nm dot. The normalized magnetoresistance is plotted since the sample resistance is also temperature dependent.

temperatures. The coercivities of these loops clearly increase as the temperature decreases. This can be understood as an indication that the magnetization switches not when the original local minimum disappears but when its depth becomes comparable to thermal energies. Thus our measurement of the coercivity at room temperature underestimates the true magnetic field needed to destroy the original energy minima. In this case, the thermal fluctuations cause the magnitude of the configurational anisotropy to be underestimated. Thermal energies also underestimate the configurational anisotropy calculated from the rotational hysteresis data; at room temperature a smaller field is required to achieve rotation of the magnetization since thermal energies assist in depinning the magnetization.

The temperature effect is size dependent, like the uncertainty due to the bending of the magnetization. In this case however, the smallest samples, which have the smallest energy barriers, are most strongly affected. Since the magnitude of this uncertainty is related to thermal activation of the magnetization over a small energy barrier, it depends on the measurement time. Longer measurement times increase the probability that thermal energies will switch the magnetization as discussed Sec. 4.2.3.

### 3.7.3 Sinusoidal Anisotropy

The assumptions made about the configurational anisotropy in our model and Eq. 3.2 also limit our analysis. For simplicity we assumed that the configurational anisotropy varies sinusoidally with the direction of the magnetization. The actual functional form however is unknown although we do know it has a four-fold symmetry based on our sample shape. While other functional forms would likely maintain the same relationship between switching fields and the calculated configurational anisotropy in Eqs. 3.4 and 3.6, the leading numerical coefficients would change.

### 3.7.4 Fabrication Imperfections

While the above sources of uncertainty all represent systematic errors, the imperfections in nanofabrication introduce a large source of random error. The variations introduced in the fabrication process were discussed above and shown in Fig. 3.4. Fluctuations in the sample dimensions as well as significant edge roughness are apparent in these images. These sample variations naturally lead to variation in our experimental measurements and the measurements of the configurational anisotropy as seen by the variation of the data in Fig. 3.15. While the data do display a consistent trend, there is noise in the data and

we attribute this primarily to variations between the samples.

## 3.8 Comparison to Micromagnetic Simulations

Much of the observed magnetic behavior of our square dot samples is reproduced in micromagnetic simulations. In addition to explaining the change in resistance in the hysteresis loops through a bending of the magnetization, the simulations confirm our model of the magnetization.

### 3.8.1 Easy-Axis Hysteresis

Simulations of hysteresis loops for our dots confirm that the magnetization switches direction in a single well-defined switching event. This was discussed above and demonstrated in Fig. 3.6. The coercivities obtained through the simulations were similar to those observed in experiment. In most cases the simulation produced a larger coercivity. For example in Fig. 3.6, a 200 nm square exhibits a coercivity of 250 Oe while the measured coercivity

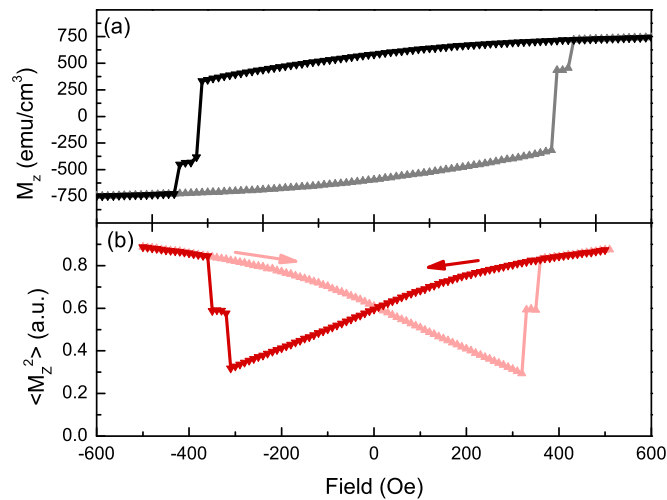


Figure 3.17: Simulation of an easy-axis hysteresis loop for a 200 nm dot where the (a) magnetization and (b) the the average of the square of the magnetization over the simulation cells,  $\langle M_z^2 \rangle$ , parallel to the applied field direction are plotted as a function of applied field. Since  $\langle M_z^2 \rangle$  is proportional to the AMR response, the data in (b) directly compared to the experimental data. The intermediate state observed around  $\pm 330$  Oe is a vortex state, which is likely unstable over longer simulation times. The simulations were conducted by Randall Victora and Chad Weigelt at 300 K and each data point was simulated for 1 ns.

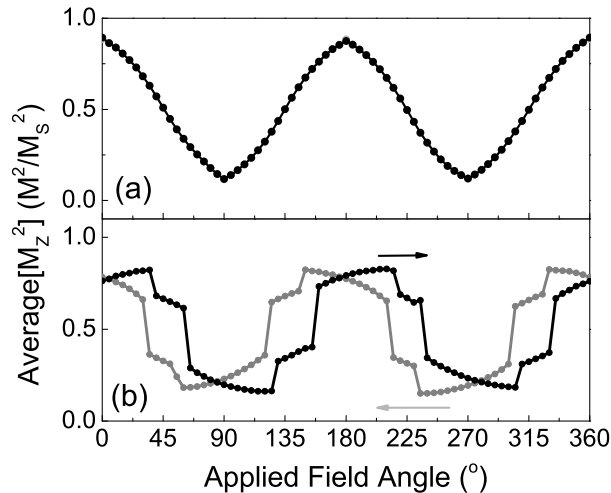


Figure 3.18: Simulation of rotational hysteresis loops of a 200 nm dot at applied fields of (a) 500 Oe and (b) 175 Oe. As in Fig. 3.17(b),  $\langle M_z^2 \rangle$  is plotted and can be directly compared to the experimental AMR data. The simulations were conducted by Randall Victora and Chad Weigelt at 300 K and each data point was simulated for 10 ns. Reprinted, with permission, from Ref. [61]. Copyright 2013, AIP.

for a dot of this size was only 20-40 Oe. The fabrication imperfections such as rounded dot corners may lower the configurational anisotropy energy barriers and reduce the coercivity in the experimental data. At the same time, the computational power required for the simulations limited the simulation time to microseconds. Since these time scales are orders of magnitude shorter than the experimental measurement timescales, thermal fluctuations will have a less substantial effect on the simulations than on the experimental data.

Simulations by Randall Victora and Chad Weigelt suggest the switching mechanism in the easy-axis loops is not by coherent rotation but by the formation of a metastable vortex state which propagates across the dot allowing the magnetization to switch. As shown in Fig. 3.17, an intermediate state similar to that seen in the experimental data in Fig. 3.8 appears after the field is swept past remanence. Since the simulations were conducted using a very short simulation time this vortex state may not be physically stable and the large coercivity may be unphysical as well. The details of this switching mechanism disagree with our simplified model of the magnetization but the specifics of the switching process do not alter our identification of a configurational anisotropy in square dots.

### 3.8.2 Rotational Hysteresis

Simulations of rotational hysteresis loops were also conducted by Victora and Weigelt which showed qualitative agreement with our experiments. Large and small field rotational hysteresis loops are shown in Fig. 3.18. In this figure we plot the mean square of the magnetization parallel to an edge as this is the quantity measured by the AMR (it is proportional to the square of the dot product between the current and the magnetization).

The simulations verify that at these fields the magnetization is saturated and follows the applied field for large fields. The simulations also reproduce rotational hysteresis at lower fields with well-defined abrupt switching in the magnetization. However additional structure is also present in the curves and larger fields are required to achieve rotation in the simulation than in the experiments. Much of the finer structure appears to arise from pinning of the magnetization at the corners of the dot which are more precise or square in the simulation than in the experiment (additional structure in the rotational data is discussed in Sec. 5.2.2). Figure 3.19 shows the magnetic configuration at several points in Fig. 3.18 supporting this conclusion. The magnetization configurations also appear to be primarily ‘S’ shaped magnetization states instead of the ‘U’ shaped states plotted in Fig. 3.12 and predicted by Cowburn et al [54]. Finally, we note that preliminary simulations of rotational hysteresis at zero temperature differed significantly from the room temperature data suggesting thermal fluctuations allow for switching mechanisms not accessible at zero temperature.

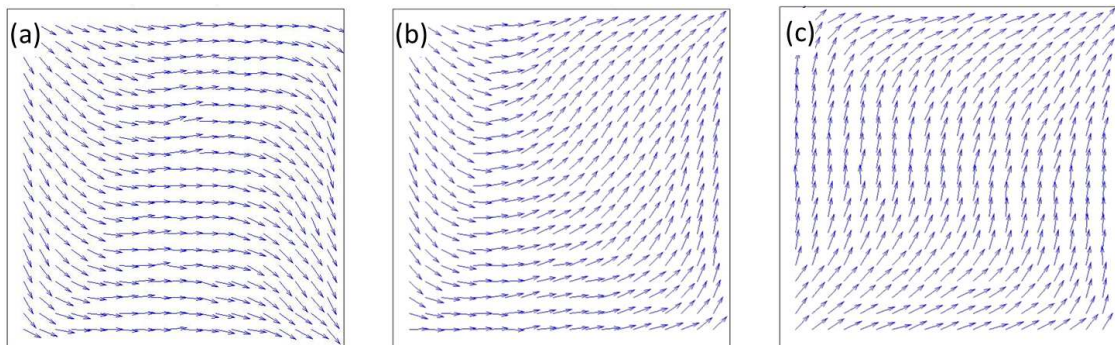


Figure 3.19: The in-plane magnetization vectors for each simulation cell corresponding to the data in Fig. 3.18(b) at applied field angles of (a)  $0^\circ$ , (b)  $60^\circ$ , and (c)  $65^\circ$ . Data taken from simulations by Randall Victora and Chad Weigelt.

## Chapter 4

# Observation and Explanation of Telegraph Noise

Thermally driven magnetic noise appears in our square dot samples as a result of the magnetic energy landscape discussed in Chapter 3. In this chapter, we show that an applied field can lower the energy barriers in this system and allow thermal fluctuations to drive the magnetization over the barrier, randomly switching between low energy orientations.

### 4.1 Signatures of the Telegraph Noise

#### 4.1.1 Noise in Hysteresis Loops at the Dot Diagonal

The hysteresis loops of the dot resistance taken for applied fields along the dot diagonal give us an initial picture of the magnetic noise in our system. In Fig. 3.10, we presented the resistance of the dot as a function of applied field along the dot diagonal. Magnetic noise appears at both positive and negative fields with a magnitude of  $\sim 60$  Oe. The amplitude of the resistance fluctuations is larger at smaller applied fields, but they disappear at the smallest fields. Repeated data runs demonstrate that the resistance at remanence randomly assumes one of two values consistent with the remanent resistance observed in easy-axis hysteresis loops (applied fields of  $0^\circ$  or  $90^\circ$ ).

To understand these resistance fluctuations, recall the model of the magnetic energy landscape in our square dots. This energy landscape is plotted versus magnetization direction in Fig. 4.1 for several applied field values at  $45^\circ$ . At large applied field values

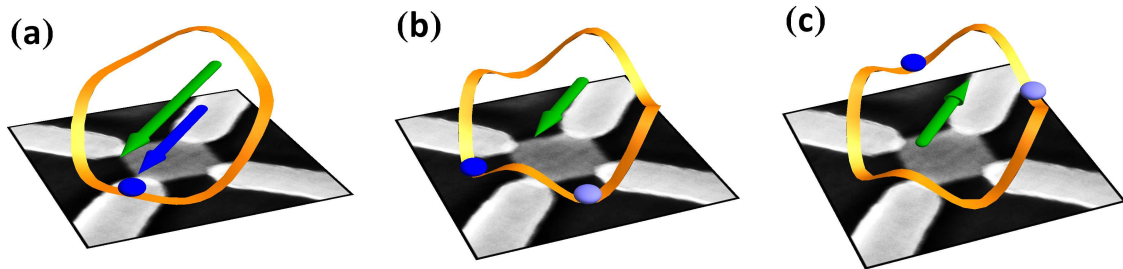


Figure 4.1: Energy diagrams for an applied field along the dot diagonal (a) at a large field where the magnetization is saturated along the diagonal, (b) at a smaller field where two local energy minima exist separated by a small energy barrier, and (c) at a negative field where the low energy states exist in the opposite direction. The green arrow indicates the applied field direction while the blue arrow and balls indicate the low energy magnetization orientations. In (b) and (c) two possible magnetization directions are indicated.

a single global minimum exists at  $45^\circ$  which causes the magnetization to align to the dot diagonal at large fields. Thus, the observed resistance above 100 Oe in Fig. 3.10 is half between the  $0^\circ$  and  $90^\circ$  cases in agreement with Eq. 2.1. At smaller positive fields, the configurational anisotropy begins to emerge as a local maximum at  $45^\circ$  with minima on either side. As the field is further reduced, both the height of the energy barrier and the separation between the minima grow leading to larger changes in resistance. For sufficiently small fields, the probability of switching becomes exponentially low and below 50 Oe, no switching is observed since the magnetization remains pinned in one of the two possible energy minima. Finally, plotting the energy contour for a similar negative field, we note that a local energy minimum appears on either side of a local maximum at  $-135^\circ$ , explaining the fluctuations we observe at negative fields.

#### 4.1.2 Observed Noise PSDs: Lorentzian Spectra

To quantify the properties of this magnetic noise we examine the noise power spectra at field values where the noise is observed. In Fig. 4.2, we plot the PSD observed at several different applied fields. For reference, we also plot the measured PSD observed at large applied fields to indicate the non-magnetic background noise. This background is dominated by the Johnson-Nyquist noise for the voltage leads of the sample ( $\sim 400 \Omega$ )

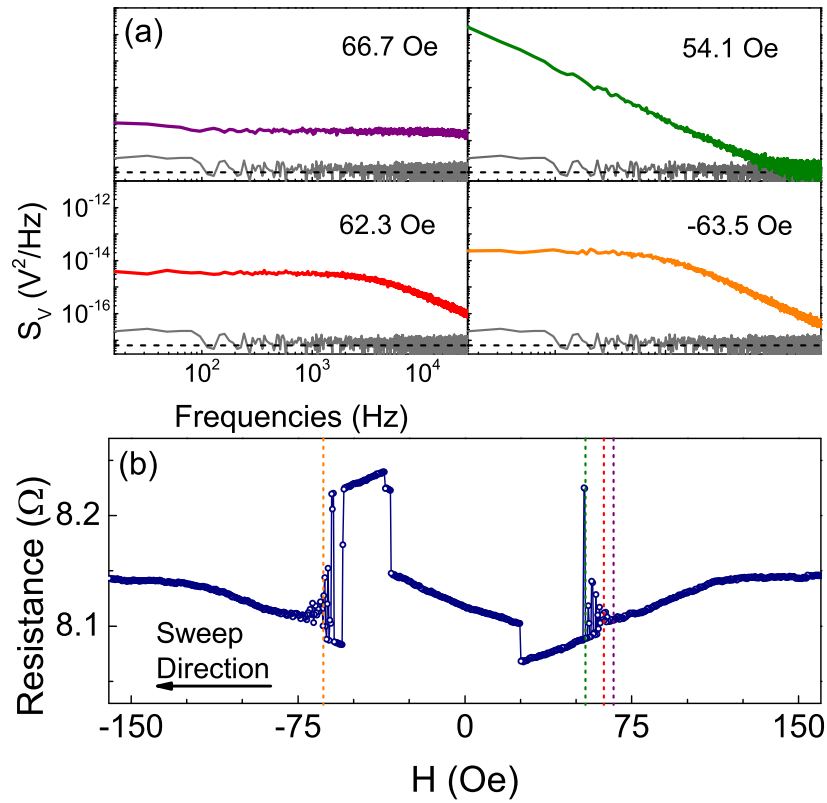


Figure 4.2: Data for a 300 nm square dot where (a) the measured PSD is plotted on a logarithmic scale as a function of frequency for four different applied fields at  $45^\circ$  with the field magnitudes indicated. The non-magnetic background noise measured at 215 Oe (gray line) and predicted Johnson-Nyquist noise for a  $400 \Omega$  resistor (dashed line) are provided for reference. (b) Data for the resistance vs. applied field has been reproduced from Fig. 3.10 and vertical lines have been added corresponding to the field values of the data taken in (a).

[18, 19]. At large fields, the PSD simply consists of an elevated frequency independent white-noise signal can be identified as the low frequency components of a telegraph noise signal with a very high switching frequency. As the field is reduced, the white-noise component of the RTN signal increases and a roll-off to a high frequency  $1/f^2$  spectrum appears. As shown in Sec. 4.1.4, this spectral shape fits well to the Lorentzian spectra associated with telegraph noise, Eq. 1.2. At even smaller fields, the white noise spectra falls below our measurement bandwidth and only the  $1/f^2$  spectrum remains, disappearing below the non-magnetic background noise at high frequency. Similar PSDs are observed at corresponding negative fields. Within the accessible frequency range of 1 Hz to 100



kHz in the measurement setup, the PSD of the magnetic noise observed in the dots was entirely Lorentzian with the exception of some unexpected magnetic  $1/f$  noise observed at very large fields, which is discussed further in Sec. 5.2.3.

### 4.1.3 Time Dependence of the Resistance at a Fixed Field

The Lorentzian power spectra originate from a two state, random telegraph signal in the magnetization of the dot as a function of time. In Fig. 4.3, the resistance is plotted as a function of time for the same sample as in Fig. 4.2. In each case, the resistance switches abruptly between two different values after random amounts of time. Careful attention should be paid to the time scales on these plots as the characteristic switching time is observed to change by several orders of magnitude as the field is varied. Comparing the measured resistance states to the resistance values in the easy-axis hysteresis loops confirms

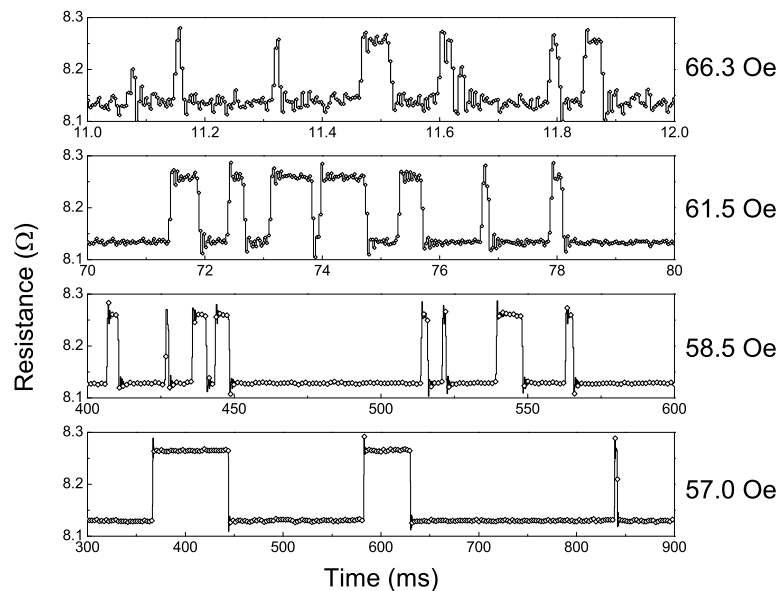


Figure 4.3: Measured resistance plotted as a function of time for applied fields along the dot diagonal (magnitude indicated next to each plot). Data was taken for the same dot as in Fig. 4.2 demonstrating that the Lorentzian PSDs arise from RTN. Note the difference in time scale on the x-axis for each data set since the telegraph frequency varies by nearly 3 orders of magnitude between the top and bottom panel. The overshoot in the data just after a transition, especially obvious in the bottom plot, is not physical but an aliasing artifacts, known as a Gibbs phenomenon [77], introduced by the limited bandwidth of the spectrum analyzer.

that the two resistance states are associated with the magnetization switching between orientations parallel to one of the dot edges. The PSD of a RTN signal is Lorentzian; thus observations of telegraph noise explain the observed frequency dependence of the magnetic noise.

#### 4.1.4 Telegraph Frequency and Fitting the Lorentzian

The switching frequency of the magnetization can be extracted directly by fitting the power spectra of the telegraph noise. This simplifies the analysis by avoiding the complex numerical analysis routines needed to extract the telegraph lifetimes from the time domain data [78]. Since Eq. 1.2 given in Sec. 1.2.3 is parameterized for a telegraph signal with an arbitrary ratio between the two state lifetimes, the values of each telegraph frequency cannot be extracted individually from the PSD without precise knowledge of  $\Delta V$ . However, if the two telegraph states have equal lifetimes, Eq. 1.2 can be simplified to

$$S_V(f) = \Delta V^2 \frac{2f_0}{(2f_0)^2 + (2\pi f)^2}, \quad (4.1)$$

where we have set  $f_1$  and  $f_2$  equal to the same characteristic switching frequency  $f_0$ . We emphasize that  $f_0$  is defined as the reciprocal of the telegraph state lifetime. Equation 4.1 then allows us to directly extract the switching frequencies of the magnetization from our measured PSD without a precise measurement of  $\Delta V$ . Thus, in making our measurements we first ensured that the field was correctly aligned to the local maximum in the configurational anisotropy so that the lifetimes of the two telegraph states were equal. This was accomplished by maximizing the measured low frequency noise (below  $f_0$ ) or by examining the time spectra as discussed in Sec. 4.2.7.

## 4.2 Tuning and Quantifying the Magnetic Noise

Using the measured telegraph frequencies, we can quantitatively show that our model predicts the observed magnetic fluctuations. In particular, the telegraph frequency is highly tunable via three experimentally controlled parameters: the applied field magnitude, the applied field direction, and temperature.

### 4.2.1 Field Dependence of the Telegraph Frequency

The applied field magnitude sets the rate of magnetic switching by adjusting the energy barrier height encountered by the magnetization. In Fig. 4.4, we plot the calculated switching frequencies as a function of applied field. The frequency data appear on a logarithmic scale since the switching frequencies vary across the five decades of frequency bandwidth available in our measurement setup within a small variation of applied field. As shown in this figure, our data also verifies that the switching frequency is symmetric in applied field with the same field dependence observed at positive and negative fields. The exponential dependence of the switching frequency on field reflects the fact that the magnetic noise is thermally activated and follows the Arrhenius law behavior discussed below.

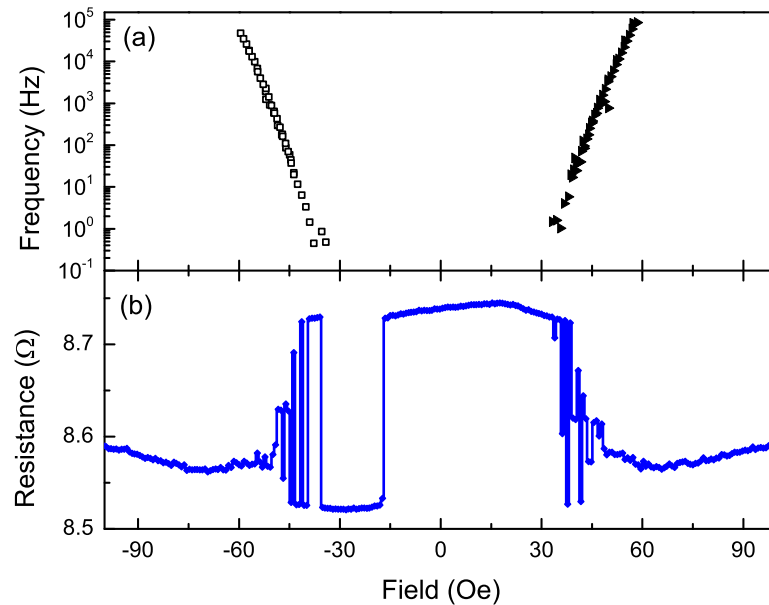


Figure 4.4: The (a) measured random telegraph frequencies and (b) sample resistance as a function of field applied at  $45^\circ$  for a 200 nm square dot. Telegraph frequencies for positive (solid triangles) and negative (open squares) show similar field dependencies and appear at the field values at which telegraph noise is observed in the resistance data. Note the logarithmic y-axis scale in (a). These data were measured at room temperature.

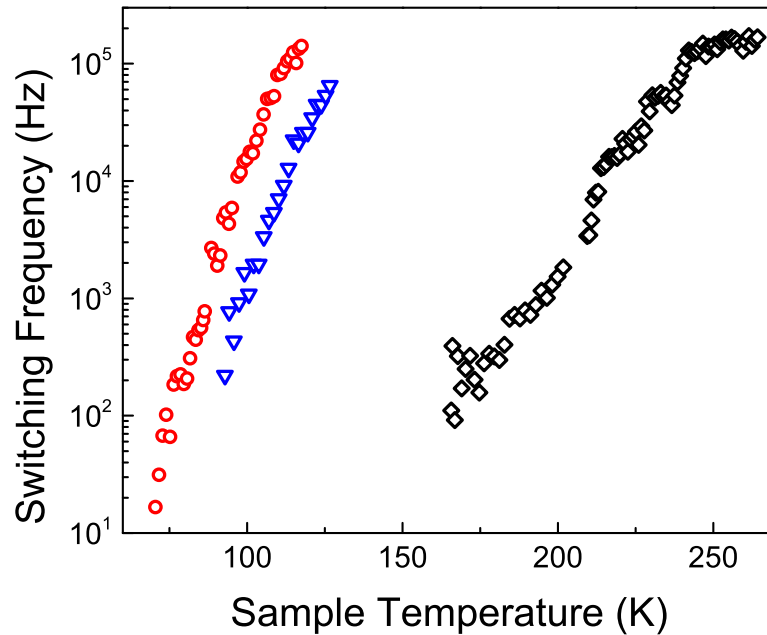


Figure 4.5: Switching frequencies plotted on a logarithmic scale as a function of temperature measured in a 200 nm square dot at applied fields along the dot diagonal of 83.5 Oe (red circles), 78.3 Oe (blue triangles), and 53.7 Oe (black diamonds).

#### 4.2.2 Temperature Dependence of the Telegraph Frequency

Just as the applied field magnitude tunes the energy barrier separating low energy states, the temperature adjusts the magnitude of thermal energy available to cause the magnetization to hop between states. By measuring the telegraph frequencies at fixed applied fields where the telegraph noise is observed, we can measure the effect of temperature on switching frequency as shown in Fig. 4.5. As in the applied field case, the switching frequencies are plotted on a logarithmic scale for several applied magnetic field values since a variation in the temperature by tens of degrees Kelvin results in telegraph frequencies that span our measurement bandwidth. The exponential dependence of the switching frequency on temperature confirms that the magnetic noise in our samples originates from thermal energies.

#### 4.2.3 Arrhenius Law and the Attempt Frequency

The thermally activated magnetic noise in our samples can be explained by an Arrhenius law which takes into account both the temperature and energy barrier height dependence

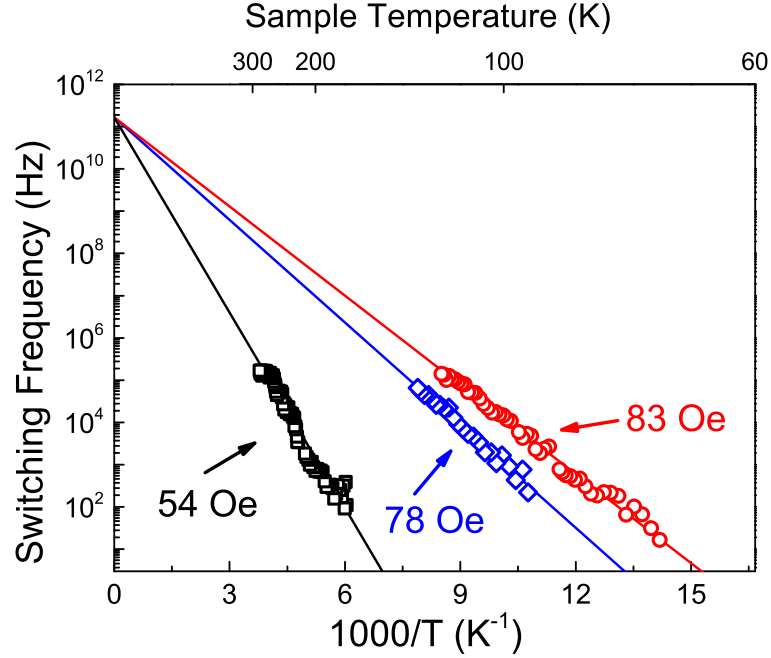


Figure 4.6: The same data shown in Fig. 4.5 plotted with an inverse temperature scale on the horizontal axis demonstrating that the telegraph noise obeys the Arrhenius law discussed in the text.

of the switching frequency. Originally formulated by Neel [57] and Brown [58], the expected Arrhenius law dependence of the switching frequency  $f_0$  is given by

$$f_0 = f_A \exp\left(-\frac{E_B}{k_B T}\right), \quad (4.2)$$

where  $f_A$  is the attempt frequency,  $E_B$  is the energy barrier height,  $T$  is the temperature, and  $k_B$  is the Boltzmann constant. This equation can be intuitively understood from the perspective of a particle trapped in a potential energy minimum. The attempt frequency represents the intrinsic frequency of the energy minimum that determines the rate at which the particle attempts to escape and the Boltzmann factor represents the probability of escape on a given attempt.

To verify the Arrhenius law behavior of the dynamics exhibited by our samples, we re-plot the data in Fig. 4.5 on an Arrhenius plot in Fig. 4.6 so that Eq. 4.3 appears as a straight line:

$$\ln(f_0) = \ln(f_A) - \frac{E_B}{k_B} \times \frac{1}{T}, \quad (4.3)$$

where the slope indicates the height of the energy barrier divided by the Boltzmann constant and the attempt frequency can be read-off as the y-intercept. Fitting the data to Eq. 4.3 to a common attempt frequency yields a value of about 170 GHz.

#### 4.2.4 Ferromagnetic Resonance Approximation

While the attempt frequency measured for our data agrees for the several applied magnetic field values, its value is difficult to explain theoretically based on our model. A range of attempt frequencies have been reported (0.2 to 46 GHz) [30, 31, 79–81], but, in general, magnetic systems with deeper magnetic energy minima exhibit higher attempt frequencies while magnetically soft materials tend to have lower attempt frequencies.

Since the attempt frequency corresponds to a natural frequency of the magnetic system, the ferromagnetic resonance (FMR) frequency may estimate the attempt frequency [58]. Following the method outlined in Kittel’s *Introduction to Solid State Physics* [82], an FMR frequency can be calculated for our energy barrier model (Eq. 3.2) as derived in Appendix D. This calculation assumes an out-of-plane shape anisotropy for an infinite thin film. Based on the data Fig. 3.15, the configurational anisotropy energy for a 200 nm square dot is approximately 1 eV. Using Eq. D.3, the effective field produced by the configurational anisotropy is  $H_{eff} = 8E_A/M_sV = 40$  Oe. Equation D.10 then predicts an FMR frequency for the square dot (without an externally applied field) of  $\sim 1$  GHz. Since the FMR frequency is approximately proportional to the relevant magnetic fields in the problem, incorporating the field applied along the diagonal of the dots during the experiments ( $\sim 50$  Oe) would not significantly alter this prediction.

The discrepancy between our calculated FMR frequency and the 170 GHz attempt frequency measured in our experiments is not understood. Some further experiments to study the attempt frequency are outlined in Sec. 5.2.5. Note also that only limited data was available in our experiments and that the value of 170 GHz is based on measurements on one sample (two additional samples were measured and both yielded anomalously high attempt frequencies: 3.5 THz for a 300 nm dot and 14 THz for a 250 nm dot).

#### 4.2.5 Field Dependence of the Energy Barrier

Since the RTN in our samples follows the Arrhenius behavior as indicated in Fig. 4.6, the field dependent energy barrier can be determined by inverting Eq. 4.3. Summarizing this process, we measure the applied field dependence of telegraph frequency as in Fig. 4.4.

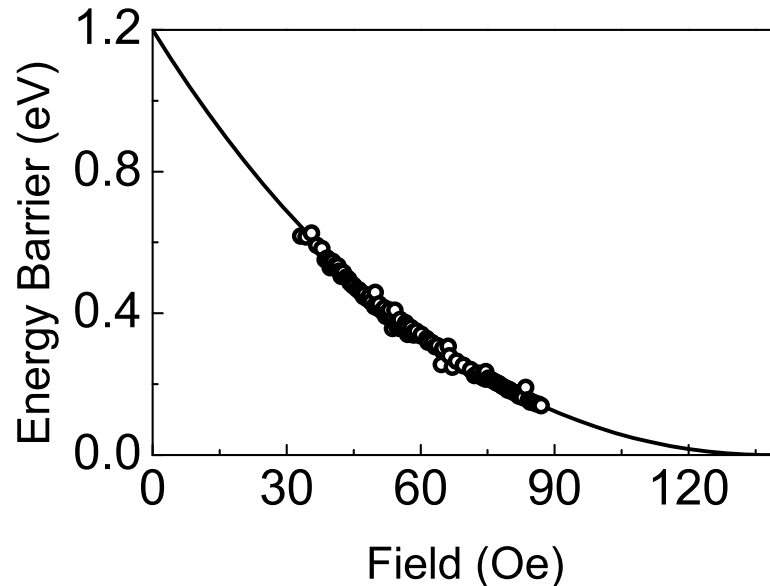


Figure 4.7: The energy barriers calculated based on the measured telegraph frequencies plotted as a function of applied field for a 200 nm square dot (symbols) and the prediction (line) numerically calculated based on Eq. 3.2. The y-intercept corresponds to the configurational anisotropy energy in this dot.

Taking data at multiple temperatures expands the range of fields exhibiting noise within our measurement bandwidth. We then calculate the field dependence of the energy barriers in our sample using Eq. 4.3 assuming an attempt frequency of 170 GHz. The energy barriers calculated from our data as a function of applied field are plotted in Fig. 4.7. The energy barrier increases with decreasing applied field as expected.

#### 4.2.6 Comparison to the Stoner-Wohlfarth Model

To tie our observations of the temperature and field dependence of the observed noise back to our model of the dot magnetization we can compare our calculated energy barrier heights with those predicted by our model. The height of the energy barrier predicted by our model can be calculated by determining the energy difference between the local maximum of Eq. 3.2 at  $45^\circ$  and the local minima on either side. Since the location of the local minima cannot be computed analytically from Eq. 3.3, we computed the height of the energy barriers numerically using a Mathematica worksheet.

To compare our calculated energy barriers from our model to our experimental data

we fit our computed barriers to the measured data. The dimensionless calculated barrier heights can be scaled for a given dot through two parameters. The field dependence is determined by fixing the magnitude of the Zeeman energy while the magnitude of the configurational anisotropy scales the energy barrier heights. If the magnetic moment of the dot is approximated as the product of the dot volume and the saturation magnetization, this fitting procedure reduces to a single fitting parameter. In Fig. 4.7, the calculated energy barriers from our model are plotted where the Zeeman energy and configurational anisotropy have been adjusted to fit the data. The functional form predicted by our model shows remarkable agreement with our measurements of the field dependence of the energy barrier.

The fit of our model provides a third method of measuring the configurational anisotropy energy barriers in our samples which can be compared with the results from the other two methods discussed in Sec. 3.6. The energy barrier extracted from the data in Fig. 4.7 can be read from the graph as the y-intercept. The magnitude of 1.2 eV agrees well with a barrier height of about 1 eV measured using the other two techniques described in Chapter 3. By determining the field dependence of the energy barrier, this measurement avoids the systematic errors introduced by temperature into the other two measurements. The error introduced by the uncertainty in the attempt frequency is proportional to the logarithm of the uncertainty in the attempt frequency and to the temperature. A true attempt frequency of 10 GHz, instead of the measured value of 170 GHz, would introduce an error of about 0.07 eV at room temperature.

#### 4.2.7 Angular Dependence of the Telegraph Noise

While temperature and the applied field magnitude offer directly quantifiable methods of tuning the rate of the telegraph noise, they do not adjust the relative lifetimes of the two magnetic states. In square dots this is accomplished by varying the applied field direction away from the configurational anisotropy maximum as demonstrated in Fig. 4.8. As the cartoon energy surfaces in this figure indicate, when the applied field angle is varied away from the dot diagonal, the minimum nearest in angle to the applied field direction is lowered while the other minimum is raised. Since the energy barrier which enters into Eq. 4.3 is determined by the difference between the starting state energy and the local energy maximum, the rate will be different for the magnetization to escape the two different local minima. The data in Fig. 4.8 provides qualitative evidence supporting



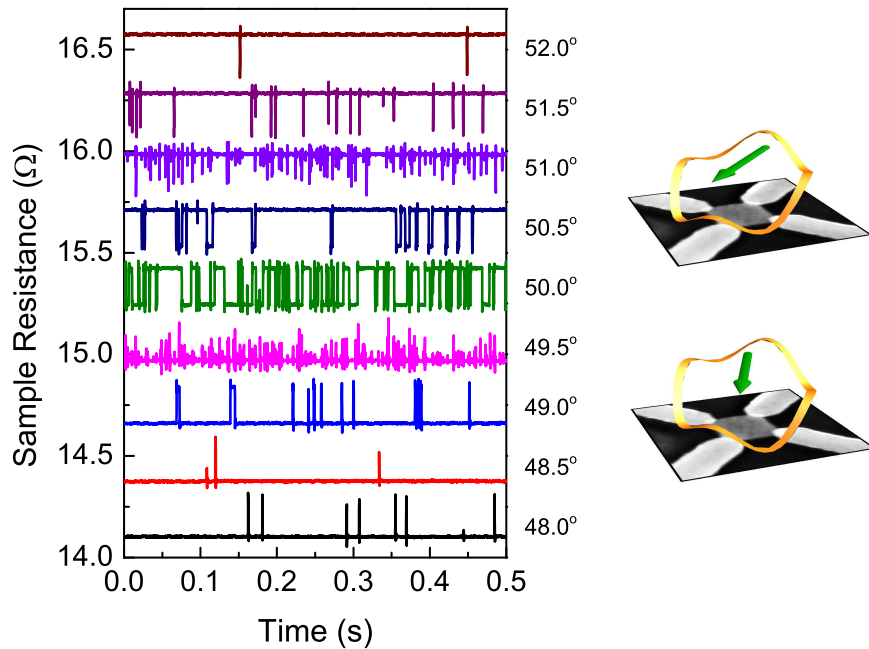


Figure 4.8: Sample resistance for a 300 nm dot plotted as a function of time for an applied field of 17 Oe for the applied field directions indicated in the figure. The data are offset for clarity. The maximum telegraph noise does not occur at  $45^\circ$  for this sample due to imperfections introduced in fabrication. Two energy surface plots are provided to demonstrate how applied fields away from  $45^\circ$  create energy minima of different depths and therefore different telegraph frequencies. The upper plot is for a field at  $45^\circ$  while the lower plot shows the exaggerated effect at an applied field of  $25^\circ$ .

the predictions of our model but additional quantitative work could extend this analysis and possibly test if the angular dependence of the configurational anisotropy energy is sinusoidal.

### 4.3 Micromagnetic Simulations of Noise

We confirmed our understanding of the magnetic RTN observed in our samples through micromagnetic simulations conducted by Randall Victora and Chad Weigelt.

#### 4.3.1 Simulations of Hysteresis Loops Along the Dot Diagonal

We first verified that in hysteresis loops measured with the applied field along the dot diagonal the magnetization randomly chooses to point along one of the directions parallel

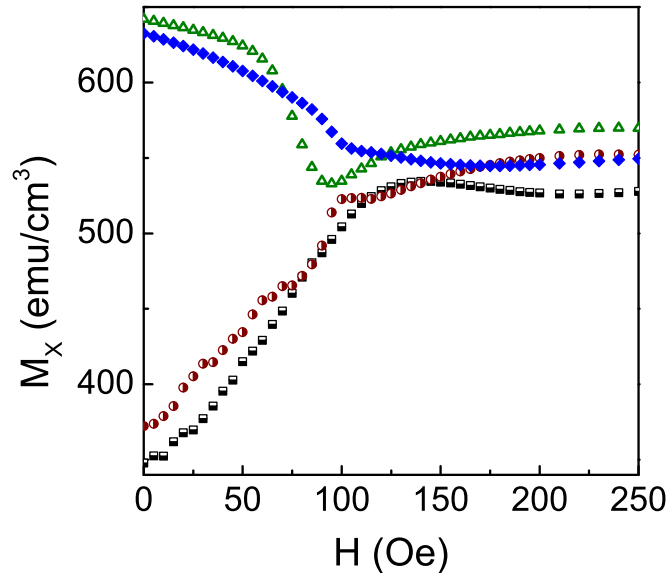


Figure 4.9: The x-component (in-plane, parallel to an edge of the square) of the magnetization simulated for a 200 nm dot plotted as a function of the applied field magnitude along the dot diagonal for four consecutive simulations starting from a large applied field. The lack of noise in this plot is due to the nanosecond time scales over which each data point is simulated. Data taken from simulations by Randall Victora and Chad Weigelt.

to the edges of the dot as the field is reduced. The field dependence of the magnetization of a square dot is shown for a 200 nm square dot with the field applied along the dot diagonal in Fig. 4.9. Four simulation data sets are shown. In each data set, the field is swept from a 200 Oe to 0 Oe under identical conditions but with different random number seeds used in generating the thermal fluctuations. Half of the simulations rotate to point along one of the dot edges at zero field and the other half rotate to point along the other edge. This reproduces our observations for hysteresis loops taken with applied fields along the dot diagonal that the magnetization randomly selects a remnant magnetic state parallel to one of the edges. The relative absence of telegraph noise between the two magnetic states at intermediate fields is primarily a result of the short time over which these simulations were run.

We also note that there is some separation between the simulation curves at very high fields. This effect may be an artifact of the simulation time or a result of the discretization of the simulated dot into a finite number of cells, though initial investigations suggest that neither of these explanations is valid. A remaining possible explanation is that

the separation between the curves may be the result of a higher order configurational anisotropy term exerting its influence over the dot magnetization even at high fields.

### 4.3.2 Simulations of Thermally Driven Telegraph Noise

The simulations also reproduce the RTN seen in our samples when the field is fixed at certain values along the dot diagonal. Applied field values were chosen so that the two magnetic states would be distinguishable but with a sufficiently small energy barrier that switching occurred within a reasonable amount of simulation time. The resultant magnetization of the dot as a function of time at applied fields of 30-55 Oe is shown in Fig. 4.10. In this plot well-defined random telegraph switching of the magnetization between two easily distinguishable magnetic states is observed. For the sake of simulation time, the telegraph frequencies in this simulation were quite large ( $\sim 100$  kHz) which is at the upper end of our experimental bandwidth. Thus, we were not able to achieve complete overlap of the experimental data with the simulations. However, there is no reason to believe that the simulation would show significant change in the behavior of the magnetization if the

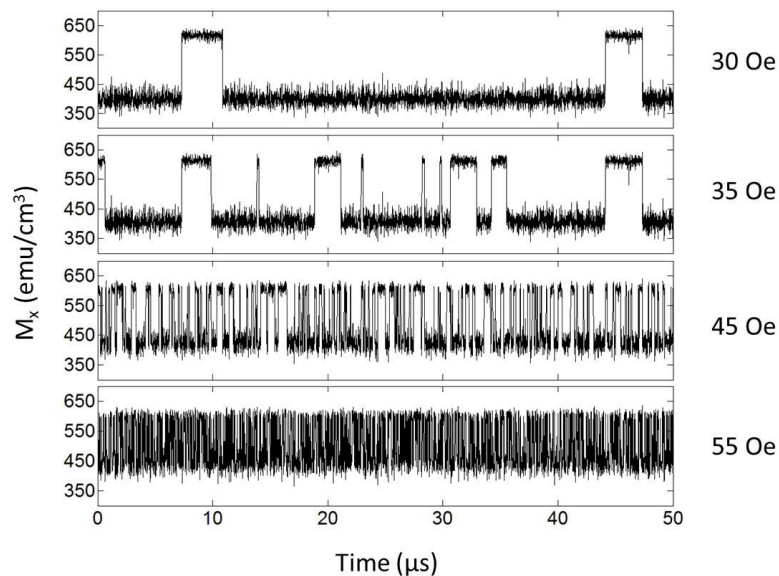


Figure 4.10: Simulated telegraph noise for a 200 nm square dot with an applied field aligned to the dot diagonal. The x-component of the magnetization is plotted as a function of time for the applied fields indicated in the figure. Data taken from simulations by Randall Victora and Chad Weigelt.

same simulation were run at smaller fields where the longer telegraph state lifetimes would be expected. In addition, data taken at different field magnitudes showed an increase in the telegraph frequency with increasing field as expected.

### 4.3.3 Magnetization Configuration of Telegraph States

Since the micromagnetic simulations rely on the behavior of the discretized cells within the dot, the simulations also provide information about the magnetic configurations of the two telegraph states. The vector fields representing the magnetic moments of the discretization cells (averaged over four adjacent cells) are shown for the dot in Fig. 4.11. These two states were taken from data points immediately before and after the magnetization switched. The net magnetization in both states is nearly parallel to the dot edges and the largest changes in the magnetization occur at the center of the dot. This supports our conclusions that the telegraph noise observed in our samples does arise from a change in the bulk magnetization state of the sample and not simply a fluctuation of the magnetization in one of the corners of the sample. The states exhibit ‘S’ shaped magnetization similar to those discussed in Sec. 3.8.2.

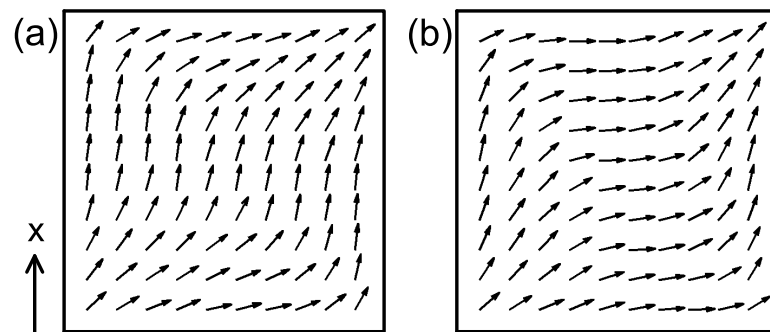


Figure 4.11: Plots of the simulated magnetization configurations for a 200 nm square dot immediately (a) before and (b) after a switching event such as those shown in Fig. 4.10. Each vector represents the average in-plane magnetization vector of four simulation cells. Data taken from simulations by Randall Victora and Chad Weigelt.

## Chapter 5

# Conclusions and Future Directions

We have demonstrated that the magnetic noise observed in square Permalloy dots originates from thermal fluctuations of the magnetization over energy barriers caused by a configurational anisotropy. In this chapter, we summarize our results, place our conclusions within the context of the larger body of research on magnetic noise, and suggest avenues of further research based on this work.

### 5.1 Conclusions

#### 5.1.1 Quantifying the Magnetic Energy Landscape in Square Dots

The configurational anisotropy in square dots results from competition between the magnetostatic and exchange energies due to the dot geometry. The corresponding energy landscape was determined in individual dots using two methods. The first method measured the magnetization direction as the magnetic field was rotated in the plane of the dot for a variety of magnetic field magnitudes. In the second method, the field direction was fixed while magnitude was varied and the coercivity of the sample was identified. In both of these experiments, the direction of the magnetization was determined by 4-terminal resistance measurements using the AMR to relate changes in resistance to changes in magnetization. From these measurements, a four-fold anisotropy energy can be identified which favors magnetization parallel to the dot edges. A Stoner-Wohlfarth model of the magnetization explains the magnetic behavior of our samples. It also provides a method to calculate the magnitude of the configurational anisotropy energy based on the rotational

hysteresis data and the easy-axes coercivities. Both of these measurements are independent of the noise observed in our samples; the two methods agree across a range of dot side lengths from 200 nm to 500 nm and both methods are consistent with the energies determined from an analysis of the noise data. Micromagnetic simulations reproduced the observed hysteresis due to the configurational anisotropy providing further confirmation of our model of this system. These simulations also reveal the underlying magnetic configurations and explain other effects in the experimental data not captured by our simple model.

While characterization of the magnetic behavior in these samples is primarily intended to explain the magnetic noise observed, these results have additional impact. First, they confirm and improve upon the measurements made by Cowburn *et al.* on arrays of square dots [54, 56]. Since individual dots are measured, well-defined magnetic switching fields can be identified that are not blurred by averaging over arrays of dots. Measuring the behavior of individual dots allows characterization of dot-to-dot variations and is applicable to research on magnetic cellular automata digital logic networks [83, 84]; this research, in brief, proposes 'circuits' of interacting magnetic dots as a current free computing logic paradigm. Extensions of our work could be used both in designing these networks and as a method of reading out the magnetic state of individual dots [85, 86].

### 5.1.2 Discovering and Explaining Magnetic Noise in Square Dots

Magnetic noise occurs in square permalloy dots as a direct consequence of the configurational anisotropy. An applied magnetic field oriented along the dot diagonal reduces the local energy maximum, which allows thermal energies to drive fluctuations of the magnetization between the low energy magnetic states parallel to the dot edge. The resultant magnetic noise has a Lorentzian power spectrum as expected for random telegraph noise (RTN). In characterizing the noise through the average switching frequency, we have demonstrated that our model of the magnetization explains the dependence on applied field magnitude, applied field direction, and temperature. Micromagnetic simulations conducted at finite temperature also exhibit RTN. Thus, we have fully characterized a model system where unambiguous magnetic noise is reproducible and highly tunable.

This work provides, first and foremost, a complete model system for studying magnetic RTN where all parameters necessary to observe the noise signatures can be controlled experimentally. This can be contrasted with previous observations of magnetic RTN

where the RTN could only be attributed to defect pinning of domain walls [34–37], was hypothesized to originate from hopping of a magnetic vortex between surface defects [33], and could be measured but not reproducibly controlled in randomly shaped magnetic particles [30–32, 38]. Since we measure isolated magnetic particles with a single magnetic layer and a well characterized magnetic energy we definitively identify the physical origin of the magnetic noise observed in this system.

Addressing the larger body of literature where magnetic noise has been reported, this work clarifies some disagreement over the existence of power law type magnetic noise. Frequency dependencies of the form  $1/f^\alpha$  have been observed with exponents  $\alpha$  ranging from 1 to 2 [87]. Guo *et al.* showed that the magnetic after-effect, which is not a reversible fluctuation, gives rise to a  $1/f^{1.7}$  power spectrum [59, 88]. This thesis offers a second mechanism to account for cases where  $\alpha \approx 2$  since the high frequency components of RTN have this spectrum. While many claims of magnetic noise lack a mechanism explain to explain the RTN, our work suggests the reported noise could be true reversible fluctuations and that a mechanism likely exists. In the smallest samples, where the magnetization should be quasi-single domain our analysis would directly apply [34]. However, in larger samples the magnetization likely reverses through domain wall motion [35, 36]; noise in domain wall motion would require further research as proposed in Sec. 5.2.6.

## 5.2 Future Experimental Directions and Open Questions

### 5.2.1 Configurational Anisotropy Phase Change

While the experiments in this thesis identify the configurational anisotropy in square dots, several questions remain regarding its properties. The size dependence of the configurational anisotropy was found to be linear as a function of dot size, as shown in Fig. 3.15 but disappears at a finite dot size of about 150 nm. The disappearance of the configurational anisotropy at a similar dot size was observed previously [56]. Several hypotheses may explain these observations. First, the energetically favored magnetization direction may switch from parallel to the dot edge to along the dot direction, as shown in Fig. 1.4. Second, the configurational anisotropy may disappear entirely as the sample size approaches the exchange length and the bending of the magnetization is reduced. And finally, the configurational anisotropy may remain finite but appear to go to zero due to temperature dependent effects like those shown in Fig. 3.16. The magnetization behavior in dots with

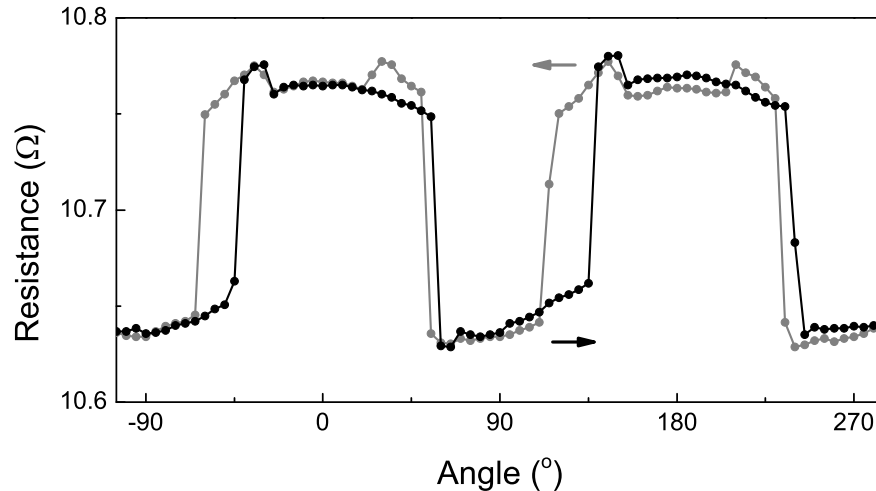


Figure 5.1: The resistance of a 400 nm square dot plotted as a function of applied field direction; the applied field magnitude is 37 Oe and arrows denote rotation directions. Additional structure is apparent in this data (for example, around  $140^\circ$ ) that is not seen in Fig. 3.2. This additional structure is repeatable and may be due to changes in the magnetization configuration within the dot.

side lengths of 75-150 nm would be very different for the three hypotheses described and dots of these sizes should be readily achievable. Thus, the methods described in this thesis could be used to identify the correct hypothesis. We note that these measurements will need to be made at low temperature since the energy barriers for dots of this size will be small.

### 5.2.2 Configurational Anisotropy Angular Dependence

Our model of the magnetization assumes the configurational anisotropy varies sinusoidally with the net magnetization direction. However, symmetry arguments only require the configurational anisotropy to be symmetric under reflection and rotation by  $90^\circ$ . Comparing the experimental data in Fig. 3.9 to the predictions of our model in Fig. 3.13 demonstrates that a sinusoidal angle dependence may not be accurate. The coercivities observed for applied field directions near the easy axis decrease by 10-20% for each 5 degrees of rotation while the model predicts a drop of nearly 50%. A sharper curvature in the local energy minima of the configurational anisotropy would pin the magnetization more strongly and better model the experimental data. The shape of the square also suggests the existence



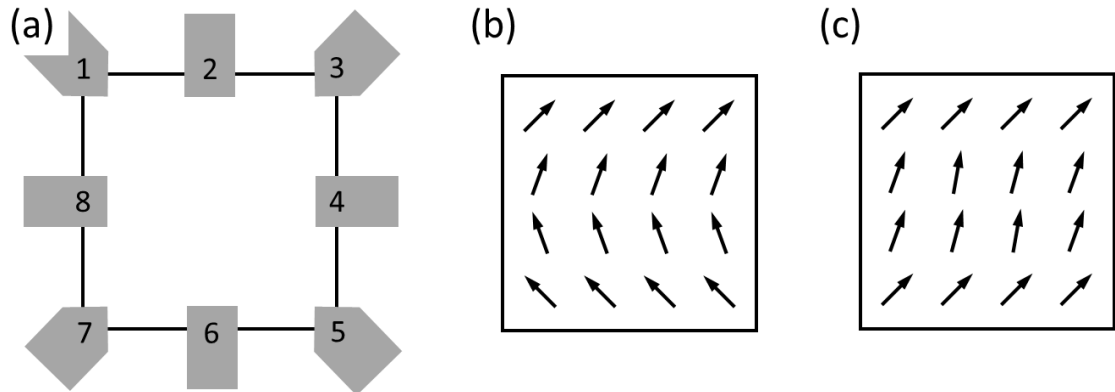


Figure 5.2: (a) A cartoon representation of a square dot fabricated with 8 non-magnetic contacts that could be used to differentiate between (b) ‘C’ shaped and (c) ‘S’ shaped magnetic states. As an example of this measurement, a current could be passed between contacts 3 and 7 along the dot diagonal and the voltage measured simultaneously between contacts 2 and 8 and between 4 and 6. The magnetization between leads 2 and 8 is primarily collinear with the current direction in both the ‘C’ and ‘S’ cases. However, between leads 4 and 6 it is perpendicular to the current in the ‘C’ case but collinear in the ‘S’ case. Thus, by comparing the relative changes in the voltage across the two contact pairs (2-8 and 4-6) for a hysteresis loop, the magnetic state at remanence could be identified.

of a sharper curvature since its Fourier transform in radial coordinates will contain higher order terms beyond the simple four-fold symmetry term.

Additional structure in the rotational hysteresis data was also observed in the micro-magnetic simulation as shown in Fig. 3.18. These abrupt magnetization changes were also observed in several 400 or 500 nm dots, as shown in Fig. 5.1. This additional structure likely stems from reconfigurations of the magnetization at individual dot corners as the magnetization is rotated. Dots containing 8 equally spaced non-magnetic leads could be used to identify these magnetization configurations as demonstrated in Fig. 5.2. When the voltage is measured across two corners of the dot simultaneously, the AMR response for each corner will be dominated by magnetization changes within the dot volume directly between voltage leads. Comparing this information with the vector field plots provided by the simulations could differentiate ‘C’ and ‘S’ shaped magnetization and further characterize the configurational anisotropy.

Finally we note that while permalloy and the square geometry were selected for their simplicity, these techniques could easily be extended to explore additional sample

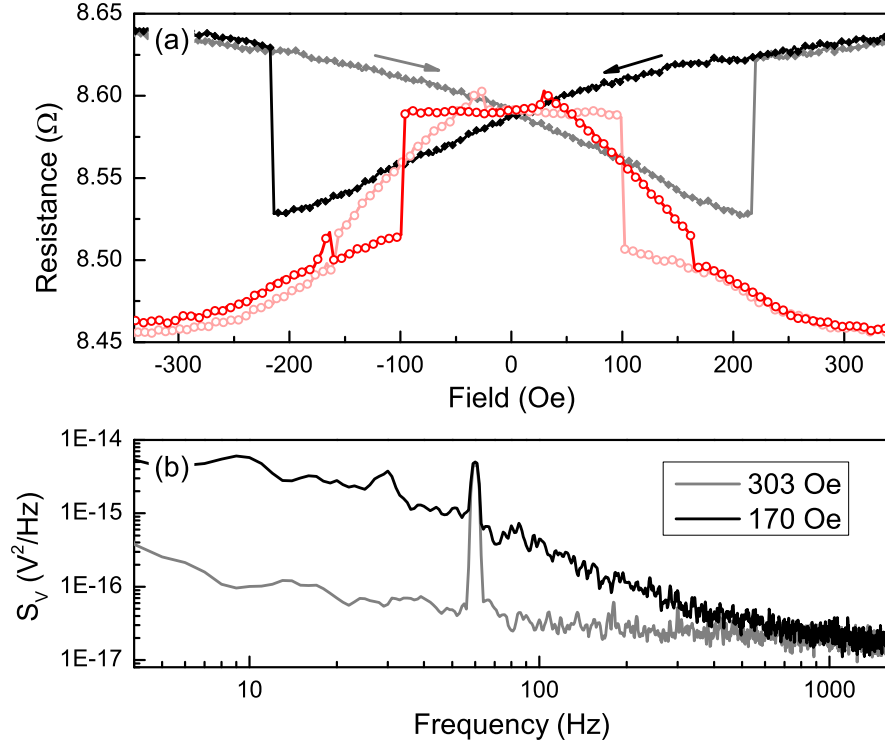


Figure 5.3: Data for a rectangular magnetic dot (200 nm by 250 nm) showing (a) the linear hysteresis for the field applied along the long axis (black filled diamonds) and short axis (red open circles). The shape anisotropy produced by the rectangular shape causes the magnetization to rotate toward the long axis prior to remanence for data taken with the field parallel to the short axis. (b) Noise measurements made for applied fields parallel to the short axis demonstrate that RTN appears at around 170 Oe; data at 303 Oe is provided for reference. This RTN can be explained in the same way that the noise is explained in square dots if a uniaxial shape anisotropy term is included in Eq. 3.2. The noise peak at 60 Hz in (b) is an artifact due to powering the pre-amplifier with an AC outlet.

properties. Triangles and pentagons have been shown to exhibit similar configurational anisotropy energies [56]. Our preliminary measurements on rectangles indicate a coexistence of a configurational and shape anisotropies as shown in Fig. 5.3. In particular, the shape anisotropy introduces a uniaxial anisotropy that modifies the angular position of the magnetic energy minima and changes the applied field conditions where RTN is observed. And studying the interactions of the configurational and magnetocrystalline anisotropies

would be relevant for many magnetic technologies where devices are fabricated from magnetically hard alloys in small square or rectangular geometries [89, 90].

### 5.2.3 Observations of $1/f$ noise

Many of the studies which report magnetic RTN also report observations of  $1/f$  noise in the same samples [34, 35, 37]. While the RTN observed in square dots was emphasized in this thesis,  $1/f$  noise was also observed in these samples. As shown in Fig. 5.4, the  $1/f$  noise was observed for applied fields along the dot diagonal larger than those fields where RTN occurred. The  $1/f$  noise increased in magnitude as the field was reduced. It also may also be present at fields where the RTN was observed but the magnitude of the RTN signal dominated the measured PSD. This  $1/f$  noise was observed in 4 samples but its origin is unknown.

To study magnetic  $1/f$  noise in this system we propose an experiment based on the prediction by Dutta *et al.* [27] in Sec. 1.2.4 that a uniform distribution of two-level fluctuators can produce  $1/f$  noise. Since the dots have a polycrystalline grain structure, the grains could give rise to a distribution of two-level fluctuators. Under this hypothesis,

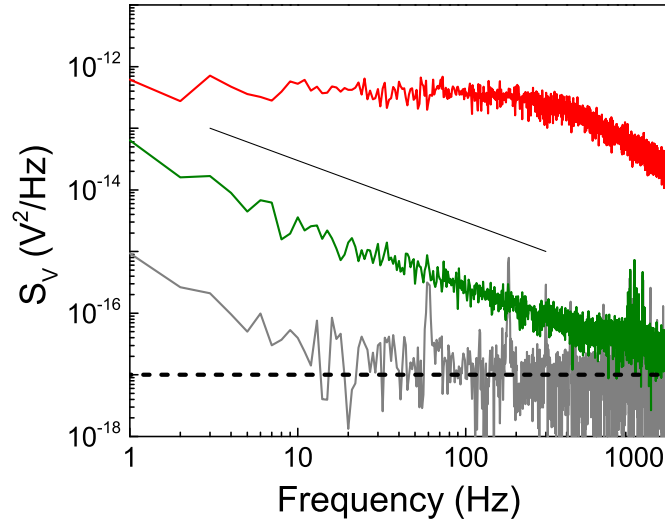


Figure 5.4: Magnetic  $1/f$  noise (green, middle line) observed at 73 Oe in the same 200 nm dot as described in Fig. 4.2. For reference we plot the data at 45 Oe where RTN is observed (red, upper line) and at 215 Oe (gray, lower line) where the noise power agrees with the background Johnson-Nyquist noise (dashed line). The solid black line indicates a  $1/f$  power-law.

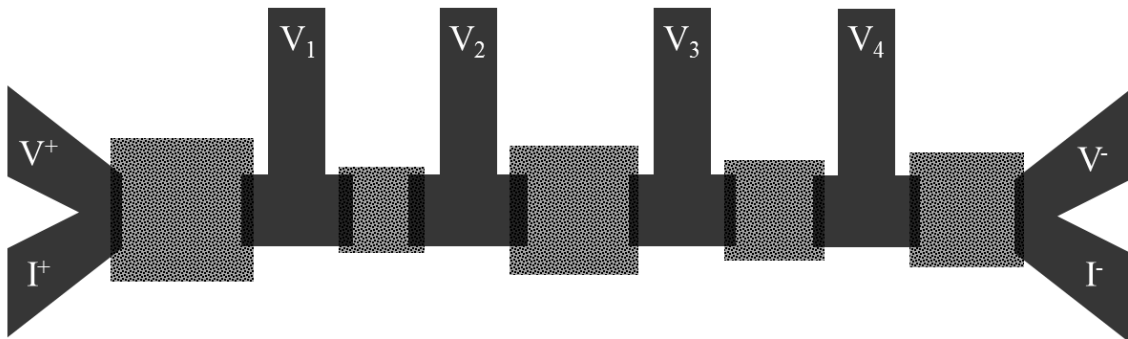


Figure 5.5: A cartoon representation of a series of magnetic dots (textured squares) connected by non-magnetic electrodes (gray bars) that could be used to examine the Dutta *et al.* model of  $1/f$  noise [27]. Chaining a series of dot with different sizes creates a series of two-level fluctuators with a distribution of telegraph frequencies. For the correct distribution,  $1/f$  noise should be observed when the voltage is measured using the leads at either end; the individual telegraph signals could be examined by probing the voltage across any dot with the additional voltage leads (e.g. between  $V_1$  and  $V_2$ ).

relatively weak coupling between grains would allow individual grains to develop multiple low-energy magnetic states. The collective effect of the RTN exhibited by these grains may combine to produce a  $1/f$  magnetic noise signal as predicted by Dutta *et al.* The exchange energies likely make the energetics of these two-state systems quite large, which would result in appropriately low telegraph frequencies comparable to the frequency at which the  $1/f$  noise is observed. By varying the size and distribution of grains within the material it should be possible to identify the role that the grain structure plays in the magnetic  $1/f$  noise of the samples. The sputter deposition parameters [91], the sample seed layer [92], and deposition technique (sputtering vs. evaporation) [93] should affect the sample grain size. This experiment would then provide a top-down approach to study magnetic  $1/f$  noise in this system.

#### 5.2.4 Chained Square Dots

In contrast to the previous experiment, square magnetic dots could also provide a bottom-up approach to studying magnetic  $1/f$  noise and verifying the RTN mechanism proposed by Dutta *et al.* [27]. The telegraph noise in our samples is highly controllable and easily probed. Thus, if several dots were fabricated with non-magnetic electrodes connecting them (Fig. 5.5), experiments could be conducted on a system with tunable RTN sources.

Additional contacts would allow the noise associated with each dot to be measured individually so that the distribution of RTN frequencies and the overall  $1/f$  noise could both be measured in the same samples. And, by varying the spacing between dots, interactions between neighboring dots could also be studied [94–97].

### 5.2.5 Attempt Frequency and High Frequency Effects

As discussed in Chapter 4, the attempt frequency for our square dots based on fitting the data to Eq. 4.3 was approximately 170 GHz (with two additional samples indicating values in the THz range). This value is two orders of magnitude larger than the prediction of 1 GHz for the FMR frequency associated with the configurational anisotropy [82]. Verifying the experimental data in additional samples and extending the data over a wider frequency range would confirm this disagreement with the FMR prediction. At the same time, the curvature of the local energy minimum, which can be measured as described in Sec. 5.2.2, determines the intrinsic frequency of the system. Varying the roundness of the dot corners or skewing the square so that the corner angle is smaller for one diagonal than the other would modify the curvature of the energy minima. It has also been suggested that entropy considerations may modify the attempt frequency [98].

Increasing the accessible frequencies in the experiment would improve the fitting routines used to extract the attempt frequency but would also allow other experimental investigations. Using a high frequency real-time oscilloscope capable of measuring at frequencies up to several GHz, the oscillations of the magnetization within the energy minima of the dot before and after a telegraph switching event may be visible. The rate at which the oscillations decay would reveal information about the damping in the system [70, 76] and the oscillation frequency should be related to the attempt frequency.

### 5.2.6 Domain Wall Measurements

Many reports of magnetic noise, both  $1/f$  and RTN, have attributed the noise to hopping of a domain wall between adjacent pinning sites [34–37]. However, this mechanism has not been definitively identified. To investigate magnetic noise in domain walls, we propose measuring films patterned in a half-circle geometry. As shown in Fig. 5.6, various DC fields can be used to form and manipulate the position of the domain wall in the wire. A giant magnetoresistance (GMR) film would be utilized since it is sensitive to  $180^\circ$  magnetization rotations and one magnetic layer would be pinned through exchange bias

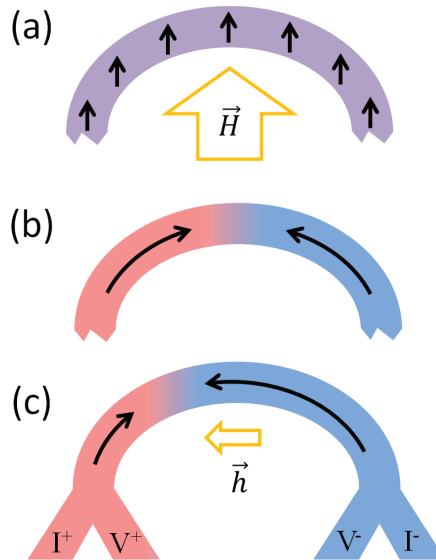


Figure 5.6: A cartoon representation of a half-circle sample geometry useful for studying domain wall noise. A domain wall is formed by (a) applying a large field to saturate the magnetization and then (b) allowing the magnetization to relax into opposing domains via the shape anisotropy when the field is removed. (c) The position of the wall can then be manipulated by a small applied field as indicated, and its position measured through the GMR effect using a four terminal resistance measurement.

[99]. If the reference layer is pinned correctly, the resistance of the device will vary linearly as the wall moves along the wire allowing investigation of thermally activated motion of the wall. Notches [100], nearby magnetic structures [101], or intrinsic defects [102] could introduce pinning sites for the wall and thermally activated domain wall RTN should occur between neighboring sites. If the pinning potentials are characterized in a similar way to that described in this thesis, the mechanism producing domain wall noise can be properly identified.

### 5.2.7 Stochastic Resonance

The phenomena of stochastic resonance refers generally to systems in which the transition rate between low energy states of a system is assisted by the application of a weak external force [103]. Weak, in this case means that the force should not be sufficient to cause a transition in the absence of thermal fluctuations. Systems exhibiting stochastic resonance are of physical interest since the noise in the system improves the strength of the desired

signal, i.e. the signal-to-noise ratio increases as the noise levels are increased [104]. This effect has been observed in spin-valves under the influence of a spin-torque periodic force [105], a rather complex magnetic system. However, a prediction exists for stochastic resonance between two domain wall pinning sites [106].

The simple two-state energetics of the square dots discussed in this thesis could easily be used to study stochastic resonance. Demonstration of the effect could be shown straightforwardly by adding an AC applied field perpendicular to the DC applied field at field values in which the RTN is observed. The full parameter space could then be explored since the energy barrier height, switching frequency, and relative state lifetime are all independently tunable within the dot.

# References

- [1] C. P. Bean, *Journal of Applied Physics* **26**, 1381 (1955).
- [2] C. P. Bean and J. D. Livingston, *Journal of Applied Physics* **30**, S120 (1959).
- [3] C. L. Dennis *et al.*, *Journal of Physics: Condensed Matter* **14**, R1175 (2002).
- [4] J. Martn, J. Nogus, K. Liu, J. Vicent, and I. K. Schuller, *Journal of Magnetism and Magnetic Materials* **256**, 449 (2003).
- [5] R. Wood, *Journal of Magnetism and Magnetic Materials* **321**, 555 (2009).
- [6] D. Weller and A. Moser, *IEEE Transactions on Magnetics* **35**, 4423 (1999).
- [7] H. J. Richter, *Journal of Magnetism and Magnetic Materials* **321**, 467 (2009).
- [8] M. Pannetier, C. Fermon, G. L. Goff, J. Simola, and E. Kerr, *Science* **304**, 1648 (2004).
- [9] W. Egelhoff Jr. *et al.*, *Sensors and Actuators A: Physical* **155**, 217 (2009).
- [10] J. Lenz and A. S. Edelstein, *IEEE Sensors Journal* **6**, 631 (2006).
- [11] Q. A. Pankhurst, J. Connolly, S. K. Jones, and J. Dobson, *Journal of Physics D: Applied Physics* **36**, R167 (2003).
- [12] A. K. Gupta and M. Gupta, *Biomaterials* **26**, 3995 (2005).
- [13] J.-H. Lee *et al.*, *Nature Nanotechnology* **6**, 418 (2011).
- [14] Y. X. Wang, S. M. Hussain, and G. P. Krestin, *European radiology* **11**, 2319 (2001).
- [15] A.-H. Lu, E. L. Salabas, and F. Schth, *Angewandte Chemie International Edition* **46**, 1222 (2007).



- [16] C. Sun, J. S. H. Lee, and M. Zhang, *Advanced Drug Delivery Reviews* **60**, 1252 (2008).
- [17] A. Ambrozy, *Electronic Noise* (Mcgraw-Hill College, 1983).
- [18] J. B. Johnson, *Physical Review* **32**, 97 (1928).
- [19] H. Nyquist, *Physical Review* **32**, 110 (1928).
- [20] W. Schottky, *Annalen der Physik* **362**, 541 (1918).
- [21] S. Machlup, *Journal of Applied Physics* **25**, 341 (1954).
- [22] A. Van Der Ziel, Flicker noise in electronic devices, in *Advances in Electronics and Electron Physics*, edited by L. Marton and C. Marton Vol. 49, pp. 225–297, Academic Press, 1979.
- [23] A. A. Verveen and H. E. Derksen, *Proceedings of the IEEE* **56**, 906916 (1968).
- [24] R. F. Voss and J. Clarke, *The Journal of the Acoustical Society of America* **63**, 258 (1978).
- [25] B. B. Mandelbrot and J. R. Wallis, *Water Resources Research* **5**, 321 (1969).
- [26] P. Dutta and P. M. Horn, *Reviews of Modern Physics* **53**, 497 (1981).
- [27] P. Dutta, P. Dimon, and P. M. Horn, *Physical Review Letters* **43**, 646 (1979).
- [28] N. Smith and P. Arnett, *Applied Physics Letters* **78**, 1448 (2001).
- [29] N. Smith, *Journal of Applied Physics* **90**, 5768 (2001).
- [30] M. Bode, O. Pietzsch, A. Kubetzka, and R. Wiesendanger, *Physical Review Letters* **92**, 067201 (2004).
- [31] W. Wernsdorfer *et al.*, *Physical Review Letters* **78**, 1791 (1997).
- [32] A. Balan *et al.*, *Physical Review Letters* **112**, 107201 (2014).
- [33] J. A. J. Burgess *et al.*, *Science* **339**, 1051 (2013).
- [34] S. Ingvarsson *et al.*, *Physical Review Letters* **85**, 3289 (2000).

- [35] L. Jiang *et al.*, Physical Review B **69**, 054407 (2004).
- [36] J. Scola *et al.*, Applied Physics Letters **90**, 252501 (2007).
- [37] J. F. Feng, Z. Diao, G. Feng, E. R. Nowak, and J. M. D. Coey, Applied Physics Letters **96**, 052504 (2010).
- [38] F. Coppinger *et al.*, Physical Review Letters **75**, 3513 (1995).
- [39] J.-G. J. Zhu and C. Park, Materials Today **9**, 36 (2006).
- [40] A. Ozbay *et al.*, Applied Physics Letters **94**, 202506 (2009).
- [41] B. Zhong, Y. Chen, S. Garzon, T. M. Crawford, and R. A. Webb, Journal of Applied Physics **109**, 07C725 (2011).
- [42] Z. Diao, E. R. Nowak, G. Feng, and J. M. D. Coey, Physical Review Letters **104**, 047202 (2010).
- [43] R. Kubo, Reports on Progress in Physics **29**, 255 (1966).
- [44] B. D. Cullity and C. D. Graham, *Introduction to magnetic materials* (IEEE/Wiley, Hoboken, N.J., 2009).
- [45] R. C. O'Handley, *Modern Magnetic Materials: Principles and Applications*, 1st ed. (Wiley-Interscience, 1999).
- [46] N. Imamura and S. Chikazumi, Journal of the Physical Society of Japan **25**, 125 (1968).
- [47] G. Abo *et al.*, IEEE Transactions on Magnetics **49**, 4937 (2013).
- [48] W. F. Brown, Journal of Applied Physics **39**, 993 (1968).
- [49] H. D. Arnold and G. W. Elmen, Bell System Technical Journal **2**, 101 (1923).
- [50] F. Pfeifer and C. Radloff, Journal of Magnetism and Magnetic Materials **19**, 190 (1980).
- [51] R. Moskowitz and E. Della Torre, IEEE Transactions on Magnetics **2**, 739 (1966).
- [52] R. P. Cowburn and M. E. Welland, Applied Physics Letters **72**, 2041 (1998).

- [53] M. E. Schabes and H. N. Bertram, *Journal of Applied Physics* **64**, 1347 (1988).
- [54] R. P. Cowburn, A. O. Adeyeye, and M. E. Welland, *Physical Review Letters* **81**, 5414 (1998).
- [55] R. P. Cowburn and M. E. Welland, *Physical Review B* **58**, 9217 (1998).
- [56] R. P. Cowburn, *Journal of Physics D: Applied Physics* **33**, R1 (2000).
- [57] L. Neel, *Ann. Geophys.* **5**, 99 (1949).
- [58] W. F. Brown, *Physical Review* **130**, 1677 (1963).
- [59] F. Guo, G. McKusky, and E. D. Dahlberg, *Applied Physics Letters* **95**, 062512 (2009).
- [60] W. K. Park *et al.*, *Journal of Applied Physics* **93**, 7020 (2003).
- [61] D. E. Endean, C. T. Weigelt, R. H. Victora, and E. D. Dahlberg, *Applied Physics Letters* **103**, 042409 (2013).
- [62] R. P. Cowburn, A. Ercole, S. J. Gray, and J. a. C. Bland, *Journal of Applied Physics* **81**, 6879 (1997).
- [63] J. I. Gittleman, B. Abeles, and S. Bozowski, *Physical Review B* **9**, 3891 (1974).
- [64] T. McGuire and R. Potter, *IEEE Transactions on Magnetism* **11**, 1018 (1975).
- [65] D. J. Griffiths, *Introduction to Electrodynamics*, 3rd ed. (Addison Wesley, Upper Saddle River, N.J, 1999).
- [66] D. Rffer, F. D. Czeschka, R. Gross, and S. T. B. Goennenwein, *Applied Physics Letters* **99**, 142112 (2011).
- [67] R. M. Bozorth, *Physical Review* **70**, 923 (1946).
- [68] W.-Y. Lee, M. F. Toney, P. Tameerug, E. Allen, and D. Mauri, *Journal of Applied Physics* **87**, 6992 (2000).
- [69] L. D. Landau and E. Lifshitz, *Phys. Z. Sowjetunion* **8**, 101114 (1935).
- [70] T. Gilbert, *IEEE Transactions on Magnetism* **40**, 3443 (2004).

- [71] J. Fidler and T. Schrefl, *Journal of Physics D: Applied Physics* **33**, R135 (2000).
- [72] M. R. Scheinfein, LLG micromagnetics simulator, 2004.
- [73] W. H. Meiklejohn and C. P. Bean, *Physical Review* **105**, 904 (1957).
- [74] J. Nogus and I. K. Schuller, *Journal of Magnetism and Magnetic Materials* **192**, 203 (1999).
- [75] E. C. Stoner and E. P. Wohlfarth, *Philosophical Transactions of the Royal Society of London. Series A, Mathematical and Physical Sciences* **240**, 599 (1948).
- [76] K. Gilmore, Y. U. Idzerda, and M. D. Stiles, *Physical Review Letters* **99**, 027204 (2007).
- [77] W. J. Gibbs, *Nature* **59**, 200 (1898).
- [78] Y. Yuzhelevski, M. Yuzhelevski, and G. Jung, *Review of Scientific Instruments* **71**, 1681 (2000).
- [79] N. D. Rizzo, T. J. Silva, and A. B. Kos, *Physical Review Letters* **83**, 4876 (1999).
- [80] S. I. Woods, J. R. Kirtley, S. Sun, and R. H. Koch, *Physical Review Letters* **87**, 137205 (2001).
- [81] S. Krause *et al.*, *Physical Review Letters* **103**, 127202 (2009).
- [82] C. Kittel, *Introduction to Solid State Physics*, 8th ed. (Wiley, Hoboken, NJ, 2004).
- [83] R. P. Cowburn and M. E. Welland, *Science* **287**, 1466 (2000).
- [84] A. Imre *et al.*, *Science* **311**, 205 (2006).
- [85] B. Lambson *et al.*, *Applied Physics Letters* **100**, 152406 (2012).
- [86] M. Niemier *et al.*, *IEEE Transactions on Nanotechnology* **11**, 220 (2012).
- [87] R. Guerrero *et al.*, *Journal of Physics D: Applied Physics* **35**, 1761 (2002).
- [88] F. Guo, G. McKusky, and E. D. Dahlberg, *Physical Review B* **88**, 014409 (2013).
- [89] P. Vavassori *et al.*, *Physical Review B* **72**, 054405 (2005).

- [90] D. B. Carlton, N. C. Emley, E. Tuchfeld, and J. Bokor, *Nano Letters* **8**, 4173 (2008).
- [91] M. Vopsaroiu, M. J. Thwaites, S. Rand, P. Grundy, and K. O'Grady, *IEEE Transactions on Magnetics* **40**, 2443 (2004).
- [92] W. Lee, M. Toney, and D. Mauri, *IEEE Transactions on Magnetics* **36**, 381 (2000).
- [93] G. Reiss *et al.*, *Journal of Magnetism and Magnetic Materials* **184**, 281 (1998).
- [94] S. A. Majetich and M. Sachan, *Journal of Physics D: Applied Physics* **39**, R407 (2006).
- [95] R. P. Cowburn, A. O. Adeyeye, and M. E. Welland, *New Journal of Physics* **1**, 16 (1999).
- [96] V. Novosad *et al.*, *Applied Physics Letters* **82**, 3716 (2003).
- [97] H.-J. Jang, P. Eames, E. D. Dahlberg, M. Farhoud, and C. A. Ross, *Applied Physics Letters* **86**, 023102 (2004).
- [98] S. Chandrasekhar, *Reviews of Modern Physics* **15**, 1 (1943).
- [99] T. Klein *et al.*, *IEEE Transactions on Magnetics* **49**, 3414 (2013).
- [100] M. Klui *et al.*, *Applied Physics Letters* **87**, 102509 (2005).
- [101] L. O'Brien *et al.*, *Physical Review Letters* **106**, 087204 (2011).
- [102] D.-H. Kim, S.-B. Choe, and S.-C. Shin, *Physical Review Letters* **90**, 087203 (2003).
- [103] L. Gammaitoni, P. Hnggi, P. Jung, and F. Marchesoni, *Reviews of Modern Physics* **70**, 223 (1998).
- [104] J. M. G. Vilar and J. M. Rub, *Physical Review Letters* **77**, 2863 (1996).
- [105] X. Cheng, C. T. Boone, J. Zhu, and I. N. Krivorotov, *Physical Review Letters* **105**, 047202 (2010).
- [106] E. Martinez, G. Finocchio, and M. Carpentieri, *Applied Physics Letters* **98**, 072507 (2011).
- [107] M. N. Baibich *et al.*, *Physical Review Letters* **61**, 2472 (1988).

- [108] G. Binasch, P. Grnberg, F. Saurenbach, and W. Zinn, *Physical Review B* **39**, 4828 (1989).
- [109] W. P. Pratt *et al.*, *Physical Review Letters* **66**, 3060 (1991).
- [110] M. A. M. Gijs, S. K. J. Lenczowski, and J. B. Giesbers, *Physical Review Letters* **70**, 3343 (1993).
- [111] S. Zhang and P. M. Levy, *Journal of Applied Physics* **69**, 4786 (1991).
- [112] J. Jacquet and T. Valet, A new magneto-optical effect discovered on magnetic multilayers: The magnetorefractive effect, in *Magnetic Ultrathin Films, Multilayers, and Surfaces*, edited by E. Marinero, Materials Research Society, Pittsburgh, 1995.
- [113] J. J. Krebs, P. Lubitz, A. Chaiken, and G. A. Prinz, *Journal of Applied Physics* **69**, 4795 (1991).
- [114] V. V. Ustinov, A. B. Rinkevich, and L. N. Romashev, *Journal of Magnetism and Magnetic Materials* **198**, 82 (1999).
- [115] V. V. Ustinov, A. B. Rinkevich, L. N. Romashev, and V. I. Minin, *Journal of Magnetism and Magnetic Materials* **177**, 1205 (1998).
- [116] T. Stanton, T. Deakin, M. Vopsaroiu, V. Artyushenko, and S. Thompson, *IEEE Transactions on Magnetics* **43**, 2767 (2007).
- [117] B. K. Kuanr, A. V. Kuanr, P. Grnberg, and G. Nimtz, *Physics Letters A* **221**, 245 (1996).
- [118] Z. Frait, P. turc, K. Temst, Y. Bruynseraede, and I. Vvra, *Solid State Communications* **112**, 569 (1999).
- [119] T. Rausch, T. Szczurek, and M. Schlesinger, *Journal of Applied Physics* **85**, 314 (1999).
- [120] R. J. Baxter *et al.*, *Journal of Physics: Condensed Matter* **15**, L695 (2003).
- [121] D. E. Endean, J. N. Heyman, S. Maat, and E. D. Dahlberg, *Physical Review B* **84**, 212405 (2011).
- [122] L. Van Der Pauw, *Philips Res. Rep.* **13**, 1 (1958).

- [123] J. D. Jackson, *Classical Electrodynamics Third Edition*, 3rd ed. (Wiley, New York, 1998).
- [124] R. L. Ramey and T. S. Lewis, *Journal of Applied Physics* **39**, 1747 (1968).
- [125] R. Havemann and L. Davis, *IEEE Transactions on Microwave Theory and Techniques* **19**, 113 (1971).
- [126] R. L. Ramey, W. J. Kitchen Jr., J. M. Lloyd, and H. S. Landes, *Journal of Applied Physics* **39**, 3883 (1968).
- [127] C. Kittel, *Physical Review* **76**, 743 (1949).

## Appendix A

# Microwave Measurements of Giant Magnetoresistance

Multilayer thin films composed of alternating ferromagnetic and non-magnetic metallic layers display an increase in resistance as the magnetizations of the ferromagnetic layers are changed from parallel to anti-parallel alignment. This effect, giant magnetoresistance (GMR), was awarded the Nobel Prize in physics in 2008 [107, 108]. GMR, and related phenomena, are the underlying effect used in all modern hard-drive read heads. We report here work done in studying GMR at microwave frequencies.

### A.1 Experimental Motivation and Goals

This work was originally motivated by an effort to characterize an anisotropy in the magnitude of the GMR effect with applied current direction. While this original experiment lacked sensitivity to this effect, a second experiment was completed that quantified GMR at microwave frequencies. We begin by discussing the motivation for these two experimental questions.

#### A.1.1 GMR Dependence on Current Direction

GMR has been studied extensively for currents flowing in the plane of the film (CIP) and to a lesser extent for currents passing perpendicular to the plane (CPP). Experimental challenges limit comparison between CPP and CIP GMR since the resistance of the sample changes by 5 to 10 orders of magnitude for the two geometries. So far comparison studies



have either been restricted to cryogenic temperatures, necessary to create superconducting contacts and eliminate contact resistance [109], or specially fabricated nano-wires with sample areas sufficiently small to yield a measureable resistance [110]. The former relies on a super-lattice of 100 or more metallic layers for which the magnetization direction of individual layers cannot be determined. In the latter case, the distribution of current within the films is also non-uniform and must be corrected by computer simulation. Theoretically, it is simpler to model than CPP-GMR than CIP-GMR since the current must flow through each layer in the CPP case. Zhang and Levy predict that the magnetoresistance for the CPP geometry should be several times larger than in the CIP geometry which motivates experimental comparisons of CIP and CPP GMR [111].

To investigate CIP and CPP GMR, some work has been done using measurements at high frequencies in the infrared regime [112] and the microwave regime [113–115]. Ustinov *et al.* observed the microwave analogue to CIP and CPP GMR in the reflection or transmission coefficient and the changes correlate well with CIP resistance measurements [114, 115]. However fundamental differences in the experimental methods used for the two geometries prevent a direct comparison between the magnitudes of CIP and CPP GMR. Thus, we attempted to develop microwave technique capable of comparing the magnitudes of CIP and CPP GMR in GMR films with only two magnetic layers allowing a definite understanding of the relative orientation of the two magnetizations.

### A.1.2 Quantifying GMR at Microwave Frequencies

While the experiments above were insensitive to the CPP-GMR of our samples, we were able to quantitatively characterize GMR at microwave frequencies in the CIP geometry. Generally GMR is measured at low frequency (audio frequencies) in standard transport measurements. Since the time scale for electron scattering is short, the GMR effect should persist to significantly higher frequencies such as microwave and even far-infrared frequencies; Krebs *et al.* first observed GMR in the microwave regime ( $\mu$ GMR) [113] and, later, Jacquet and Valet observed the magnetorefractive effect (MRE) in the infrared regime [112]. These high frequency measurement techniques may find application as a non-contact method to measure GMR [116].

The  $\mu$ GMR effect has been observed in a variety of geometries such as resonant cavities [113, 114, 117], by direct measurement of transmission [115] or differential absorption [118] and in an antenna circuit [119]. These results all show a correlation between transport

GMR and the  $\mu$ GMR but the explanations provided [115, 118] simply predict a correlation and do not quantify the magnitude of the effect. Experiments have also been limited to separate measurements of transmission or absorption and have neglected the reflection coefficient. Quantitative efforts have been made in the infrared regime, but an inter-band conduction calculation beyond the simple Drude model appears necessary to quantitatively explain the MRE effect [112, 120]. Thus, we determine whether the complex spin and frequency dependent Drude model necessary to explain GMR at infrared frequencies is necessary to achieve quantitative agreement with observations at microwave frequencies.

## A.2 Sample Fabrication

For both experiments, GMR films and simple metallic films were grown on Si substrates coated with 100 nm of  $\text{Si}_3\text{N}_4$  and deposited using dc-magnetron sputtering in an Ar atmosphere at 3 mTorr. The GMR films were exchanged biased and of the form Si/ $\text{Si}_3\text{N}_4$  100 nm/Ta 20 nm/Py 30 nm/IrMn 60 nm/CoFe  $t_{\text{CoFe}}$  nm/Cu  $t_{\text{Cu}}$  nm/CoFe 10 nm/ Py 20 nm/Ta 20 nm, where  $t_{\text{CoFe}}$  and  $t_{\text{Cu}}$  were varied from 10 to 45 nm while the thickness of the other layer was held constant at 25 nm. The samples were grown in a field of 1.5 kOe to set the exchange bias of the bottom magnetic layer.

## A.3 Attempts to Measure CPP-GMR

Based on the success by previous researchers in measuring CIP-GMR in the microwave and infrared regime, we hypothesized that microwave or infrared radiation incident at an angle to the film surface would probe both CIP and CPP components of the GMR effect. We document our attempts at this experiment and explain its insensitivity to CPP-GMR.

### A.3.1 Experimental Design and CPP-GMR Measurements

To compare CIP and CPP GMR using microwaves, we developed an experiment intended to drive currents at an angle to the plane of the film. The electric field of the fundamental mode in rectangular waveguide is everywhere perpendicular both the direction of propagation and the long-axis of the waveguide cross-section. To probe both the CIP and CPP GMR, the GMR film was placed in the waveguide at an angle to this electric field, as shown in Fig. A.1. If the electric field drives currents in the film parallel to the electric

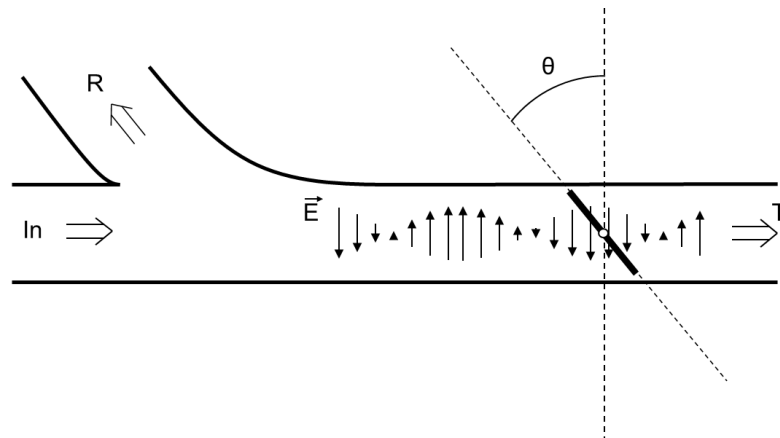


Figure A.1: A cartoon showing the sample orientation in the waveguide and the direction of the electric field where the perspective is parallel to the long-axis of the rectangular waveguide cross-section. The indicated electric field indicate the microwave electric field which has a wavelength of  $\sim 3$  cm. The ‘Y’ at the right represents the directional coupler which forces incoming microwaves from the lower branch to travel leftward while reflected microwaves are forced to return along the upper branch.

field in the waveguide, the change in reflection and transmission caused by changing the magnetic state of the GMR film should depend on the relative amounts of CIP and CPP GMR probed at a given film angle.

The experiment was attempted at both microwave and infrared frequencies in a variety of sample geometries. As an example of the data which was initially thought to indicate a measurement of the CPP-GMR we plot the measured change in reflectivity of the sample as a function of the angle of the sample with respect to the angle of the film with respect to the waveguide electric field in Fig. A.2. From this data it appears that the measured change in reflectivity increases in magnitude as the sample is rotated to larger angles suggesting that the CPP-GMR is larger than the CIP-GMR as predicted.

However, in checking the validity of this measurement we found this apparent sensitivity to CPP-GMR could be explained by other effects. For example, rotating the film around an axis parallel to the electric field also produced an angle dependent response even though under this rotation only the CIP-GMR should be probed. Similarly, the effect disappeared if a smaller sample was used. Thus, all angle dependent effects could be explained by the fact that geometry of the measurement changed as the sample was rotated. Thus, we were unable to produce a measurement which was sensitive to the CPP-GMR and not explained by another effect.

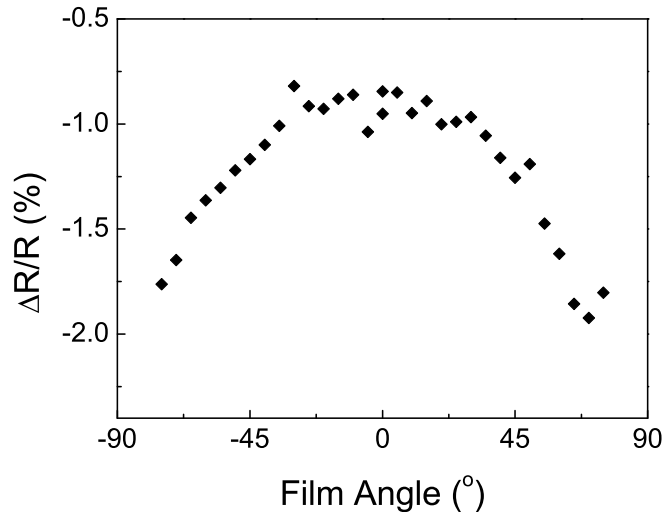


Figure A.2: Change in reflection coefficient measured for a GMR film as a function of the angle of the film in the waveguide. The DC resistance change due to the GMR effect in this film was 5.48%,  $t_{\text{Cu}} = 25$  nm, and  $t_{\text{CoFe}} = 25$  nm. Changes in reflection are plotted as negative numbers since a positive increase in resistance decreases the reflectivity.

### A.3.2 Theoretical Justifications for Infeasibility

While our geometrical effects can account for our experimental data, they do not explain why the experiment was not sensitive to CPP-GMR. Naively, in the limit of zero frequency, electromagnetic waves should behave the same as a DC measurement and probe the conductivity of the material. However, this argument fails ultimately due to the extremely large difference between the dielectric constants of air and the metal film; it can be understood from two perspectives, optics and electronics.

From the perspective of optics, we note that the boundary conditions for Maxwell's equations at the interface of two materials require continuity of the perpendicular component of the displacement, which is proportional to the product of the relative dielectric constant of the medium and the electric field [65]. This boundary condition is responsible for refraction. In the case of metal films the dielectric constant is much greater than one so any light incident on the film at an oblique angle from air will be transmitted into the film in a direction nearly perpendicular to the interface. Thus, the electric field of this radiation will be in the plane of the film and only sensitive to the CIP component of GMR.

From an electronics perspective, the fundamental difference between a resistance measurement and the waveguide measurement is the presence of air around the film. Consider

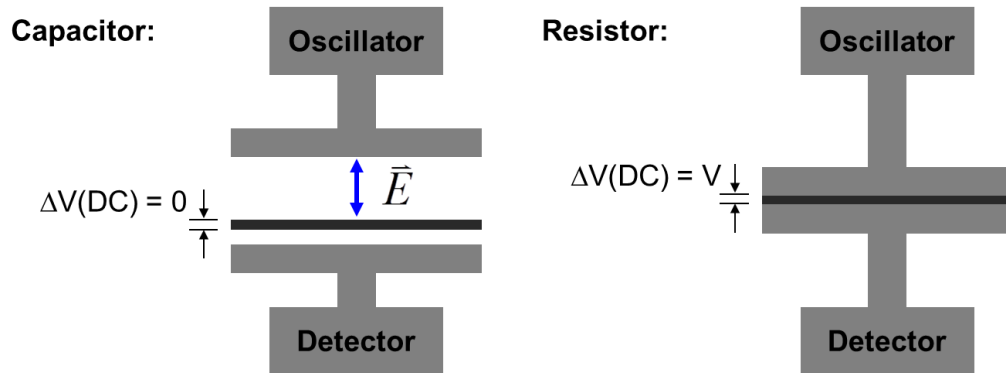


Figure A.3: A cartoon representation which illustrates the failure of the CPP-GMR experiment from an electronics perspective. When the GMR film, shown in black, is placed between two electrodes, shown in gray, with an air gap present a double capacitor is formed and no voltage is developed across the film. By contrast, if direct electrical contact is made to the film, in the case of a resistor, the entire voltage difference will occur across the film. Since the microwave experiment is analogous to the capacitor case, it is insensitive to the CPP component of GMR.

Fig. A.3 which compares the cases where a film is placed in electrical contact with a measurement circuit and one inserted into the air gap of a capacitor. On time scales longer than the transit time of the electrons across the film, the voltage across the film in the capacitor case will be zero. However for the resistor, the voltage applied to the circuit drops entirely across the resistance of the film. The microwave measurement of the perpendicular component of the resistivity is fundamentally the same as the capacitor measurement. Measuring the CPP-GMR in this film using microwaves is analogous to attempting to measure the change in the RC time of the capacitor in Fig. A.3 as the conductivity of the film is changed. Even for a very large capacitor with an extremely small air gap, the change in frequency would be well below any reasonable experimental sensitivity.

## A.4 Quantifying Microwave CIP-GMR

Since our experiments intended to measure CPP-GMR were sensitive to the CIP-GMR of our films, we quantitatively showed that the CIP-GMR of a film agrees well with the observed effect in the microwave regime and obeys Maxwell's equations. The details of this work were published in Ref. [121].

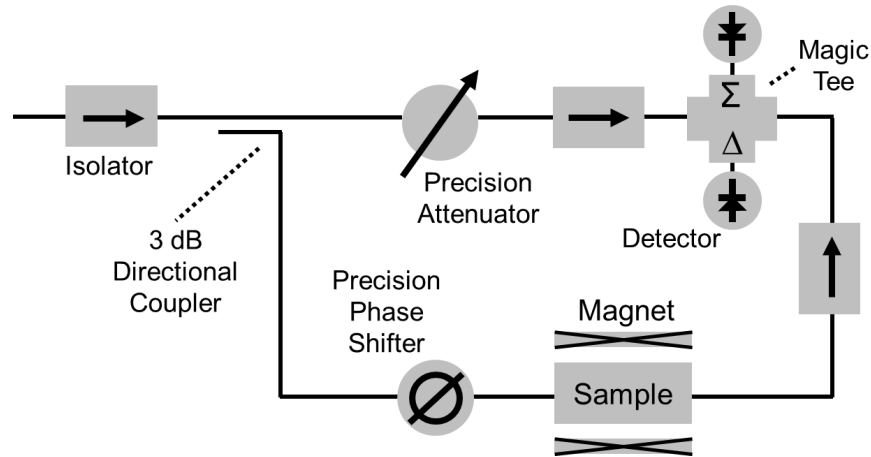


Figure A.4: A cartoon representation of the waveguide bridge used for the quantitative measurements of CIP-GMR in transmission. The magic tee has two ports, a difference and sum port, which ensures a maximum phase shift of  $90^\circ$  is required to null the signal at one of the ports. For the reflection setup, an additional 3 dB directional coupler was added in the lower right corner. The sample was located downstream so that microwaves entered the coupler, reflected off the sample, and were redirected by the coupler to the magic tee.

#### A.4.1 Experimental Design

In measuring CIP-GMR, the sample is not required to rotate. Thus, it was mounted in the plane of the waveguide cross-section on a small plastic block. Silver paint was applied at the edges of the sample to ensure electrical contact with the waveguide walls and eliminate leakage of microwaves around the sample. Glass and  $\text{Si}_3\text{N}_4$  coated Si substrates were both used. Glass yielded better results as the Si substrates were doped sufficiently high that the residual conductivity significantly affected the microwave response. All measurements were made at room temperature; transport measurements utilized the van der Pauw technique to extract the sheet resistance of the sample [122]. The microwave measurements were made at 10.49 GHz using a microwave bridge setup, shown in Fig. A.4, that functioned in the same way as an interferometer. The microwave radiation was split and traveled two nearly equal length paths, one of which contained the sample under study. A directional coupler split the microwave power along the two paths and the microwaves were recombined using a magic tee. By varying the phase shifter and the attenuator, the recombined signal at the magic tee could be nulled. The absolute reflection and transmission coefficients were determined by comparing the necessary attenuation with

and without the sample present (thick copper sheet metal served as a reference for the reflection measurements). Changes in the reflectivity and transmission of the sample caused by the GMR effect were measured by noting changes in the attenuation as the magnetic state of the film changed.

#### A.4.2 Theoretical Predictions

The reflection and transmission coefficients can be calculated directly by solving Maxwells equations with the appropriate boundary conditions [123]. This calculation is identical to that for a plane wave with a modified wavenumber,  $\kappa$ . In X-band rectangular waveguide, the TE<sub>1,0</sub> mode is the fundamental propagating mode and has a wavenumber given by,

$$\kappa = \sqrt{(\pi/a)^2 - \omega^2\mu\epsilon/c^2 + i\omega\mu_0\mu\sigma}, \quad (\text{A.1})$$

where  $a$  is the long-axis dimension of the rectangular waveguide,  $\omega$  is the angular frequency,  $\mu$  and  $\epsilon$  are the relative permeability and permittivity respectively,  $c$  is the speed of light,  $\sigma$  is the conductivity, and  $\mu_0$  is the permeability of free space [124]. The scattering rates for charge carriers in the component metals of our films are much higher than 10 GHz, so the DC conductivity can be used in calculations of the  $\mu$ GMR response. For the glass substrate or the empty waveguide, the third term under the radical may be neglected. If the conductivity of a sample is non-zero or the frequency is below cut-off,  $\kappa$  will have a real component resulting in a non-zero absorption coefficient and attenuation of the microwave amplitude.

Enforcement of the boundary conditions can be done either in the manner given in Ref. [124] or by following Ref. [123] and constructing a transfer matrix. Since the measured conductivity of our samples is an order of magnitude smaller than that for the copper waveguide we assume that only the TE<sub>1,0</sub> mode is present in all regions of the waveguide [124]. The complete expressions for a free standing film are given in Ref. [124] and Ref. [125] gives the complete expression for a film grown on a substrate.

As shown in Ref. [126], the free standing film expressions can be significantly reduced assuming the that that the skin-depth of the film is much less than the film thickness and the impedance mismatch at the air-metal interface is large ( $\kappa_0 \ll \kappa_{film}$ , where  $\kappa_0$  is the propagation constant of the empty waveguide). Addressing the first assumption, at 10 GHz, the skin depth for nickel is 140 nm and is 560 nm for copper, both of which are

more than 10 times larger than the film thickness. The second assumption is true when  $\sigma \ll \epsilon_0\omega$  where  $\sigma$  is the conductivity and  $\epsilon_0$  is the permittivity of free space; even poor conductors meet this criteria at 10 GHz. Under these assumptions the transmission and reflection coefficients can be simplified to:

$$t = 4 \left| 2 + \frac{R_0}{R_s} \right|^{-2} \quad (\text{A.2})$$

and,

$$r = \left| 1 + \frac{2R_s}{R_0} \right|^{-2}, \quad (\text{A.3})$$

where  $R_s$  is the sheet resistance of the film and  $R_0$  is given by the expression:

$$R_0 = \frac{\omega\mu_0}{|\kappa_0|}. \quad (\text{A.4})$$

X-band waveguide has a broad wall dimension of 2.29 cm. At 10.49 GHz, for this waveguide  $|\kappa| = 1.71 \text{ cm}^{-1}$  and  $R_0 = 483.3 \Omega$ . In these expressions it should be noted that there is no dependence on the relative permeability,  $\mu_{film}$ , and that both the conductivity and thickness of the film are represented in the single quantity  $R_s$ . As indicated by Ref. [126], these expressions remain valid across materials with values of  $R_s$  ranging from 0.1  $\Omega$  to 10 k $\Omega$ .

Since the GMR effect depends on the relative orientation of the layer magnetizations we may define the field dependent transport GMR ratio as  $\Delta\rho/\rho(H) = (\rho(H)\rho_P)/\rho_P$  where  $\rho(H)$  is the field dependent resistivity of the film and  $\rho_P$  is the resistivity of the film when the layers are aligned parallel ( $P$ ). Assuming  $\Delta\rho/\rho$  is small and taking  $R_s$  to be the sheet resistance of the film in the  $P$  state, the relative change in the transmission and reflection coefficients defined in the same way are given by

$$\Delta t/t = \frac{2R_0}{R_0 + 2R_s} \Delta\rho/\rho, \quad (\text{A.5})$$

and,

$$\Delta r/r = -\frac{4R_s}{R_0 + 2R_s} \Delta\rho/\rho. \quad (\text{A.6})$$

According to this analysis  $\Delta t/t$  and  $\Delta r/r$  depend linearly on  $\Delta\rho/\rho$  with but with a coefficient of proportionality that depends on  $R_s$ . The negative sign for  $\Delta r/r$  is expected; increasing the resistivity should decrease the reflectivity of the film. It should be noted that this



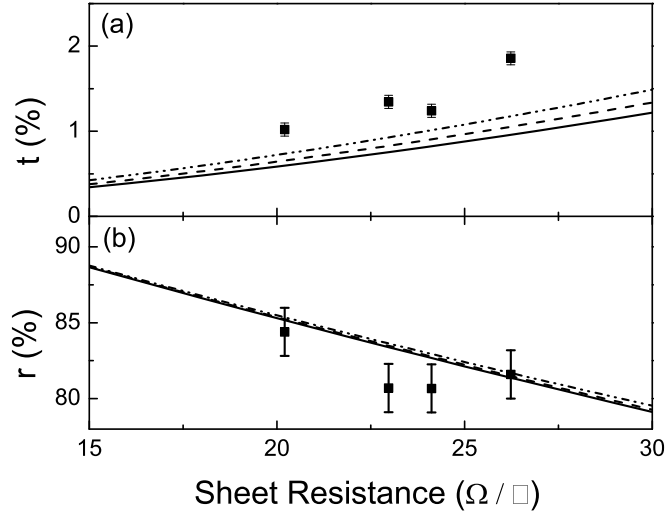


Figure A.5: (a) Transmission and (b) reflection coefficients for plotted as a function of film sheet resistance. The predicted values are shown for a free standing film (solid line) and for a film on a glass substrate with the experimentally determined dielectric constant of 3.3 (dashed line) and the book value dielectric constant of 6.0 (dash-dot line).

model of the microwave GMR response differs from that in Ref. [115] in that it accounts for the effects due to the interfaces in addition to the attenuation due to the skin depth of the samples. While the previous analysis does show a correlation between  $\Delta t/t$  and  $\Delta\rho/\rho$ , it predicts a one-to-one correspondence that is sample and frequency independent and does not predict any observed effect in the reflection coefficient.

### A.4.3 Experimental Observations

A blank sample was placed in the waveguide to estimate the dielectric constant of the glass substrates. The film displayed a transmission coefficient of  $90 \pm 5\%$  and reflection coefficient of  $13 \pm 3\%$ . Based on these data, the dielectric constant of the substrate is approximately 3.3. Since most glasses have a reported dielectric constant of  $\sim 6$ , we consider this value as well below. Figure A.5 shows the reflection and transmission coefficients for the four samples measured along with the theoretical predictions for a free standing film and film grown on a substrate. Both measured quantities agree with the predicted dependences on sheet resistance. Furthermore it is clear that dielectric constant of the substrate does not change the theoretical values significantly.

Figure A.6 shows a comparison between the  $\Delta\rho/\rho$ ,  $\Delta t/t$ ,  $\Delta r/r$  for the sample with  $t_{\text{CoFe}}$

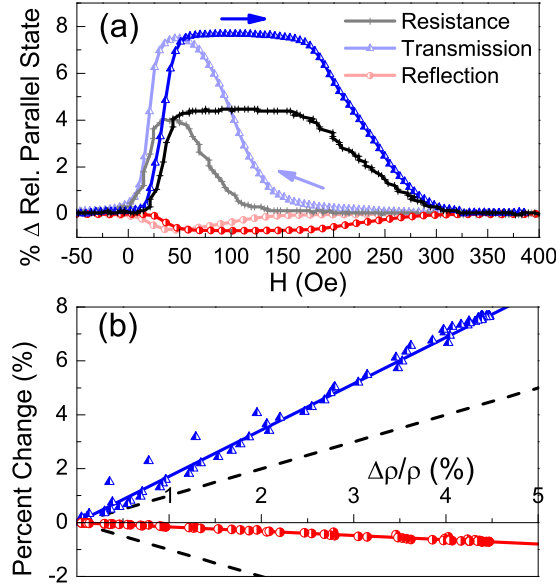


Figure A.6: (a) The applied field dependence of the resistance, transmission, and reflection for a GMR film with  $t_{\text{Cu}} = 25$  nm, and  $t_{\text{CoFe}} = 35$  nm. The sweep directions are indicated by the arrows in the plot with the reverse direction shown in a lighter color. (b) A parametric plot of the transmission and reflection coefficients in (a) as a function of the resistance change. Solid lines indicate linear fits to the data while dashed lines indicate the one-to-one correspondence predicted by Ustinov *et al.* [115]. Reprinted, with permission, from Ref. [121]. Copyright 2011, APS.

$= 35$  nm and  $R_s = 23 \Omega$ . In Fig. A.6(a), the asymmetric dependence of the resistance on applied field due to the exchanged biased bottom magnetic layer is apparent in the microwave data. In Fig. A.6(b), the same data is plotted parametrically as  $\Delta t/t$  vs.  $\Delta\rho/\rho$  and  $\Delta r/r$  vs.  $\Delta\rho/\rho$ . We see clearly that  $\Delta t/t$  and  $\Delta r/r$  are proportional to  $\Delta\rho/\rho$  and that  $\Delta t/t$  shows a larger response while  $\Delta r/r$  is much smaller and of opposite sign. The samples grown on Si substrates yielded qualitatively similar results but the high doping level in the Si complicate the quantitative analysis.

In Fig. A.7 the ratios of  $\Delta t/t$  and  $\Delta r/r$  to  $\Delta\rho/\rho$  are plotted for each of the samples measured and compared to the predicted values based on Eqs. A.5 and A.6 as well as those given by Ref. [125]. The data plotted corresponds to the slopes in Fig. A.6(b) and the coefficients in Eqs. A.5 and A.6. All of these results display the predicted dependences on sheet resistance. Furthermore it is clear that dielectric constant of the substrate does not change the predicted values significantly.

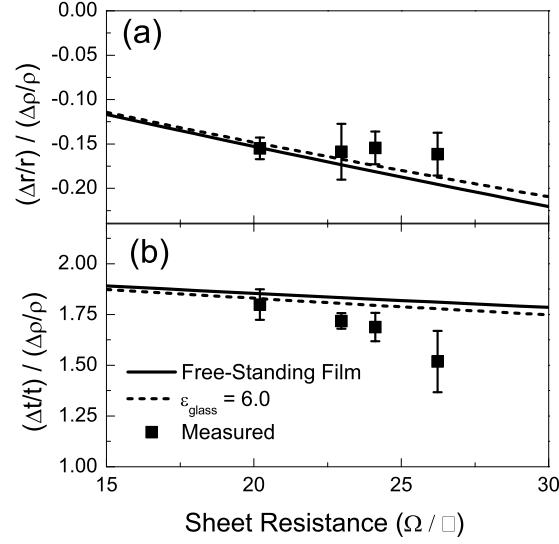


Figure A.7: The ratios of the (a) reflection and (b) transmission coefficient changes to the resistivity change due to the GMR effect for four samples are plotted as a function of the film sheet resistance. The predictions discussed in the text for a free standing film (solid line) and a film on a glass substrate of dielectric constant 6.0 (dashed line) are provided for comparison. Reprinted, with permission, from Ref. [121]. Copyright 2011, APS.

## A.5 Discussion

The ratios of  $\Delta t/t$  to  $\Delta \rho/\rho$  are all significantly larger than unity in contrast to Ref. [115] where the  $\mu$ GMR transmission signal was observed to be approximately proportional to the transport GMR signal and independent of sheet resistance. Since their measurement was made on a super lattice containing Cr non-magnetic layers we expect their samples to have a higher sheet resistance leading to a lower slope in the graph of  $\Delta t/t$  vs.  $\Delta \rho/\rho$ . Their measurements were also at lower frequencies and in waveguide with larger dimensions which may have yielded data supporting a one-to-one correspondence between the relative changes in resistance and transmission. While this one-to-one relationship is predicted by their simplified model based only on the skin depth, their model incorrectly predicts a transmission coefficient near unity and no observed effect in the reflection coefficient. Since they do not report the electrical transport properties of their samples we are unable to verify whether our model accurately describes their data.

It was found that a lack good electrical contact between the sample and waveguide wall reduced  $\Delta t/t$  and  $\Delta r/r$  by nearly an order of magnitude. Discrepancies with the theory

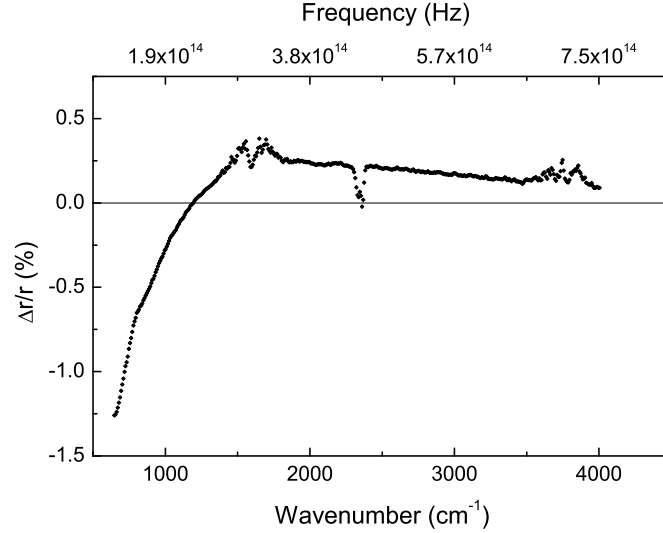


Figure A.8: The change in reflection coefficient due to the GMR film plotted as a function of wavenumber (bottom axis) and frequency (upper axis). The change in sign of the effect is thought to be due to spin dependent scattering rates in the film that are similar to the radiation frequency. The additional structure around  $1500 \text{ cm}^{-1}$ ,  $2300 \text{ cm}^{-1}$ , and  $3500 \text{ cm}^{-1}$  results from absorption lines of atmospheric gases.

in Figs. A.7 and A.5 can be attributed in all measurements primarily to this imperfect electrical contact which systematically decreases the transmission coefficient,  $\Delta^t/t$ , and the magnitude of  $\Delta^r/r$ ; and increases the reflection coefficient. Growing the film *in situ* could provide better electrical contact. The absolute transmission and reflection coefficients rely also on accurate calibration measurements of an open waveguide and ideal reflector.

Based on the above agreement between our experiment and theory, it appears that an intra-band conduction model fully explains the microwave GMR in both transmission and reflection. Since the reflection coefficient in the infrared regime is not well understood and inter-band contributions likely are involved [120], our results indicate that a transition to a more complicated model must occur at frequencies above 10 GHz. We expect this to occur at frequencies around 100 THz since the scattering rates are comparable to the infrared frequencies. We propose measuring the equivalent effect in the THz regime to determine where this crossover occurs.

## A.6 Conclusions and Future Directions

Based on our measurements, the reflectivity and transmission of a GMR films is well understood within Maxwells classical equations of electricity and magnetism and does not require a complex spin and frequency dependent treatment of the film conductivity. However, this is not true at infrared frequencies. At certain frequencies in the infrared regime an increase in the DC resistance may actually produce a decrease in the reflectivity of the film, as demonstrated by our measurements shown in Fig. A.8 and by others. Additional investigation of the nature of these effects could provide additional information related to the spin lifetimes of the charge carriers in a GMR film. In addition, our same analysis could examine whether the anisotropic magnetoresistance (AMR) effect could be observed using a microwave measurement. Since AMR exhibits an in-plane anisotropy, one could examine a possible sensitivity of microwaves to this effect by rotating the magnetization in the film for a fixed microwave electric field in the film.

# Appendix B

## Details of the Fabrication Process

The square permalloy dots studied in this work were fabricated using the tools in the Minnesota Nano Center (MNC) at the University of Minnesota and the DC magnetron sputtering deposition system in the Dahlberg lab. Section B.1 outlines the overall fabrication procedure with the specific optical lithography and EBL recipes listed in Secs. B.2 and B.3 respectively. Additional discussion of these processes can be found in Chapter 2 with a schematic overview of the lift-off processes provided in Fig. 2.4.

### B.1 Fabrication Procedure

1. Alignment Mark and Coarse Contact Definition
  - (a) Follow the bilayer photolithography recipe in Sec. B.2 using the mask for alignment marks and coarse contacts.
    - i. Align the mask to the crystalline axes of the wafer to improve the results of wafer sawing and scribing of the wafers.
    - ii. Use the CHA electron-beam evaporator to deposit 30 nm of Ti followed by 70 nm of Au for a total film thickness of 100 nm.
    - iii. Ti serves as a seed layer to ensure substrate adhesion.
    - iv. Au has a high atomic weight that yields high contrast positive tone alignment marks in the EBL system. Au also reduces the resistance of the contacts.
  - (b) After lift-off is completed, coat the wafer using Shipley Microposit S1813.

- i. This resist layer serves only to prevent particulates from accumulating on the die during wafer dicing.

- (c) Dice the wafer into  $1\text{ cm} \times 1\text{ cm}$  square die following the cut lines defined by the alignment mark mask.

## 2. Dot pattern design

- (a) Sample patterns may be designed using IC Editors Inc.'s IC32 layout software or a similar package to produce GDSII patterns.

- (b) The proprietary software LayoutBEAMER and CJOB developed by Vistec Electron Beam GmbH fractures and assembles a job file for writing the desired pattern.

- i. Small fine details and large coarse areas can be split into separate write routines to improve resolution and write speed respectively.

## 3. Dot Deposition

- (a) Select and clean one or more die for dot deposition.

- i. Labels scribed on the sample back assist in sample identification.

- ii. Spraying the die with acetone while held vertical avoids accumulation of particulate matter from the wafer saw on the die.

- (b) Follow the bilayer EBL recipe in Sec. B.3 to define the magnetic dots

- i. The dots discussed in this work were deposited using magnetron sputtering in the Dahlberg lab.

- ii. The dots in this thesis had the form: 3 nm Ta / 10 nm Py / 3 nm Ta.

- (c) Complete a second EBL lift-off process to deposit the dot electrodes.

- i. Since the alloy composition of the contacts is not critical, electron beam evaporation can be used in this step.

- ii. The contacts in this thesis had the form: 5 nm Ti / 15 nm Au.

- (d) Upon completing this fabrication process, the samples can be measured.

- i. Once the lift-off of the final dot material begins, the samples are electrically isolated and susceptible to ESD.

## B.2 Bilayer Photolithography Recipe

1. Begin with a clean dry substrate.
  - (a) Consider an O<sub>2</sub> plasma etch if the wafer was previously coated in resist.
  - (b) Pre-bake at 150° C for 5 minutes to dehydrate surface.
2. Spin MicroChem LOR-3A onto the wafer at 3000 RPM for 30 seconds.
  - (a) A slow ramp of 500 RPM/s should be used since LOR-3A is a viscous resist.
3. Bake at 170° C for 5 minutes.
4. Spin Shipley S1805 onto the wafer at 3000 RPM for 30 seconds.
  - (a) S1813 can be used if lower resolution features can be tolerated.
5. Soft-bake at 105° C for 1 minute.
6. Expose using the contact aligner.
  - (a) LOR-3A is not light sensitive; exposure parameters should be set for the S1805 resist.
  - (b) Exposure times of around 4 seconds produce sufficient exposure without degrading resolution.
  - (c) Low vacuum contact mode can be used to improve resolution.
7. Develop the S1805 resist in solution of MF-351:H<sub>2</sub>O (1:5) for 25 seconds.
8. Hard-bake the S1805 resist at 125° C for 5 minutes.
9. Develop the LOR-3A resist using undiluted MicroPosit CD-26 for 1 minute.
  - (a) Undercuts of ~ 1.5 μm should be visible at 50x magnification.
10. Deposit desired film.
  - (a) Film thickness should not exceed 1/3 of the thickness of the LOR-3A.
11. Lift-off in MICROPOSIT Remover 1165 for 1 hour at 80° C or overnight at room temperature under a fume hood.



- (a) N-Methyl-2-pyrrolidone (a component of 1165) has a flash-point of 88° C, DO NOT exceed this temperature.
- (b) Sonication may degrade of small features.
- (c) When lift-off is complete, regions where metal is not wanted will appear corrugated and less reflective.
- (d) Without allowing the wafer to dry, spray with acetone (or 1165) over a waste container to dislodge any material which does not easily separate from the wafer.
- (e) Poor lift-off results may be salvaged if the film is not dried but immediately returned to the 1165 stripper bath and sonicated.

### **B.3 Bilayer Electron Beam Lithography Recipe**

1. Start with a clean dry substrate.
  - (a) Consider an O<sub>2</sub> plasma etch if the wafer was previously coated in resist.
  - (b) Pre-bake at 150° C for 5 minutes to dehydrate surface.
  - (c) Since PMGI precipitates in water, clean the sample only with Acetone, Methanol, and Isopropanol (IPA) and dry with N<sub>2</sub>.
2. Spin MicroChem PMGI onto the wafer at 5000 RPM for 30 seconds.
  - (a) A high ramp rate (10 kRPM/sec) will reduce the size of the edge bead.
  - (b) PMGI diluted to 2% concentration in MicroChem T Thinner should be 500 angstroms thick at this spin speed.
  - (c) Changing the resist thickness will influence the development rate. The PMGI layer should be 2-3 times thicker than the deposited film for clean lift-off.
3. Bake the wafer at 180° C for 20 minutes.
  - (a) Higher bake-out temperature may increase adhesion to the substrate but will lower the development rate.
4. Spin MicroChem 950 PMMA onto the wafer at 5000 RPM for 30 seconds.
  - (a) The PMMA should be diluted to 4% in MicroChem A-Thinner

- (b) The MNC will cease stocking anisole thinned PMMA in the near future. A similar recipe can be developed using chlorobenzene thinned PMMA
  - (c) This layer serves as the imaging layer for the final pattern. Its thickness is not critical but must be able to support any suspended portions of the resist in the final pattern.
5. Bake the wafer at 180° C for 20 minutes.
  6. Expose the desired pattern on the Vistec EBPG 5000+.
    - (a) Exposure rates vary and should be determined with a dose test varying logarithmically from 300  $\mu\text{C}/\text{cm}^2$  to 2000  $\mu\text{C}/\text{cm}^2$ .
    - (b) A dose of  $\sim 900 \mu\text{C}/\text{cm}^2$  is expected.
  7. Develop the PMMA resist in MIBK (Methyl isobutyl ketone):IPA (1:3) for 25 seconds.
    - (a) Stop the development process in IPA by soaking for 20-60 seconds.
    - (b) MIBK dissolves in IPA exothermically. Use pre-mixed stock or mix several hours in advance; development times can be sensitive to developer temperature.
  8. Verify development under a microscope.
  9. Develop the PMGI resist in a solution of CD-26:IPA (1:30) for 45 seconds.
    - (a) Stop the development process in IPA by soaking for 20-60 seconds.
    - (b) The CD-26 concentration and bake-out temperature should be varied in tandem; higher bake-out temperatures require higher CD-26 concentrations. At 265° C, a solution ratio of 3:2 is usually required.
    - (c) The sample can be developed in 10-15 second increments to achieve the desired undercut.
    - (d) A 0.5  $\mu\text{m}$  undercut in the resist should be present depending on the size of the features and the shape of the pattern. Larger features should have larger undercuts.
  10. Verify development under a microscope.

- (a) To ensure complete development, scratch the resist away from the area of interest. The color of the exposed substrate in the scratch and the developed pattern should be the same.
11. Etch the sample in the Intlvac Ion Mill for 30 seconds using the slow etch settings.
- (a) This etch step removes any residual oxide at the contact-dot interface.
12. Deposit the desired film.
- (a) Deposit in an evaporative system (thermal or E-beam) for best results. Sputtering is conformal and may result in poor lift-off.
13. Lift-Off in MICROPOSIT Remover 1165 for 1 hour at 80° C or overnight at room temperature under a fume hood.
- (a) Follow the procedure in Step 11 of the Bilayer Photolithography Recipe in Sec. B.2.
  - (b) PMMA does not dissolve in 1165. A 1:1 mix of NMP and acetone may hasten the development. In this case, do not heat the lift-off bath.

# Appendix C

## Experimental Techniques

The experiments discussed in this thesis require particular care in two areas of experimental technique: low noise measurement (Sec. C.1) and ESD protection (Sec. C.2).

### C.1 Low Noise Considerations

To measure the noise signatures of our samples several steps were taken to remove background noise sources. A short list of the most important settings used in these measurements are provided in Table C.1.

#### C.1.1 Grounding

The most important consideration for a low noise setup is proper grounding of the sample and the experimental equipment. Clean power should be selected from a single outlet where the ground pin of the outlet is known to be clean and not connected to any other equipment (compressors, power supplies, motors, computers, etc.). This ground should be connected to the negative voltage terminal of the sample. All faraday shields discussed below should be grounded to this same ground as well as the chasses of the pre-amplifier and the spectrum analyzer. To avoid ground loops, a single branching point should be selected from which all grounds originate. Since the negative terminals of the pre-amplifier input and output are connected via a  $50\ \Omega$  resistor, the input of the spectrum analyzer should be floated to avoid the introduction of a ground loop.

### C.1.2 Faraday Shielding

All circuits contain loops which are susceptible to fluctuating electromagnetic fields. These loops should be reduced by twisting wire pairs. Where wires cannot be twisted, the experiment should be enclosed with metal shielding. Sheet metal can be used in most cases but it is important to note the skin depth of low-frequency radiation is relatively long ( $\sim 9$  mm for Copper at 60 Hz). The 60 Hz peak in the experiments discussed in this thesis was reduced below the pre-amplifiers background spectra with approximately 5 mm of aluminum shielding.

### C.1.3 Cable Shielding

Cables connected to experimental instruments, especially any connections on the sample side of the pre-amplifier, should be shielded. A two-conductor connection with an additional ground shielding should be used to connect the current supply to the sample (Belden Beldfoil shielded 24 AWG, #9452). This cable shield also provides a ground connection between the faraday shielding of the sample holder and the current supply chassis. Since the SRS 560 pre-amplifier only accepts BNC electrical connections, a single BNC connection was used in this case. The pre-amplifier could be run in A-B mode if additional shielding is needed.

### C.1.4 Magnetic Field Noise

As discussed above, the power supply for any electromagnet should not share the same electrical circuit as the measurement setup to avoid contaminating the ground. The applied magnetic field can introduce noise into the experiment through inductive coupling. Connecting a large capacitor (8200  $\mu\text{F}$ ) in parallel with the magnet reduces several sources of low-frequency noise. Ideally a nonpolar capacitor or two back-to-back polar capacitors should be used. However, for our experiments a single polar capacitor was used without any indication of rupture. For safety, the capacitor was placed in a hollow aluminum tube.

### C.1.5 Spectrum Analyzer Setup

Several settings for the HP 35670A Spectrum analyzer are necessary for proper low-noise measurements. A floating input avoids introducing a ground loop into the measurement circuit. The input should also be AC coupled to eliminate the DC component from the

spectrum and allow smaller input range to be used. A uniform windowing function should be chosen since the signals being measured are not periodic. All other windowing functions will lead to broadening of any residual background noise peaks in the spectra as discussed in the manual of the analyzer. Finally, care should be taken when using the auto-range function on the analyzer. If the analyzer input range is mistakenly set too low, clipping of the spectra will occur and excess noise will appear in the final spectra. However, if the input range is too high the analyzer will not be sensitive to the desired noise signal. When averaging spectra the overload rejection option should be left on to reject those spectra taken at too low of a range and the overload light should be monitored to ensure that the input voltages do not exceed the measurement range setting. Ideally, the auto-range function should be disabled and the analyzer manually set to the correct range, though the auto-range setting was used for some measurements in this thesis.

### C.1.6 Pre-Amplifier Setup

The SRS 560 pre-amplifier was set to a constant gain of 200 for these experiments with a DC coupled input. Higher gain did not improve the signal-to-noise ratio of the measurements as shown in Fig. 2.7. DC coupling allows measurement of the DC sample resistance while also collecting noise spectra. Low-pass filters may improve the signal quality though the roll-off frequencies of these filters should be considered when analyzing the measured PSDs (filters with roll-off frequencies of 100 kHz or higher were used). The pre-amplifier should always be operated under battery power to reduce extraneous 60 Hz noise and never allowed to completely lose its charge. Disconnecting the pre-amplifier from outlet power for 30 minutes prior to making measurements reduces DC drifts in the sample voltage measurements.

<b>Instrument</b>	<b>Parameter</b>	<b>Setting</b>
HP-35670A	Input Coupling	AC
	Window Function	Uniform
SRS-560	Input Coupling	DC
	Gain Mode	Low-noise
	Gain	200
	Power Source	Battery
	Physical separation from other instrumentation	>25 cm
	Input	AC

Table C.1: Instrumentation settings for low noise measurements.

We also note that the pre-amplifier does tend to couple to radiative noise sources from nearby instrumentation even if the chassis is grounded. The best solution to this problem would be to enclose the pre-amplifier in a separate grounded metal box. However, it was generally found that increasing the distance between the pre-amplifier (a distance of  $\sim 25$  cm was used) and other electronics such as the spectrum analyzer was sufficient to reduce these extraneous noise sources.

### C.1.7 Computer and GPIB

The GPIB connections between the measurement instrumentation and the data collection computer provide a  $\sim 2 \Omega$  path to ground which may lead to a contamination of the experiment ground. However, no increase the measured background noise was observed due to the GPIB connection. Even though there is a ground connection, the experimental computer should not share the same electrical circuit as the experimental setup.

### C.1.8 Low-Temperature Setup

The Advanced Research Systems closed-cycle refrigerator used for temperature dependent measurements produces significant amounts of unwanted noise peaks. Proper grounding of the setup did lower some of the background noise. However, a persistent set of noise peaks still appear when a field is applied while the refrigerator is cold. These peaks increase with the square of the magnetic field and appear to originate from a region in the refrigerator near the heating coils (based on investigations with a small permanent magnet). Their magnitude increases as the refrigerator is cooled and remain after the heater is turned on and the sample is warmed up. When the compressor is shut off, they immediately disappear. The origin of this background noise remains unknown though the vibrations of the cryostat likely play a role. These peaks did not significantly impact the experimental results presented here. The RTN spectrum has a broad frequency dependence that is visible on top of these noise peaks. The Lakeshore temperature controller also introduces a radiative noise source. The thermometer nearest the sample produces several harmonics of 60 Hz noise if it is operated in the alternating current (AC) mode. Turning off this function reduces the noise but also reduces the accuracy of the measured temperature. The second thermometer, used in stabilizing the temperature, did not produce any measureable background noise.

## C.2 Electrostatic Protections

In order to safely measure the nanometer scale samples in this work, several considerations were made to protect the samples from electrostatic discharge (ESD).

### C.2.1 Grounding

Connecting the sample to a proper ground is not only valuable for a low-noise measurement setup but also reduces the risk of ESD. Care should be taken to ensure that the sample is always grounded properly to prevent charging.

### C.2.2 Foil Coverings and Experimentalist Wristbands

ESD events associated with interactions between the experimentalist and the measurement equipment were highly correlated with sample breakdown. These arise from static electricity developed while moving around the lab, from plastic lab chair wheels rolling on the lab floor, and other similar sources. They are of largest concern during the dry winter months. It was found that a sample could be connected to the measurement equipment and survive for over 48 hours under full measurement current. However, the simple act of touching the grounded chassis of the spectrum analyzer by the experimentalist was sufficient to destroy the sample under study.

To prevent ESD introduced by the experimentalist several steps should be taken. A grounding wrist bracelet should be worn at all times when working with ESD sensitive samples. Proper bracelets have a high impedance ( $1\text{ M}\Omega$ ) which also protects the experimentalist from high voltages in the measurement equipment. This impedance reduces protection of the sample against electrostatic charges developed when the experimentalist returns to the experimental setup after stepping away (i.e. the bracelet can only bleed static charges from the experimentalist; it cannot prevent a static charge build-up from reaching the sample). Thus, the experimentalist should ground him or herself to a piece of equipment not connected to the measurement setup before touching the wristband. Similarly, to prevent electrostatic build up on any of the experimental surfaces, all insulating surfaces of the work area near the experimental should be covered in aluminum foil and connected to ground.



### C.2.3 Experimental Design and Start-up

Care should be taken in building experimental setups which are used to measure nanoscale samples. In particular, electrical switches which are part of the measurement circuit should be chosen so that no large transient voltages are introduced (i.e. choose make-then-break switches). In addition, all electrical connections between equipment should be completed and all experimental equipment should be turned on before the sample is added to the experimental setup. Large power supplies such as that used for the electromagnet should be electrically isolated from the experimental setup and turned on prior to the sample being introduced. Battery-powered multimeters are safer than their wall-powered counterparts when the sample resistance needs to be measured. A battery powered Fluke 73 III was used for this process with a fixed range larger than  $1\text{ k}\Omega$  (probe current  $<1.5\text{ }\mu\text{A}$ ).

### C.2.4 Wirebonding

The samples studied in this work were connected to the experimental setup via wirebonding using removable DIP chips. In the case of the wirebonder owned by the research groups in the University of Minnesota School of Physics and Astronomy, the stage, the wire, and the bonding tip are well grounded. Any other wirebonder used should be checked for similar grounding considerations. A temporary holder for the sample chip mount was used for wirebonding. Connections on this holder were available to probe the connections to the sample and a switch was installed to allow all of these connections to be grounded during wirebonding.

In the actual process of wiring the sample, wirebonds were made starting on the sample chip mount and only then connected to the sample. After all bonds were completed the continuity of the connections was verified with a Fluke 73 III multimeter. To ensure grounding between the sample leads even when the chip mount was removed from the temporary holder and transferred to the experimental setup, additional wirebonds were added between the terminals on the sample chip mount. Once the transfer was completed, these additional bonds were removed to allow measurements to be made.

### C.2.5 SEM Work

As a final note concerning SEM imaging of the samples, the SEM uses a high voltage source of electrons and the sample substrates are insulating. Thus, any imaging of the

samples necessarily introduces a charge; electrical connections made to the sample after SEM imaging may lead to ESD.

## Appendix D

# Derivation of the FMR Frequency in Square Dots

The ferromagnetic resonance (FMR) frequency discussed in Sec. 4.2.4 provides one estimate of the attempt frequency [58]. We derive the FMR frequency for a square dot using the method outlined in Kittel's *Introduction to Solid State Physics* [82]. For this calculation the magnetization points in the z-direction parallel to one of the dot edges with the y-direction corresponding to the other in-plane easy axis. The x-direction is normal to the plane of the square dot.

The calculation begins by assuming the magnetization precesses about an internal magnetic field  $\mathbf{H}_i$  given by,

$$\mathbf{H}_i = \mathbf{H}_0 - \mathbf{N} \cdot \mathbf{M}. \quad (\text{D.1})$$

where  $\mathbf{N}$  is the demagnetization tensor which characterizes the shape anisotropy of the sample and  $\mathbf{H}_0$  is the external applied field. For this calculation, we approximate the out-of-plane shape anisotropy to be that for an infinite thin film,  $N_x = 4\pi M_s$  and  $N_z = N_y = 0$  in cgs units. The configurational anisotropy is introduced through an effective magnetic field,  $H_{eff}$ , rather than adding it to the demagnetization tensor. Expanding Eq. 3.1 as a series of cosines to first order yields,

$$E(\theta) = -\frac{E_A}{2} \cos 4\theta = -8E_A \cos \theta + \dots, \quad (\text{D.2})$$

which can be rewritten analogously to the Zeeman energy as,

$$E(\theta) = -\frac{8E_A}{M_s V} M_s V \cos \theta + \dots \approx -m H_{eff} \cos \theta. \quad (\text{D.3})$$

From Eq. D.3 we can identify the effective magnetic field produced by the configurational anisotropy minima as  $8E_A/M_s V$ . This effective field points in the plane parallel to the dot edge. Thus the components of the total effective magnetic field felt by the magnetization are:

$$H_x^i = H_x^0 - 4\pi M_x \quad (\text{D.4})$$

$$H_y^i = H_y^0 \quad (\text{D.5})$$

$$H_z^i = H_z^0 + \frac{8E_A}{M_s V} \quad (\text{D.6})$$

The calculation proceeds by determining the steady state precession of the magnetization,  $\mathbf{M}$  following its equation of motion, which is given by,

$$\frac{d\mathbf{M}}{dt} = \gamma(\mathbf{M} \times \mathbf{H}_i). \quad (\text{D.7})$$

where  $\gamma$  is the gyromagnetic ratio (for a bare electron,  $\gamma = 2.8$  MHz/Oe; for Permalloy,  $\gamma \approx 2.94$  MHz/Oe [127]). Since the magnetization precesses about the energy minima in the z-direction with the magnetization aligned in this direction, we may assume to first order  $dM_z/dt = 0$  and  $M_z = M_s$ . The other two components of the Eq. D.7 become, with no external field ( $H_0 = 0$ ),

$$\frac{dM_x}{dt} = \gamma(M_y H_z^i - M_z H_y^i) = \gamma \frac{8E_a}{M_s V} M_y; \quad (\text{D.8})$$

$$\frac{dM_y}{dt} = \gamma(M_z H_x^i - M_x H_z^i) = -\gamma \left( 4\pi M_s + \frac{8E_a}{M_s V} \right) M_x; \quad (\text{D.9})$$

Solutions to these equations that yield a sinusoidal time dependence of the magnetization can be determined following the same procedure in Ref. [82]. The resulting angular precession frequency  $\omega_0$  (i.e. the FMR frequency) is given by,

$$\omega_0^2 = \gamma^2 \frac{8E_a}{M_s V} \left( 4\pi M_s + \frac{8E_a}{M_s V} \right). \quad (\text{D.10})$$

## Appendix E

# Abbreviations and Symbols

Table E.1: List of Abbreviations

<b>Acronym</b>	<b>Definition</b>
AC	Alternating current
AMR	Anisotropic magnetoresistance
CIP	Current-in-the-plane
CPP	Current-perpendicular-to-the-plane
DC	Direct current
EBL	Electron Beam Lithography
ESD	Electrostatic discharge
FMR	Ferromagnetic resonance
GDSII	Graphic Database System II file format
GMR	Giant magnetoresistance
GPIB	General Purpose Interface Bus
HP	Hewlett-Packard
IPA	Isopropanol
LLG	Landau-Lifshitz-Gilbert
MNC	Minnesota Nano Center
$\mu$ GMR	Microwave GMR

continued on next page

Table E.1: continued from previous page

<b>Acronym</b>	<b>Definition</b>
MRE	Magnetorefractive Effect
MTJ	Magnetic tunnel junction
PMGI	Polymethylglutarimide
PMMA	Poly-methyl methacrylate
PSD	Power spectral density
RTN	Random Telegraph Noise
SEM	Scanning Electron Microscopy
STM	Scanning Tunneling Microscopy
SRS	Stanford Research Systems
UV	Ultraviolet

Table E.2: List of Symbols

<b>Symbol</b>	<b>Definition</b>
$a$	Long-axis dimension of rectangular waveguide
$A_{ex}$	Exchange stiffness constant
$c$	Speed of light
$E$	Total magnetic energy
$E_A$	Configurational anisotropy energy
$E_B$	Energy barrier height
$f$	Frequency
$f_0$	Reciprocal of the telegraph state lifetime
$f_A$	Attempt frequency
$H$	Magnetic field
$H_c$	Coercivity
$H_{min}$	Minimum field required for rotational hysteresis
$k_B$	Boltzman Constant

continued on next page

Table E.2: continued from previous page

<b>Symbol</b>	<b>Definition</b>
$m$	Magnetic moment
$M_s$	Saturation magnetization
$N$	Demagnetization tensor
$R$	Resistance
$r$	Reflection coefficient
$R_s$	Sheet resistance
$S_V$	Noise Power
$T$	Temperature
$t$	Transmission coefficient
$V$	Voltage
$\gamma$	Gyromagnetic ratio of the electron
$\epsilon$	Relative dielectric constant
$\theta$	Magnetization direction, defined in Fig.2.1
$\theta_H$	Applied magnetic field direction
$\kappa$	Wavenumber
$\kappa_0$	Wavenumber of an empty waveguide
$\mu$	Relative permeability
$\mu_0$	Permeability of free space
$\rho$	Resistivity
$\sigma$	Conductivity
$\tau$	Torque
$\omega$	Angular frequency
$\omega_0$	Angular precession frequency